Structural and Optical Characterization of Pulsed Laser Deposited MoS_2 and WS_2 Layered Thin Films and Quantum Dots

A Thesis submitted in partial fulfillment of the requirements for the award of the degree of

DOCTOR OF PHILOSOPHY

by

GOBINDA PRADHAN

DEPARTMENT OF PHYSICS
INDIAN INSTITUTE OF TECHNOLOGY GUWAHATI
GUWAHATI-781039, INDIA

January 2020

Structural and Optical Characterization of Pulsed Laser Deposited MoS_2 and WS_2 Layered Thin Films and Quantum Dots

A Thesis submitted in partial fulfillment of the requirements for the award of the degree of

DOCTOR OF PHILOSOPHY

by

GOBINDA PRADHAN

DEPARTMENT OF PHYSICS
INDIAN INSTITUTE OF TECHNOLOGY GUWAHATI
GUWAHATI-781039, INDIA

January 2020

Dedicated to my Family

Gobinda Pradhan
Registration No. 146121006
Department of Physics
Indian Institute of Technology Guwahati
Guwahati-781039, Assam, India

Statement

I hereby declare that the matter embodied in this thesis is the result of investigations carried out by me at the Department of Physics, Indian Institute of Technology Guwahati, Guwahati, India, under the supervision of **Dr. Ashwini Kumar Sharma**. This thesis has not been submitted to any university, institute or elsewhere for the award of any degree, diploma or associate-ship.

Date:10.01.2020 **Gobinda Pradhan**

Dr. Ashwini Kumar Sharma
Associate Professor
Department of Physics
Indian Institute of Technology Guwahati
Guwahati-781039, Assam, India
Tel - 0361 2582724, Fax - 0361 2582749
E-mail: aksharma@iitg.ac.in

Certificate

It is certified that the work contained in the thesis entitled **"Structural and Optical Characterization of Pulsed Laser Deposited MoS_2 and WS_2 Layered Thin Films and Quantum Dots"** by **Mr. Gobinda Pradhan** (Roll no.-146121006), a Ph.D. student of the Department of Physics, Indian Institute of Technology Guwahati is carried out under my supervision and has not been submitted elsewhere for the award of any other degree.

Date: 10.01.2020

(Ashwini Kumar Sharma)

Dr. Ashwini Kumar Sharma
Associate Professor
Department of Physics
Indian Institute of Technology Guwahati
Guwahati-781039, Assam, INDIA

Acknowledgment

First and foremost I would like to express my sincere thanks to my thesis supervisor, Dr. Ashwini Kumar Sharma for his constant guidance and precious advice throughout my research. I really praise him for showing trust in my ability and provide me the freedom to do the research work in my own way. Without his guidance, intuition, patience and hours of discussion, this thesis would not exist. I consider it a great privilege that I had the opportunity to work as a student under his supervision. Apart from professional suggestions, he strengthened my communication skills in various ways.

I am also grateful to my doctoral committee members, Prof. Saurabh Basu, Dr. Subhas Thota, Dr. S Ravi and Dr. S.N. Joshi for their well throughout critique of the progress of my thesis and providing valuable suggestions which steered the thesis in the right direction. My special thanks to Prof. Alika Khare for valuable discussions with her to improve the research work. I owe my thanks to the present and former Head of Department of Physics, IIT Guwahati for providing me the necessary facilities to fulfill my Ph.D. thesis objectives. Thanks to the entire faculty, staff, and students who make this place a great environment to work in.

I am also thankful to central Instrument Facilities, IIT Guwahati for instrumentation facilities. I am grateful to Mr. Ankur Pandey for his kind help in AFM data recording and Mr. Tusharkanta Sahu and Anirban Sikdar for their kind help in HER data recording and Prof. Mohd. Qureshi and Dr. U.N. Maiti for providing the HER experimental facility. I convey my thanks to Dr. Partha P Dey for his assistance in thin-film growth dynamics study and QDs synthesis. I am also indebted to Dr. Rahul Kesarwani for his help in learning the ellipsometric system. It has been a great pleasure to work with my research lab members Dr. Indrajeet, Dr. Partha, Dr. Gyan, Dr. Prahlad, Dr. Rahul, Eshita, Sasmita, Sumit and Nagendra. Thanks to them for assistance in experiments and data analysis. I am deeply indebted to all my friends Gautam, Sasmita, Purusottam, Indu, Nawaz, Shyam, Joy, Srinivas, Jagan, and Ranjan for making me feel like at home during all these years and successful completion of my Ph.D. tenure.

Last but not least, I would like to express my deepest appreciation to my family members for providing me support and encouragement throughout my academic studied.

Abstract

Monolayer to multilayered MoS_2 and WS_2 thin films and quantum dots (QDs) have been synthesized by pulsed laser deposition and pulsed laser ablation in liquid environment. Mono- and a few layered MoS_2 films have been deposited by applying different numbers of laser pulses with similar experiment also performed to synthesize monolayer to multilayered WS_2 thin films by varying the laser fluence and keeping other deposition parameters unchanged. An efficient way to deposit 1T and 2H mixed-phase mono and a few layered MoS_2 thin films in a very short span of time of 20 sec has been achieved by using the pulsed laser deposition technique. The films showed a mixed-phase structure while the 2H to 1T phase ratio which increased from 66 to 84% with an increase in the deposition temperature from 400 to 720 °C. An experimental investigation has been carried out to identify the scaling behavior as well as the growth mechanism of 2D MoS_2 thin films grown by pulsed laser deposition at different deposition time durations, using atomic force microscopy images. The growth of MoS_2 thin films followed intrinsic anomalous scaling behavior. Similar work has been also extended to WS_2 films deposited onto corning glass and SiO_2/Si substrate as well. Spectroscopic ellipsometry has been used extensively to extract the linear optical properties (extinction coefficient, refractive index, excitonic state, bandgap) of the thin films. A significantly large reverse saturation absorption and positive nonlinear refraction response has been observed in all the MoS_2 and WS_2 films deposited at various argon pressure, as measured by the open and closed aperture *Z*-scan experiment under He-Ne laser at 632.8 nm. The anomalously high nonlinear optical response of the film has been attributed to the continuous-wave laser-induced thermal nonlinearity dominance over optical nonlinearity. Optical limiting has been observed in the WS_2 thin films. Along with layered thin films, MoS_2 and WS_2, QDs have been synthesized by multilevel photo-exfoliation of solid MoS_2 and WS_2 targets using pulsed laser ablation in distilled water. As an application, the MoS_2 and WS_2 films of various thicknesses and MoS_2 QDs of various sizes have been used as a catalyst for hydrogen evolution reaction.

Contents

List of Figures

List of Tables

Abbreviations

2D: Two-dimensional

2PA: Two- photon absorption

AFM: Atomic Force Microscopy

BEMA: Bruggeman's Effective Medium Approximation

CA: Closed Aperture

CCD: Charge Coupled Device

CE: Counter electrode

CVD: Chemical Vapor Deposition

CW: Continuous Wave

DRS: Diffuse reflectance spectra

DOS: Density of state

DW: Distilled Water

EDX: Energy Dispersive X-ray

FESEM: Field Emission Scanning Electron Microscope

FETEM: Field Emission Transmission Electron Microscope

GCE: Glassy carbon electrode

HRTEM: High Resolution Transmission Electron Microscope

IFFT: Inverse Fast Fourier Transform

Fig.: Figure

FFT: Fast Fourier Transform

FWHM: Full width at half maximum

He-Ne: Helium-Neon

HER: Hydrogen evolution reaction

HHCF: Height Height Correlation Function

LIP: Laser induces plasma

ND: Neutral density

NLA: Nonlinear absorption coefficient

NLR: Nonlinear refractive index

NPs: Nanoparticles

Nd:YAG: Neodymium-doped Yttrium Aluminium Garnet

NLO: Non Linear Optical

MoS_2: Molybdenum disulfide

OA: Open Aperture

OL: Optical Limiting

PL: Photoluminescence

PLAL: Pulsed Laser Ablation in Liquid

PLD: Pulsed Laser Deposition

PSDF: Power Spectral Density Function

PVD: Physical vapor deposition

QDs: Quantum Dots

RE: Reference electrode

RHE: Reversible hydrogen electrode

RMS: Root Mean square

RMSE: Root Mean Square Error

RSA: Reverse Saturation absorption

SAED: Selected Area Electron Diffraction

SE: Spectroscopic Ellipsometry

SEA: Spectroscopy ellipsometry analyzer

TMDCs: Transition metal dichalcogenides

TRPL: Time-resolved photoluminescence

UV-Vis: Ultra Violet-Visible

WE: Working electrode

w. r. t.: with respect to

WS_2: Tungsten disulfide

XRD: X-Ray Diffraction

Symbols

A	Absorbance	T	Temperature
α	Linear absorption coefficient	f	Focal length
α_{loc}	Local roughness exponent	h	Plank's constant
β'	Nonlinear absorption coefficient	**Hz**	Herz
ρ	FWHM of XRD peak	I_0	Peak intensity at focus
β	Growth exponent	k	Extinction coefficient
c	Speed of light	$Leff$	Effective sample length
D	Crystalline size	**mbar**	Millibar
ε_1	Real part of dielectric function	**min**	Minute
ε_2	Imaginary part of dielectric function	n	Refractive index
λ	Wavelength of light	n_2	Nonlinear refractive index coefficient
ν	Frequency of light	**nm**	Nanometre
ρ	Fresnel reflection coefficient	**ns**	Nanosecond
ϕ	Incident angle of plane polarized light	**Mo**	Molybdenum
Δ	Phase difference between p-and s-polarisation	**S**	Sulfur
°C	Degree Celsius	**W**	Tungsten
cm	centimeter	T_{cl}	Closed aperture transmittance
eV	Electron volt	T_{op}	Open aperture transmittance
E_i	Incident electric field	ω_0	Beam diameter at focus
E_{ip}	Incident electric field for p-polarization	χ^3	Third order nonlinear susceptibility
E_{is}	Incident electric field for s-polarization	z	Sample position
E_g	Optical band gap	z_0	Rayleigh length

Chapter 1

Introduction

The challenging issue with modern electronics is that the Si and other compound semiconductors such as GaAs and GaN-based devices have reached almost their optimized stage, however, the demand is still high for efficient devices concerning device properties like less power consumption, fast operation, smaller size, etc. For further enhancement of the efficiency of electronic devices, some alternative materials need to explore. Two-dimensional (2D) materials can be a solution to eliminate the drawbacks of Si devices. In the year 2004, the synthesis of graphene by Giem et al. was a pioneering work in the field of 2D materials [1]. Graphene is a promising material for the ultrathin electrical conductor, electrodes, flexible display panel, sensor, etc. owing to its unique electrical and mechanical properties [2-4]. It is a zero bandgap material with extremely high carrier mobility of the order of 10^6 cm^2 $v^{-1}s^{-1}$ [5]. However, due to the absence of a natural optical band gap, it has limitations in the application for electronics and optical devices. In addition to graphene, other 2D layered materials like hexagonal boron nitride (h-BN), transition metal dichalcogenides (TMDCs) such as molybdenum disulfide (MoS_2), tungsten disulfide (WS_2), molybdenum diselenide ($MoSe_2$), tungsten diselenide (WSe_2), etc. have drawn significant attention. TMDCs are an emerging class of 2D materials with interesting electronic and optical properties [6-8]. TMDCs with general formula MX_2 (where M-Transition metals (Mo, W) and X- Chalcogen elements (S, Se, Te)), possessing bandgap in the near-infrared to visible regions, have drawn tremendous attention as the potential 2D layered materials which can fulfill the limitations of graphene.

Among all the TMDC materials, MoS_2 has drawn remarkable attention with its excellent semiconductor behavior like tunable band gap of 1.2 (indirect) – 1.9 (direct) eV, high electron mobility, high electronic on-off switching ratio, photo responsibility, etc. which makes it a

futuristic optoelectronic material with its potential applications in spintronics, valleytronics and nanoelectronics devices like Transistor, MOSFET, photovoltaic cell, etc. [9-11]. These properties make it more suitable than graphene for logic device applications. True 2D nature makes MoS_2 outperform Si transistors in terms of nanoscale device limit [12,13]. Recently, various MoS_2-based optoelectronics devices including field effect transistors, integrated circuits and phototransistors, etc. have been reported [14-18]. MoS_2 nanosheets also established their efficacy as catalyst for hydrogen evolution reaction (HER) and as an electrode in super-capacitors [19-21]. Among all the TMDCs, while significant progress has been made on MoS_2, the closely related sulfide WS_2 has started to gain attention recently. WS_2 is emerging as a promising alternative 2D material for new generation electronics devices with its interesting thickness dependent optical band gap from visible (2.1 eV(monolayer)) to infra-red regions (1.3 eV(bulk)), high carrier mobility, high on-off switching ratio as well as chemically stable and mechanically flexible structure [22-27]. Besides the interesting electrical and linear optical behavior, notable optical nonlinearity has been also observed in monolayer to a few-layered MoS_2 and WS_2 films. In the present era, nonlinear optical materials have shown great importance with their excellent modern applications like optical switcher, optical limiter, Q switcher, mode locker, harmonic generator, etc. As a nonlinear optical phenomenon, broadband saturation absorption is experimentally observed in MoS_2 nanosheets and its application as a passive laser mode locker is demonstrated by Zhang et al. [28]. Carlos et.al. reported on the nonlinear optical properties of mono- and few layers of WS_2 [29]. Zin et.al. demonstrated a shift from saturable absorption to reverse saturable absorption in monolayer WS_2 with an increase in laser intensity [30]. Ningning et al. and Zin et al. also reported reverse saturation absorption (RSA) in monolayer WS_2 by two- photon absorption (2PA) using femtosecond laser pulse of wavelength 800 nm (~ 1.55 eV) and 1040 nm (~ 1.19 eV) [30,31]. Along with the 2D layered structure, a lot of work is reported on MoS_2 and WS_2 quantum dots (QDs) synthesis and their excellent use in optoelectronic and

sensing devices [32-35]. In general, for semiconductor QDs the grain size is equal to or less than the exciton Bohr radius of the respective materials. Zero-dimensional QDs of semiconductor materials show additional unique optoelectronics properties compared to their bulk counterpart. By synthesizing QDs of different sizes one can tune the band gap of the QDs which results in photoluminescence (PL) emission at different wavelength. As most of the existing QDs like PbSe, PbS, CdAs, CdSe contain heavy metal which increases the risk of toxic hazards so alternative high efficient nontoxic QDs are in high demand. Hence, MoS_2 and WS_2 QDs which are nontoxic, band gap in the visible region, chemically and thermally stable with a noticeable high efficiency seems to be a good alternative. Recently, MoS_2 and WS_2 nanostructures and QDs have been shown to exhibit immense possibility as hydrogen evolution catalyst [36-40]. An increase in effective surface area and presence of a large number of active sites at the edges of MoS_2 and WS_2 nanostructures increases the HER activity. The high conductivity of metallic 1T phase MoS_2 also makes it an efficient HER catalyst. The catalytic activity of MoS_2 and WS_2 nanostructures can be further increased by modifying their chemical structure, inducing defects and creating strain and doping of external materials.

1.1 Properties of MoS_2 and WS_2

The two TMDC materials, MoS_2 and WS_2, possess similar crystalline and band structures. In a layered MoS_2 film, the intralayer S-Mo-S atoms are covalently bonded while the interlayer MoS_2 films are attached to each other by weak van der Waals force in between interlayer S-S atoms. As shown in fig. 1.1 (a), the S-Mo-S trilayer atomically stacked structure is considered as a single layer MoS_2. In every layered MoS_2 film, the plane Mo and S atoms layers are in hexagonal structure. Generally, MoS_2 has polymorphism structure of two district symmetries called trigonal prismatic 2H (hexagonal crystalline structure) which belongs to the point group of D_{3h} and octahedral 1T phase (tetragonal crystalline structured) with O_h point group. The top view of 2H and 1T phase MoS_2 are shown in fig. 1.1 (b) and (c) and the side

view of 2H and 1T MoS_2 are shown in fig. 1.1(d) and (e). Figure 1.1(f) shows trigonal prismatic symmetry of 2H MoS_2 and fig. 1.1(g) shows the octahedral symmetry of 1T phase MoS_2. 2H-MoS_2 shows semiconducting behavior with a finite band gap between the filled d_{z^2} and empty $d_{x^2-y^2, xy}$ bands while 1T-MoS_2 shows metallic character having Fermi level in the middle of degenerate d_{xy}, d_{yz}, d_{xz} single band [41]. 2H structured MoS_2 is a stable phase and most suitable for all the optoelectronic device applications. On the other hand, 1T phase shows metallic character with a volatile nature and can easily be transformed into 2H phase with high-temperature treatment. Another TMDC, WS_2 also possesses a very similar crystalline structure to MoS_2. The detailed crystalline properties of natural MoS_2 and WS_2 are shown in table 1.1.

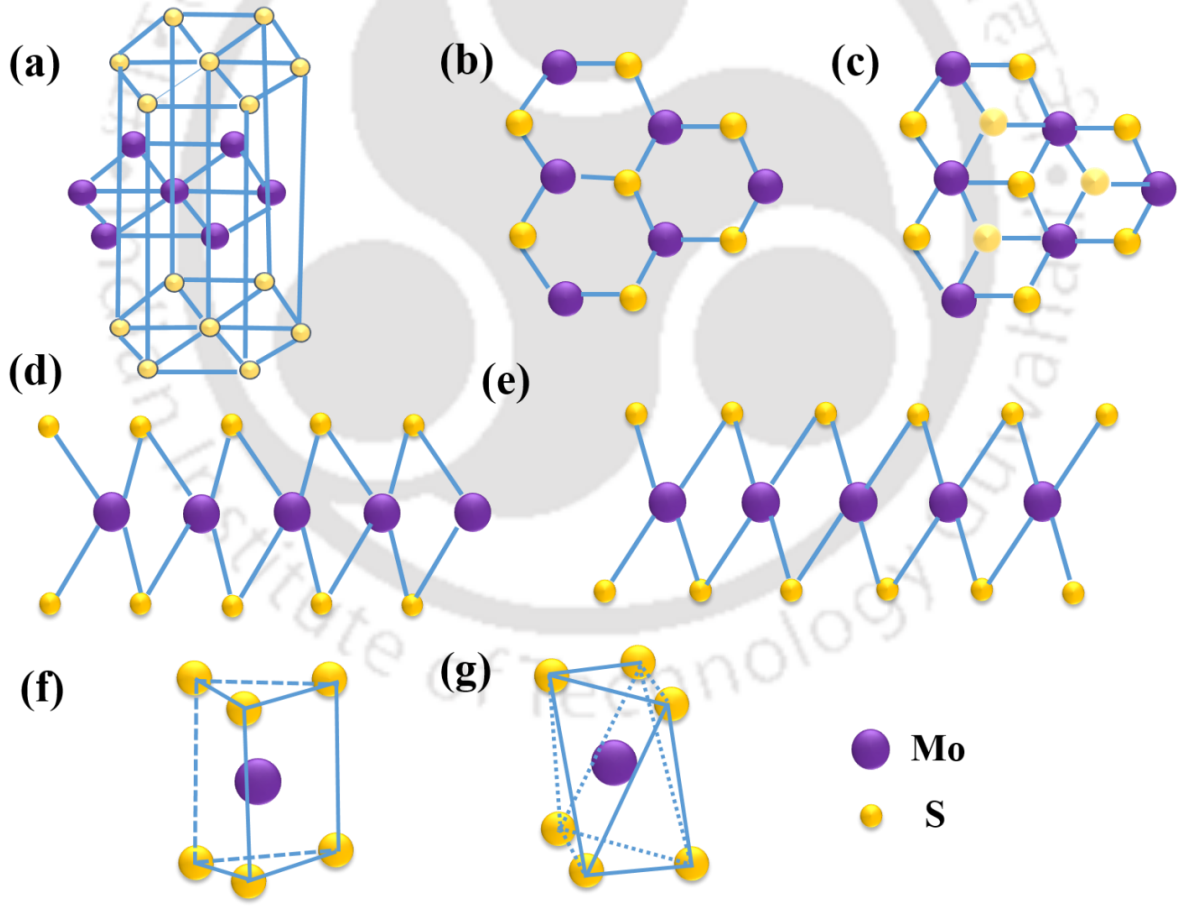

Figure 1.1 (a) Single layered MoS_2 with hexagonal in-plane atomic arrangement of S and Mo atoms. (b) Top view of 2H MoS_2, (c) Top view of 1T MoS_2, (d) Side view of 2H MoS_2 (e) Side view of 1T MoS_2 (f) Trigonal prismatic symmetry of 2H MoS_2 (g) Octahedral symmetry of 1T MoS_2.

Table 1.1 Natural MoS_2 and WS_2 crystalline properties [42,43].

Properties	**MoS_2**	**WS_2**
Crystal structure	Hexagonal	Hexagonal
Unit cell parameters	$a = b = 0.316$ nm, $c = 1.229$ nm, $\alpha = \beta = 90°$, $\gamma = 120°$	$a = b = 0.315$ nm, $c = 1.227$ nm, $\alpha = \beta = 90$, $\gamma = 120°$

The Raman vibrational state is considered as a fundamental property of a material. The Raman vibrational mode is also a useful tool to identify the number of layers of 2D materials like graphene, TMDCs, etc. The Raman vibration modes of 2D materials show a shift in peak positions depending on their layer numbers which are helpful in determining a certain number of layers. The Raman active and IR active lattice vibrational modes of MoS_2 are schematically shown in fig. 1.2. Lattice dynamics of crystalline MoS_2 structure shows four Raman active vibrational mode and two Infrared absorption phonon mode. Four Raman active modes are E_{1g}, $E_{2g}{}^1$, A_{1g}, and $E_{2g}{}^2$ and two infrared active modes are $E_{1u}{}^1$ and $A_{2u}{}^1$ [5,44]. Among the four Raman active mode, A_{1g} is due to the out of plane vibration of S atom while other three modes correspond to the in-plane vibration of S atoms opposite to the Mo atom.

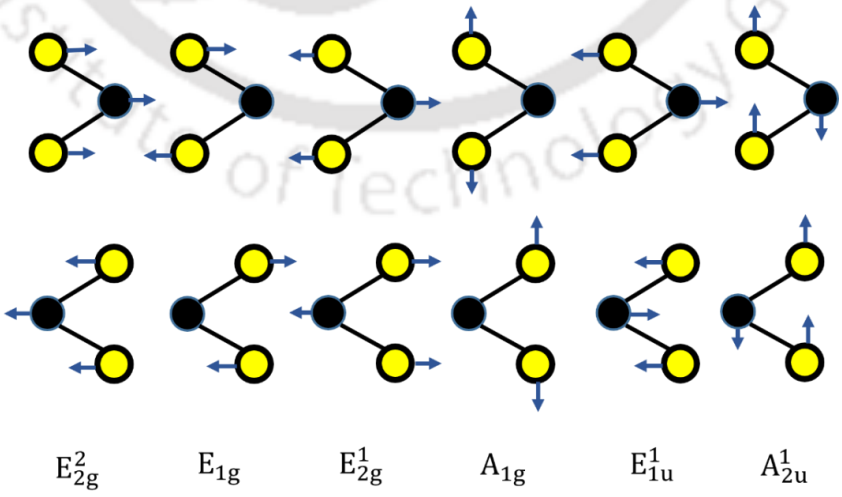

Figure 1.2 Atomic displacement vectors of four first-order Raman active modes $E_{2g}{}^2$, E_{1g}, $E_{2g}{}^1$, and A_{1g} and two IR-active modes $E_{1u}{}^1$ and $A_{2u}{}^1$.

E_{2g}^1 and A_{1g} modes are easily detectable in Raman spectroscopy and their peak position difference is mostly used to determine MoS_2 layer numbers. On the other hand, the other two Raman modes E_{1g} and E_{2g}^2 cannot be easily detected in conventional Raman measurement.

MoS_2 and WS_2 show interesting thickness-dependent bandgap properties. Band structure and band gap energy value of TMDCs 2D layered materials were predicted by First principle calculations using density functional theory [45]. These results were later backed by various tools like UV-vis, PL, and spectroscopic ellipsometer [46,47]. It has been established that bulk MoS_2 is an indirect bandgap semiconductor with bandgap energy of 1.2 eV and the bandgap energy increases with decreasing the thickness due to the quantum confinement effect. Monolayer MoS_2 exhibits a direct bandgap of 1.9 eV [5,45,48]. Like MoS_2, WS_2 also shows thickness dependent optical bandgap from visible (2.1 eV(monolayer)) to infra-red regions (1.3 eV (bulk)) [49,50]. Figure 1.3 shows the band structure of (a) bulk MoS_2, (b) monolayer MoS_2, (c) bulk WS_2 and (d) monolayer WS_2.

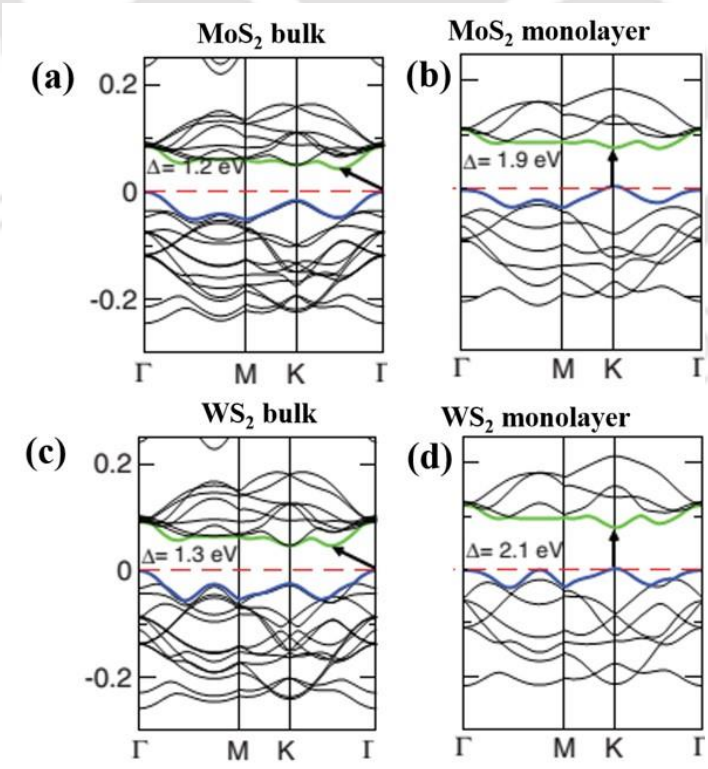

Figure 1.3 Band structure of (a) bulk MoS_2, (b) monolayer MoS_2, (c) bulk WS_2 and (d) monolayer WS_2 [45].

The thickness dependent shift in bandgap from indirect to direct bandgap and their affect in optical behavior can easily be observed in PL and UV-Vis spectroscopic measurements. Monolayer MoS_2 and WS_2 show intense PL peak between 600-700 nm as compared to their bulk counterpart [10,46,47]. In UV-Vis spectrum, two distinguishable excitonic transition peaks A and B can be observed in monolayer MoS_2 and WS_2 thin film [51-53].

The optical properties of 2D materials can be accurately measured using spectroscopic ellipsometry (SE) technique. SE measurement is a nondestructive and noncontact technique to extract the optical properties (extinction coefficient, refractive index, bandgap) of thin films by modeling the change in polarization state of the reflected light from the sample surface. Using the SE fitting thin film thickness and root means square (RMS) roughness can also be derived with high accuracy. This technique can be applied to a few nm ultrathin film where Swanepoel envelope approximation cannot be applied due to the lack of interference pattern in the UV-Vis transmission spectra of the ultrathin films. This technique is also very much useful for thin films grown on non-transparent substrate i.e. Si, where UV-Vis transmission spectra cannot be recorded. In recent years SE has been used extensively to investigate the optical response of a few nm thick 2D materials i.e. graphene, MoS_2, WS_2, $MoSe_2$, etc. [54-56].

Along with linear optical properties, TMDC 2D materials also show interesting nonlinear optical behavior. For nonlinear optical measurement, Z-scan is a useful technique to rapidly measure the nonlinear refraction (NLR) and nonlinear absorption (NLA) of a nonlinear solid, liquid or gaseous medium. In the year 1989, Sheik Bahae et al. proposed the single beam NLO measurement technique which is based on the principle of spatial beam distortion [57]. The name Z-scan originated from the fact that during the measurement in this technique, sample is translated along the propagation direction of a focused laser beam, which is conventionally considered as Z-axis. As the sample is translated along the focused laser beam it experiences different laser intensity at different Z positions. In this way, this technique takes into account

the transformation of phase distortion and amplitude distortion during beam propagation. As merit, this technique allows measuring the magnitude and sign of the NLO parameters i.e. nonlinear refractive index ($n_{2)}$ and third-order susceptibility (χ^3) as well as the real and imaginary part of χ^3. On the other hand, as a demerit, the origin of nonlinearity in a sample due to different mechanisms cannot be differentiated in this technique. Till now this technique has been applied successfully in a variety of materials to analyze their NLO properties [58,59]. There are multiple reports on the NLO characterization of 2D materials using Z-scan technique [28,60,61].

1.2 MoS_2 and WS_2 nanostructures

Monolayer to multilayered MoS_2 and WS_2 thin films are potential materials for nanoelectronic and optoelectronic devices [62-64]. Possessing a large scale of applications, the controlled synthesis of layered MoS_2 films has great importance. The 2D layered MoS_2 films have been synthesized by similar techniques used for graphene. A few layers even monolayer TMDCs have been synthesized through the 'Scotch tape method'. Among different approaches, mechanical exfoliation from a geological bulk sample is a promising way to obtain good structural layered MoS_2 film [44]. Large area MoS_2 films grown via chemical vapor deposition (CVD) technique has been reported [65-67]. Along with 2D materials layered structures, like nanosheets, heterostructures and hybrid structures, QDs have also shown advantages in catalytic and sensing applications [68-72]. The heterostructure of semiconductor materials play a crucial role in high-speed electronic devices. Beyond conventional semiconductors, 2D material heterostructures like MoS_2/WS_2, MoS_2/Graphene, and WSe_2/MoS_2, etc. have emerged as high electronic performance devices. Many physical properties like interlayer coupling, electronic nature, interlayer hot exciton formation, etc. have been explored on similar structures. Rui et al. showed excellent photo rectification and rapid photoresponse behavior of vertically stacked WSe_2/MoS_2 heterostructures [73]. Kun et al. demonstrated an intrinsic p-n diode phenomenon in a MoS_2 (monolayer)/ WS_2 (multilayer) heterostructure [74].

Along with the 2D layered structure, MoS_2 and WS_2 QDs have drawn tremendous attention with their useful optical direct band gap properties. Recently, a lot of efforts have been made in the synthesis of MoS_2 and WS_2 QDs by various processes like multi exfoliation based on lithium intercalation, hydrothermal route, wet-grinding assisted co-solvent sonication, probe assistant ultra-sonication, solvent assisted sono-chemical exfoliation process, etc. [32,33,75,76]. Very recently, Bo et al. [77] have reported monolayer MoS_2 QDs synthesis by femtosecond laser ablation of a solid MoS_2 target in water while Tugba et al. [78] reported on the preparation of 2D/3D MoS_2 nanosheets of various sizes by nanosecond laser ablation of MoS_2 powder in methanol.

1.3 MoS_2 and WS_2 thin film synthesis approaches

In the year 2004, Novoselov et al. succeeded in extraction of single layer graphite or graphene by mechanical exfoliation (using scotch tape) technique [79]. Soon after that, single to multilayered thick other 2D materials like MoS_2, WS_2, BN, etc. were fabricated by using the same technique [44,62]. In this process, nano to micro size MoS_2 flakes are peeled off from bulk MoS_2 and transferred to another substrate. This process offers high quality flakes which are most suitable for device performances. However, the drawback of the process is that there is no control over the flake size and thickness. Another class of exfoliation called chemical exfoliation is also used to separate MoS_2 layers from the bulk MoS_2 crystal. In chemical exfoliation two basic approaches are used, ion intercalation and solvent-based exfoliation [80,81]. In the ion intercalation method generally, lithium ions are inserted in between the MoS_2 layers and then water is introduced to the system to allow the interaction of lithium ion and water to form hydrogen gas in between the MoS_2 layers. The released hydrogen gas forces the MoS_2 crystal apart into layered structure. A longer duration of reaction (3-4 days) and a little control over the extent of intercalation is a major drawback of the experiment. On the other hand, the solvent-based exfoliation is a relatively new technique which was proposed by Coleman et al.

in 2011 [82]. In this technique, bulk MoS_2 crystal is introduced into organic solvents like isopropyl alcohol (IPA) and N-methylpyrrolidone (NMP) and after reaction the bulk crystal gets fragmented into layer by layer structure.

Among other techniques, 'hydrothermal process' is a solution based process to produce MoS_2 nanostructures. In this process, typically, a molybdate compound is allowed to react with sulfide or pure sulfur in a stainless steel autoclave in a controlled high temperature and high pressure environment for several hours [83-85]. The resultant product can either be powder or thin film or in the form of various nano shapes, depending on the preparation conditions. The *as*-synthesized MoS_2 shows different qualities of crystallinity. Very often, the resultant product passes through high-temperature treatment to further improve its crystalline structure.

In a controlled way, for the first time in 2009, large scale homogeneous graphene was synthesized onto copper substrate using chemical vapor deposition (CVD) technique [86]. CVD is used extensively to realize highly crystalline monolayer to multilayered thin films of 2D materials like MoS_2, WS_2, $MoSe_2$, BN, etc. [87-89]. In CVD technique, MoS_2 or WS_2 films are mainly deposited onto solid substrate via (i) vaporization of transition metal and chalcogen precursors (for WS_2 film, $WOCl_4$ and $HS(CH_2)_2SH$ are used as precursors), (ii) direct sulfurization of pre-deposited transition metal (Mo, W) or (iii) conversion of transition metal oxide (MoO_3, WO_3) into MoS_2 or WS_2 by sulfurization. As prepared films show superior optical properties and are very useful for optoelectronic devices. Despite promising results, control over film thickness and film uniformity still remain a problem in CVD technique.

Along with the processes like CVD, hydrothermal and sulfurization processes as well as chemical and mechanical exfoliation, pulsed laser deposition (PLD) technique has also shown its potential to synthesize mono-to-multilayered MoS_2 and WS_2 thin films [27,90,91]. PLD can be a great alternative process to synthesize layered TMDCs structures, although there are only a

few reports till date. Siegel et.al, have successfully deposited layered MoS_2 film on crystalline *c*-sapphire substrate using PLD [92]. Loh et al. have studied the growth mechanism of pulsed laser fabricated layered MoS_2 films on various metal substrates like Cu, Ni, Al and Ag [93]. Useful device applications of PLD MoS_2 film are reported by Late et al. and Serrao et al. [94,95]. In the last few years, WS_2 films of thicknesses monolayer to multilayer to a bulk-like structure have been deposited via PLD and their usefulness as photodetector, HER catalyst has been demonstrated in the literature [96-100].

1.4 PLD as a versatile thin film deposition technique

This technique was first used by Smith and Turner in 1965 to deposit semiconductors and dielectric materials and later it started to gain popularity after the synthesis of high T_c superconductors using PLD by Dijkkamp et al. in 1987 [101,102]. Today, PLD is an established versatile physical vapor deposition technique for growing various kinds of complex oxides, sulfides, carbides, nitrides, pure metallic thin films, and polymers, etc. [103-107]. In this technique, a focused pulsed laser beam is used to ablate a target material and a plasma plume is formed by the ejected material. The constituents of the plasma are deposited as a thin film onto a substrate placed in front of the target a few centimeters apart. By optimizing the parameters like gas pressure, type of ambient gas, substrate temperature, target-to-substrate distance, laser wavelength and fluence one can control the chemical composition, surface morphology, and crystallinity of the deposited films [108-111]. PLD also offers a uniform well-adhered film through the impingent of highly energetic (0.1- 10 eV) ions and ionic radicals of the target material onto the substrate. PLD has some potential advantages likes stoichiometric transfer between target and deposited film, high deposition rate, greater control over growth, epitaxy growth at low temperature, etc. compared to the other deposition techniques. As a drawback, PLD also suffers from a few limitations like uneven deposition, smaller deposition area, requirement of

many parameters to optimize the deposition, etc. In PLD technique one can easily control the film thickness using different numbers of laser pulses.

1.5 Motivation and objective

Being a futuristic material, lots of efforts are underway to synthesize 2D layered MoS_2 and WS_2 films by various techniques. Different approaches like mechanical exfoliation, CVD, hydrothermal techniques, etc. have been used to synthesize layered MoS_2 films [65,67]. The control over film thickness in a systematic way still remains a problem. Hence, PLD can be a great alternative technique to synthesize layered TMDCs structure, although there are only a few reports till date [92]. Usually, single phase 2H MoS_2 layered film can be synthesized by various processes like hydrothermal, sulfurization, chemical vapor deposition as well as chemical and mechanical exfoliation. Unlike 2H MoS_2 it's a great challenge to prepare single-phase 1T MoS_2. However, there have been efforts to prepare 1T-MoS_2 by lithium intercalation of 2H-MoS_2 and other complicated chemical reaction methods which are tedious and time-consuming processes [112,113]. All these methods result in a 50-80% 2H-1T mixed phased MoS_2. An efficient synthesis process for large-scale 1T MoS_2 production is still scarce. However, the growth of 1T phase MoS_2 grown via PLD is rarely reported. Similarly, to synthesize MoS_2 QDs, instead of various tedious and time-consuming processes (lithium intercalation, hydrothermal route, wet-grinding assisted co-solvent sonication, probe assistant ultra-sonication, etc.) pulsed laser ablation in liquid (PLAL) could be an efficient and easy way to synthesize MoS_2 QDs. In PLAL technique the ablation parameters like laser fluence, laser wavelength, ablation time, liquid medium, etc. can play a significant role in regulating the shape and size of synthesized QDs. Hence a systematic study is required to understand the effect of the parameters on the shape and size and concentration of the generated MoS_2 and WS_2 QDs. Along with the excellent electrical and linear optical behavior, reports are also available on the optical nonlinear behavior of monolayer to a few-layered MoS_2 and WS_2 thin

films and nanosheets [28]. To the best of our knowledge, there is hardly any systematic study on NLO properties of pulsed laser deposited MoS_2 or WS_2 multilayered films. Surface morphology of thin films can control many of the physical and chemical properties (such as optical, catalytic, mechanical, electronic, etc.) which can strongly affect the device performance of the respective films. As our focus is on linear and nonlinear optical behavior of 2D thin film materials, therefore, understanding the growth dynamics of the deposited thin films is very important. The growth dynamics of thin films expressed by scaling theory is a useful tool to quantify the statistical properties of the surface morphology of thin films and to formulate theoretical models of growth modes for different inorganic materials such as metals, semiconductors, perovskite material, etc. The growth mechanism of 2D van der Waals materials remains poorly investigated till date. The growth dynamics of 2D materials using scaling functions under PLD has never been reported which motivated us to undertake similar work on MoS_2 and WS_2 thin films.

1.6 Thesis Organization

In the present thesis, growth of monolayer to multilayer MoS_2 film is studied on various substrate like SiO_2/Si, Corning glass, Si by varying the deposition time in PLD. 2H-1T mixed-phase mono and few-layered MoS_2 films have been obtained by PLD in a very short time span of only 20 sec at various deposition temperatures. The tunability of the ratio of the two phases with deposition temperature as well as deposition time has been investigated extensively. The kinetic roughening of MoS_2 thin films grown by the PLD technique has been studied based on generic scaling *ansatz*, using surface morphology information from atomic force microscope (AFM) images of the films. We have reported on the effect of deposition parameters on linear and nonlinear optical properties of a few layered MoS_2 and WS_2 films. MoS_2 and WS_2 QDs of various sizes have been synthesized by tuning the nanosecond pulsed laser fluence and ablation

time. Further, the MoS_2 and WS_2 thin films and QDs have been shown as efficient catalyst for hydrogen evolution reaction (HER).

The overall thesis work is structured into various chapters as follows:

Chapter 1: Introduction contains literature survey on 2D materials and their properties along with motivation and objective of the present work.

Chapter 2: Experimental details describes the details of the experimental setup of PLD, PLAL, *Z*-scan and HER. The characterization techniques used for the analysis of structural and optical properties of thin films and QDs are also discussed.

Chapter 3: MoS_2 and WS_2 monolayer to multilayered thin film synthesis by pulsed laser deposition describes the monolayer-to-multilayered MoS_2 and WS_2 thin film deposition via PLD by varying deposition time and laser energy. A study on crystalline 1T/2H mixed phase MoS_2 thin film formation and their phase ratio modulation with the deposition conditions like substrate temperature, deposition time, etc. is also discussed in detail.

Chapter 4: Surface evolution of a few-layered to bulk-like MoS_2 and WS_2 thin films during growth under pulsed laser deposition discusses the evolution of surface morphology of MoS_2 and WS_2 films from layered-structure to bulk-like structure. The growth exponents are correlated with the optical parameters of the respective films.

Chapter 5: Nonlinear optical characterizations of MoS_2 and WS_2 thin film presents a detailed study on the *Z*-scan measurements to estimate the nonlinear optical parameters like nonlinear absorption coefficient, nonlinear refractive index, and third-order nonlinear optical susceptibility of the deposited thin films. Optical limiting property of the films is also reported.

Chapter 6: MoS_2 and WS_2 quantum dots synthesis by pulsed laser ablation in liquid presents the realization of MoS_2 and WS_2 QDs using a chemical-free simple physical process. The role of laser ablation parameters in the synthesis of QDs is also discussed in detail.

Chapter 7: MoS_2 and WS_2 thin films and quantum dots as a catalyst for hydrogen evolution reaction presents the application of the MoS_2 and WS_2 thin films and respective QDs as an efficient catalyst for hydrogen generation.

Chapter 8: Conclusions highlights the important results and potential future scope of the present work.

भारतीय प्रौद्योगिकी संस्थान गुवाहाटी
Indian Institute of Technology Guwahati

Chapter 2

Experimental details

2.1 Introduction

The present work is focused on layered MoS_2 and WS_2 thin films and QDs synthesis and characterization of the respective nanostructures. Since PLD technique is known for high deposition rate and fine control over film thickness, it can be a potential technique to synthesis layered 2D material thin films. On the other hand PLAL is chemical-free, simple physical technique to synthesize nanoparticles. It can also be very effective technique to fabricate MoS_2 and WS_2 QDs. In the present thesis, PLD technique is applied to fabricate monolayer to multilayer to bulk like MoS_2 and WS_2 thin films onto various substrates and the properties of the film are modified by controlling various deposition parameters like deposition time, laser fluence, deposition temperature, gas pressure, etc. Besides thin films, MoS_2 and WS_2 QDs are also synthesized using PLAL technique. The structural properties of the thin films and QDs are characterized by Raman spectrometer, X-ray diffraction (XRD), field emission transmission electron microscope (FETEM) and the surface morphology are studied by field emission scanning electron microscope (FESEM), AFM and linear optical behavior are analyzed by UV_VIS_NIR spectrometer, fluorescence spectrometer, and spectroscopic ellipsometer. Nonlinear optical characterization of MoS_2 and WS_2 films is performed with an in house assembled Z-scan setup.

In this chapter, the experimental setup of PLD, PLAL, Z-scan and HER experiments are discussed. All the characterization tools used for analyzing thin films and QDs structure, crystallinity, and optical properties are also discussed.

2.2 Preparation of MoS_2 and WS_2 pellets as PLD target

For depositing MoS_2 and WS_2 thin films, sintered MoS_2 (and WS_2) pellets were prepared from highly pure MoS_2 (and WS_2) powder (bought from Alfa-Aesear). The powder was pressed to a pellet of diameter 13 mm and thickness 3 mm using a hydraulic system by applying a pressure of 75 kg/cm^2. Further, the pellets were sintered at 800 ℃ for 8 hours in the argon atmosphere to yield hard pellets without any impurities or oxidation. The sintered pellets were used as the target in PLD system. Figure 2.1 shows the images of the *as*-prepared MoS_2 and WS_2 pellets.

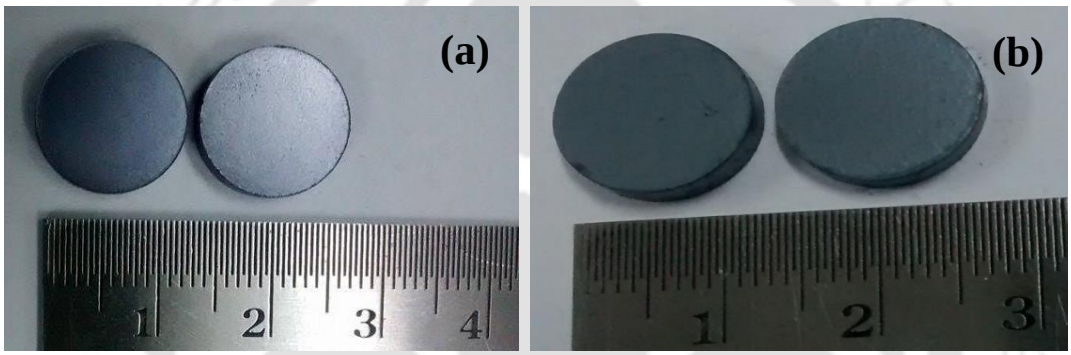

Figure 2.1 Images of (a) MoS_2 and (b) WS_2 pellets.

2.3 Substrates

MoS_2 and WS_2 thin films were deposited onto SiO_2/Si, Si, corning glass and FTO substrates. Prior to deposition substrates were dipped into acetone and sonicated for 45 min. After removing from acetone solutions, the substrates were cleaned and dried with the flow of pure nitrogen gas (99.99% purity) and then placed onto the substrate holder inside the deposition chamber.

2.4 PLD setup

PLD is established as a versatile physical vapor deposition technique (PVD). Finely controlled thin films are deposited by PLD by following three processes: (a) laser matter

interaction causing ablation of solid target and generation of laser induces plasma (LIP), (b) expansion and cooling of LIP and interaction with the chamber atmosphere and (c) deposition as a thin film onto the substrate placed a few centimeters away from the target. The PLD setup used in the present work to synthesize MoS_2 and WS_2 thin layered films is shown schematically in fig 2.2. Figure 2.3 shows the photograph of the PLD system used for the experiment. It consists of an ultra-high vacuum compatible 12" diameter stainless steel chamber with multiple ports for the attachment of evacuation unit, target and substrate holder and pressure gauge units.

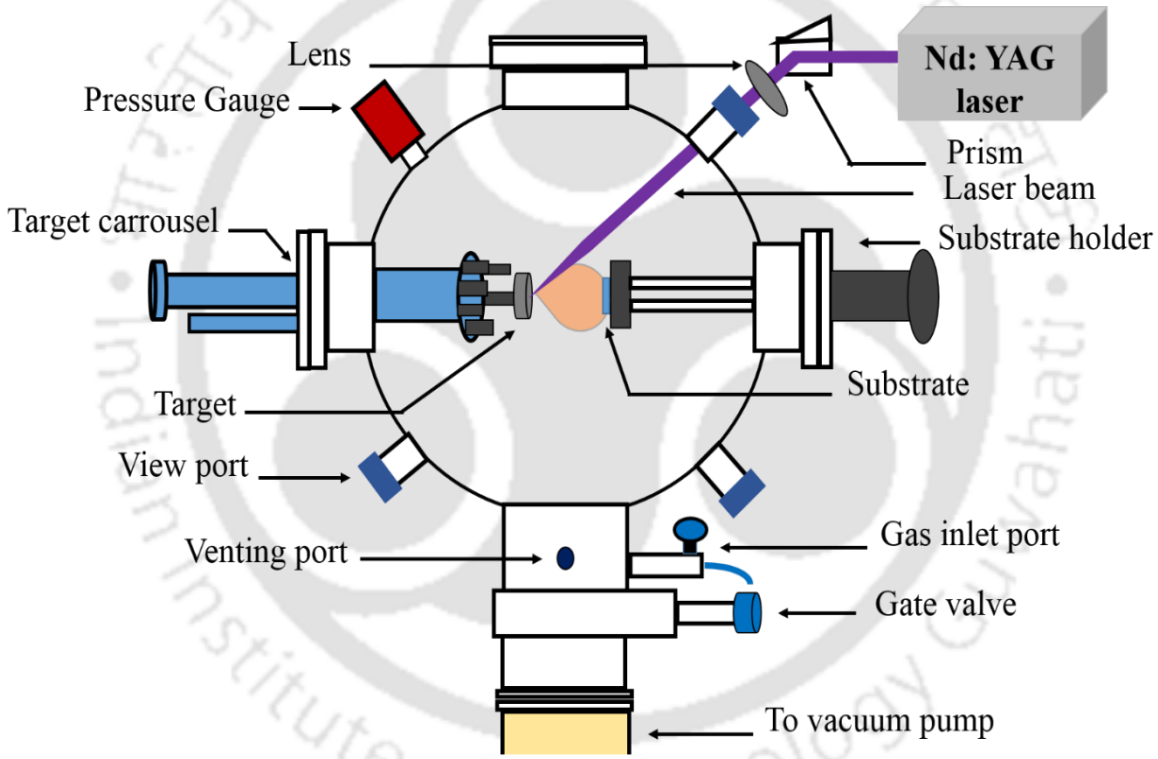

Figure 2.2 Schematic diagram of PLD setup.

Along with all the attached units, there are some extra ports which are used for the laser beam and observation and monitoring purposes. Motorized target carrousel was fixed with the chamber in horizontal plane through one of the 150 CF ports. The target carrousel can hold six targets at a time. Substrate holder was attached to the chamber on the opposite side to the target

holder. Multiple substrates can be placed onto the substrate holder-cum-substrate heater with a maximum achievable temperature of 800°C in a programmable way. The substrate holder unit is assembled within the chamber with a 150CF port parallel to the target carrousel unit. During deposition target-to-substrate distance was fixed at 5 cm. High level vacuum was achieved inside the chamber with the help of turbo pump (*Pfeiffer, Hi pace 300 C*) backed by rotary pump (*Pfeiffer, DUO 10 MC*). The vacuum level of the chamber was measured by various gauges.

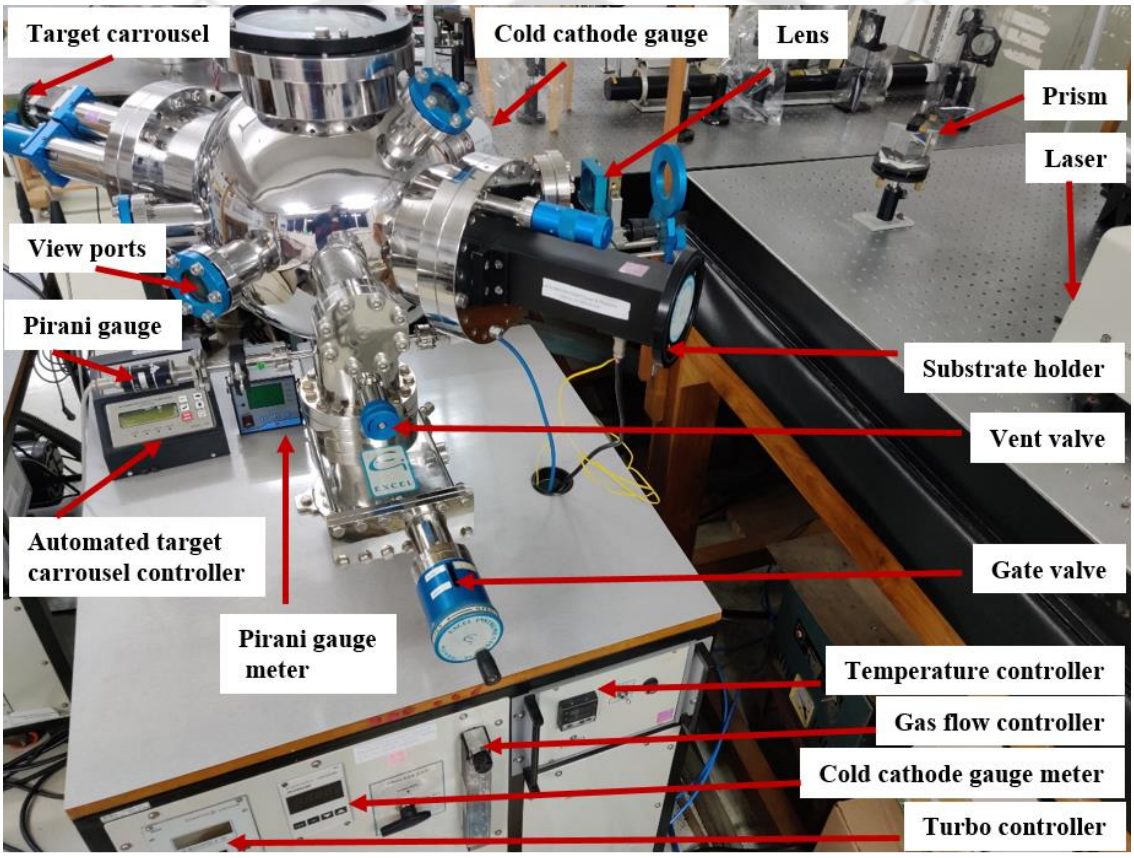

2.3 Photograph of PLD setup.

Cold cathode gauge (*Pfeiffer, IKR 251*) was used for ultra-low pressure (10^{-2} – 10^{-7} mbar) measurement and Pirani gauge was used to measure high pressure (10^{3} – 10^{-3} mbar). Along with all these components, another most significant component is high power pulsed

laser source (third harmonic Q switched Nd:YAG laser). The laser system was placed externally near the chamber and using several optical components the laser beam was allowed to enter through one of the ports of the chamber. The pulsed laser beam was used for ablating the solid target. During laser ablation, plasma plume was formed by the ejected material. The plasma plume moves in the forward direction from the target surface interacting with the surrounding atmosphere. The plasma plume contains the ablated material that is deposited as a thin film onto the substrate placed in front of the target. In PLD, by optimizing various parameters like gas pressure, type of ambient gas, substrate temperature, target-to-substrate distance, laser wavelength and fluence one can control the chemical composition, surface morphology, and crystallinity of the deposited films [108-111].

Monolayer to multilayer MoS_2 films were deposited onto SiO_2/Si substrate heated to 600 ℃ under vacuum ($\sim 5 \times 10^{-6}$ mbar). The films were deposited for the time duration of 14, 24, 30 sec and 6 minutes. A similar experiment was also performed to synthesize monolayer to multilayered WS_2 thin films where the laser energy was varied from 20 to 30 mJ and other deposition parameters were kept constant. To monitor the 1T/2H phase ratio, films were deposited at the substrate temperatures of room temperature (RT ~25 ℃), 300, 400, 500, 600 and 720 ℃ with 200 number of laser pulses while all others parameters were kept constant. To study the growth dynamics of 2D materials, the films were deposited on Corning glass and SiO_2/Si substrates for various deposition times of 20 sec, 1, 2, 5, 10, 15 and 20 min duration. Multilayered MoS_2 and WS_2 thin films were also deposited under Ar gas atmosphere at a pressure of 10^{-1}, 10^{-2}, and 10^{-5} mbar, respectively.

2.5 PLAL experimental setup

PLAL is a versatile technique to synthesize nanoparticles of various shapes and sizes from a bulk sample. Most importantly, the experiment is free of using any kind of chemical

reagent and mostly performed at room temperature. PLAL method is mostly used to synthesize pure and stable novel metal (like Au, Ag and Cu, etc.) nanoparticles. Various semiconductor QDs (like Si, Ge, CdTe, ZnS, etc.) have been successfully synthesized following this technique. The technique shows a great possibility as an efficient, single step, simple physical process to synthesize MoS_2 QDs. In PLAL technique the ablation parameters like laser fluence, laser wavelength, ablation time, liquid medium, etc. can play a significant role in regulating the shape and size of synthesized QDs. Hence, in the present work, a systematic study on the effect of the parameters on the shape and size, concentration of the generated MoS_2 and WS_2 QDs is reported.

The schematic of the experimental setup for laser ablated MoS_2 QDs from a solid bulk-MoS_2 target is shown in Fig. 2.4. A photograph of the experimental setup of during an experiment is shown in fig. 2.5. MoS_2 pellet of diameter 13 mm and thickness 3 mm was used as the target for laser ablation. The pellet was stick at the bottom of a beaker filled with 8 ml of distilled water (DW). Nanosecond laser beam from the 2nd harmonic (wavelength 532 nm) of a Q-switched Nd: YAG laser with a pulse duration of 8 ns and a repetition rate of 10 Hz was used for ablating the target. The laser beam was focused on the MoS_2 target by using several optical components like optical mirror and then finally focused using a 25 cm focal length lens onto the target immersed in DW. During laser ablation, the open surface of the beaker was covered with a transparent glass plate to protect the lens from water splashing. To ensure the availability of fresh area of ablation with each laser shot, the liquid cell was placed onto a motorized translational stage which was continuously translated during the experiment. The colloidal solution was also manually stirred in between the ablation process to facilitate proper distribution of the NPs formed and to enable the laser beam to reach the target easily without getting obstructed by the suspended MoS_2 nanoflakes, nanoparticles and QDs in order to ensure uniform ablation throughout the ablation time.

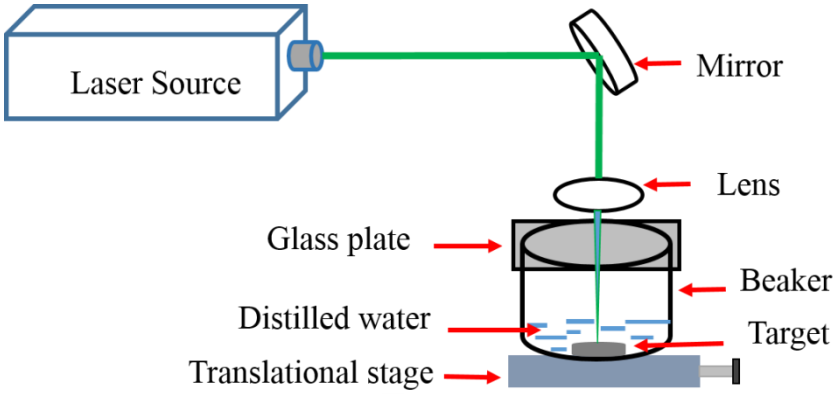

Figure 2.4 Schematic diagram of PLAL setup.

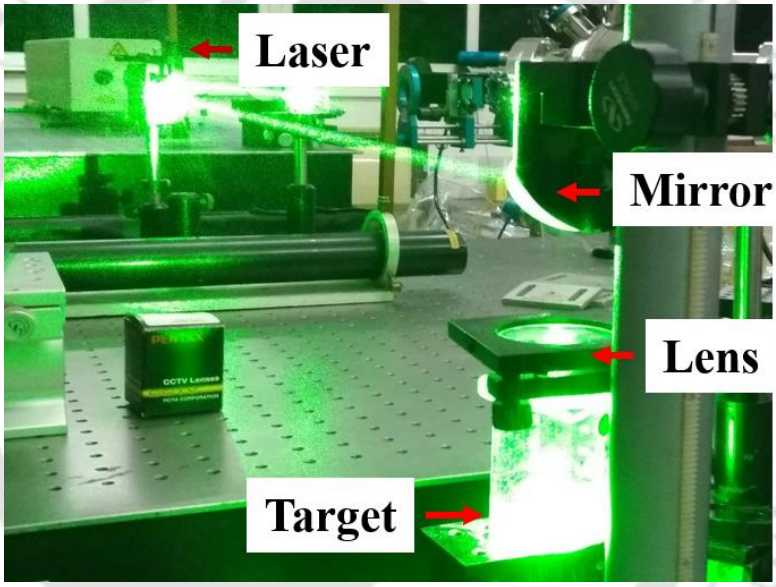

Figure 2.5 Photograph of PLAL setup.

After laser ablation, the samples were further sonicated and centrifuged to obtain the QDs solution. The three-step processes, *as* presented schematically in Fig. 2.6, were followed to extract MoS_2 QDs from a bulk solid MoS_2 target. At first, during laser ablation, multilevel photo-exfoliation i.e. detachment of the multilayer MoS_2 QDs, nano-sheets from bulk MoS_2 target occurred. In the second step, the solution was ultrasonicated for 2 hours to reduce the particle size. Finally, the solution was centrifuged at 12000 rpm for 10 min. After centrifugation, supernatant solution was collected which mainly contained MoS_2 QDs.

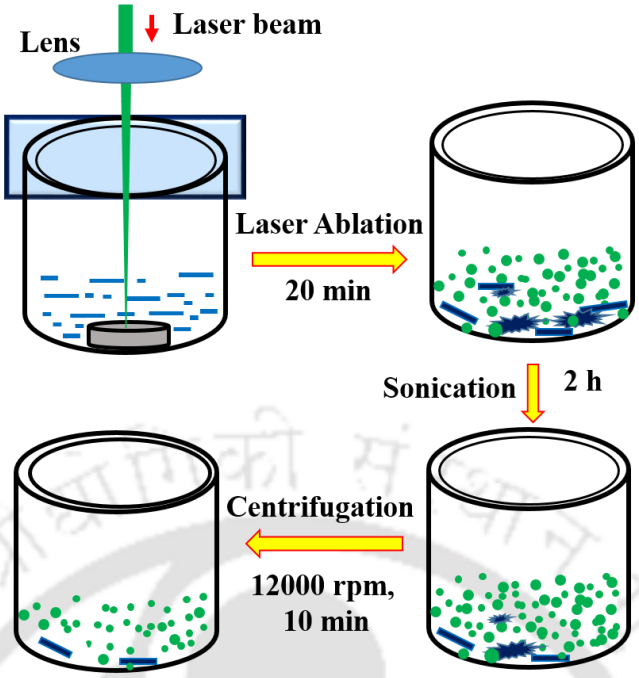

Figure 2.6 Schematic representation of MoS_2 QDs synthesis by nanosecond pulsed laser ablation of solid MoS_2 target submerge in distilled water.

Figure 2.7(a) shows the post-ablation solution of ablation times of 5, 10 and 20 min, respectively for a fixed laser energy of 40 mJ. The laser ablation produced blackish colloidal solution which mainly consisted of MoS_2 nano-sheets, nano-particles and QDs. The concentration of the solution is higher at higher ablation time. Figure 2.7(b) shows the post-centrifuged supernatant solution at ablation times of 5, 10 and 20 min, respectively where the solutions turned from blackish to pale yellowish or almost transparent.

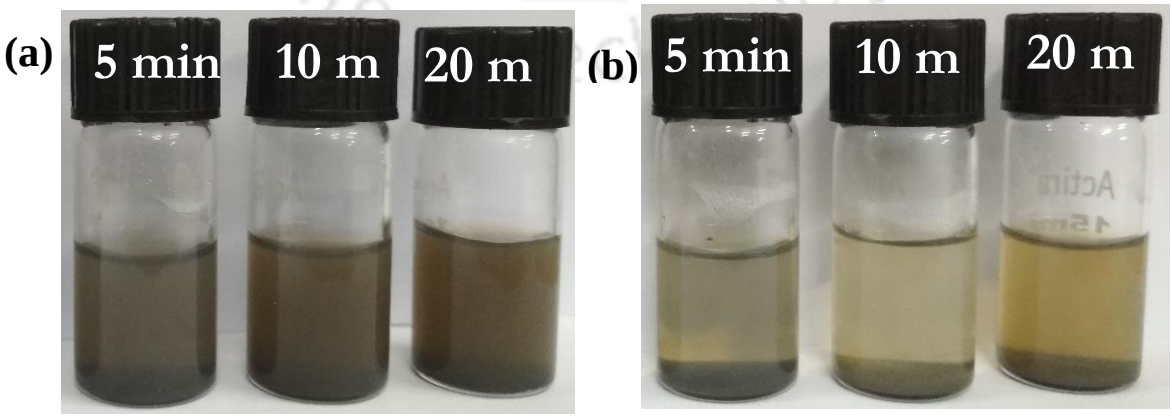

Figure 2.7 Photograph of (a) post-ablated solution at ablation times of 5, 10 and 20 min and (b) post-centrifuged supernatant solution at ablation time of 5, 10 and 20 min, respectively.

In the present work, MoS_2 and WS_2 QDs were synthesized by the PLAL technique with a nanosecond pulsed laser at various laser fluence and ablation time. The effect of laser fluence and ablation time on QDs size and their structures were investigated systematically. The shape and sizes of the QDs were characterized by FETEM and AFM images. All the samples were subjected to Raman spectra and XRD pattern analysis to identify the crystalline properties. Further, the optical properties were investigated by recording the Photoluminescence and UV-Vis spectra, time-resolved photoluminescence (TRPL) of the respective QDs.

2.6 Z-scan setup

The concept of single beam Z scan technique to measure the optical nonlinearity of various materials was first demonstrated by Bahae et al. in 1989 [57]. The basic working principle of the technique is based on the nonlinear optical loss and phase distortion of a Gaussian beam transmitted through a nonlinear optical medium. In this technique, the transmitted beam intensity is recorded for a step by step translations of the nonlinear medium along the beam direction around the focus beam point from –z to +z position and the recorded transmitted beam data is then fitted with transmitted beam formula to extract all the nonlinear optical parameters. In the present thesis, nonlinear optical behavior of the films was studied using a similar Z-scan setup. A schematic diagram of the Z-scan setup is shown in fig. 2.8. He-Ne laser (MELLES GRIOT 05-LHP- 927, power: 32 Watt) of wavelength 632.8 nm was used as the laser source which was focused onto the film surface using a bi-convex lens of focal length of 5 cm. The film was placed on a translation stage which was translated in a step of 1 mm on both sides (from -15 mm to 15 mm with respect to the focused point of the lens) along the optical axis of the focused laser beam. The transmitted beam passing through the sample was collected by a CCD camera (PCO PixelFly) connected with a computer. The transmitted laser beam through the film was recorded at every step of translation of the sample by 1 mm with respect to the focal plane. During experiment, a neutral density (ND) filter was set before CCD to avoid its

saturation by high intensity laser beam. The unwanted scattered light was blocked from entering into CCD by placing an iris diaphragm before ND filter. The transmitted beam intensity is equivalent to the integrated gray values of recorded images as measured by the MATLAB programming. The total transmitted beam is considered as open aperture Z scan transmitted beam. For the closed aperture (CA) Z-scan, the images were extracted from the full-size images (open aperture) by implementing an optimized size soft aperture using the MATLAB program. The aperture size was adjusted at a certain value so that the ratio of integrated intensity of the image with aperture to that of full image was, $S \sim 0.4$, the optimum aperture size to determine the nonlinear refraction coefficient with good accuracy. Thus, the Z-scan setup provides open as well as closed Z-scan data by a single recorded data only. Figure 2.9 shows the photograph of the Z scan experimental setup. Figure 2.10 (a) and (b) shows a typical open aperture and close aperture transmitted beam images.

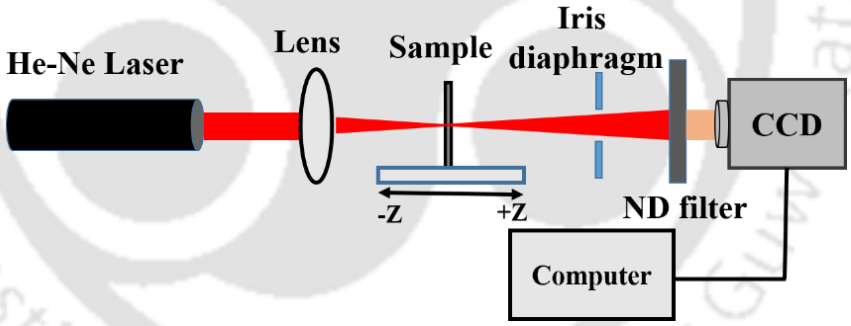

Figure 2.8 Schematic diagram of Z-scan experimental setup.

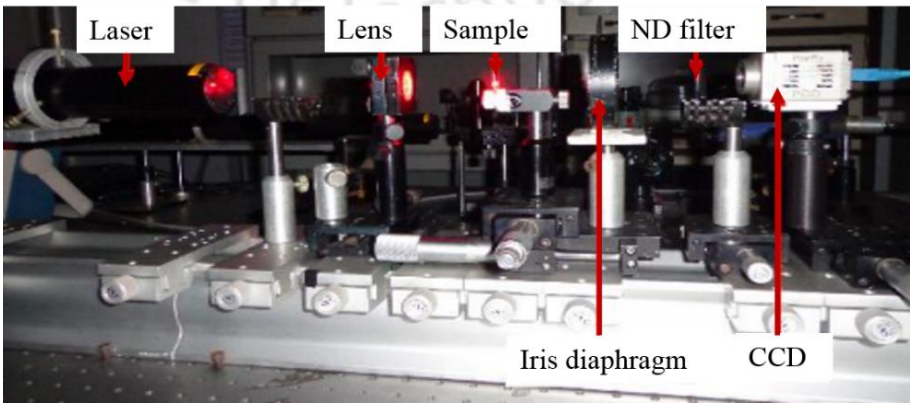

2.9 Photograph of Z scan setup.

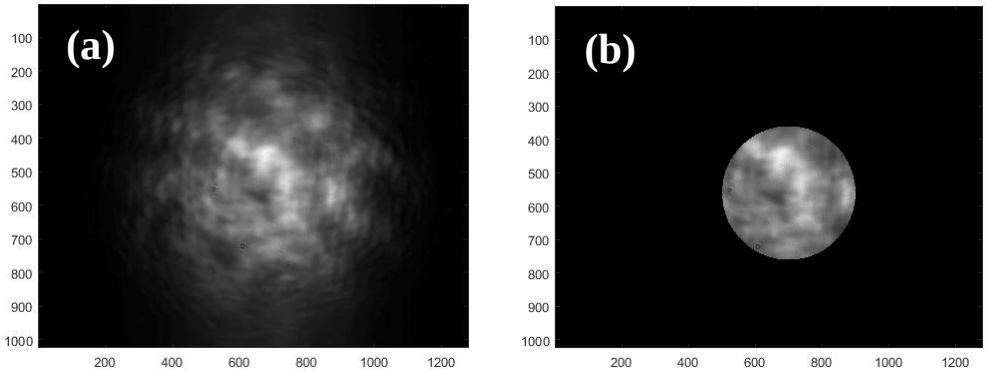

Figure 2.10 Images of (a) open and (b) closed Z-scan transmitted beam.

The nonlinear absorption coefficient (NLA) and nonlinear refractive index (NLR) coefficient of the MoS_2 and WS_2 films were obtained by fitting the open and closed aperture transmitted beam recorded at different positions with the respective position-dependent transmitted intensity formulae. The transmittance beam passing through the sample is expressed as [114,115]

$$T_{op} = 1 - \frac{c}{(1+bz^2)} \tag{2.1}$$

$$T_{cl} = 1 + \frac{4az}{(1+bz^2)(9+bz^2)} \tag{2.2}$$

where, T_{op} and T_{cl} are normalized transmissions for the open aperture *Z*-scan and close aperture Z-scan, $c = \beta' I L_{eff}/2^{3/2}$, $a = 2\pi n_2 I L_{eff}/\lambda z_{0,}$ $b = 1/{z_0}^2$, β' and n_2 represent the nonlinear absorption coefficient and nonlinear refraction coefficient of the sample, *I* is the intensity of the laser beam at the focus point, z_o is the Rayleigh length and L_{eff} is the effective thickness of the WS_2 film which is given by the equation

$$L_{eff} = \frac{1-\exp(-\alpha L)}{\alpha} \tag{2.3}$$

where, α and *L* are the linear absorption coefficient and average film thickness, respectively. The value of *L* was measured by ellipsometer and surface profilometer. Further, the linear

absorption coefficient (α) at the laser wavelength (632.8 nm) was extracted from the UV-Vis spectra of the respective films. The Rayleigh length (z_o) is constant for a fixed z scan setup. $z_o = \pi\omega_0^2/\lambda$, where ω_0 is the beam waist and λ is the wavelength of the laser source. In the present study $\omega_0 \sim 20.6$ μm and laser was He-Ne laser of $\lambda \sim 632.8$ nm. The Rayleigh length is estimated ~ 2.1 mm. Rayleigh length of the setup is much larger than the thickness of the films which satisfy the thin film approximation condition of the experiment. The focused beam intensity (I) was ~1.11 kW/cm^2. Thus, using equation (2.1) and (2.2), one can extract β and n_2 of the thin films.

The real (χ_R^3) and imaginary (χ_I^3) third-order nonlinear optical susceptibility of the films were obtained using the following equations [114]

$$\chi_R^3 = 10^{-7}\frac{nc}{12\pi^2}(nn_2 - kk_2) \quad (2.4)$$

$$\chi_I^3 = 10^{-7}\frac{nc}{12\pi^2}(nk_2 + kn_2) \quad (2.5)$$

and corresponding third-order nonlinear optical susceptibility (χ^3) from

$$\chi^3 = \sqrt{(\chi_R^3)^2 + (\chi_I^3)^2} \quad (2.6)$$

where n is the linear refractive index, k (= $\frac{\alpha\lambda}{4\pi}$) is the linear extinction coefficient and k_2 (= $\frac{\beta\prime\lambda}{4\pi}$) is the nonlinear extinction coefficient. The calculated values of n_2, β', χ_R^3, χ_I^3 and $\boldsymbol{\chi^3}$ of the MoS_2 and WS_2 films are reported in tables 5.1 and 5.2 in chapter 5.

2.7 HER experimental setup

The MoS_2 and WS_2 thin films and QDs were used as a working electrode to verify their effectiveness as an active electrocatalyst for HER. A schematic diagram of the HER experimental setup is presented in fig. 2.11. The experiment was performed with an

electrochemical analyzer (model-CHI1120B) in a three-electrode configuration. HER activity of the samples was evaluated in an electrolyte solution of 0.5 H_2SO_4 (pH = 0) at room temperature (24° C). During the experiment, MoS_2 and WS_2 thin films deposited onto FTO substrate and MoS_2 QDs drop cast onto glassy carbon electrode (GCE) were used as working electrode (WE), Ag/AgCl (aq) was used as reference electrode (RE) and a Pt wire was used as counter electrode (CE). The experimentally applied potential was converted into reversible hydrogen electrode (RHE) potential using the following relation

$$E_{RHE} = E_{Ag/AgCl} + 0.059\, pH + E^0_{Ag/AgCl} \quad (2.7)$$

where E_{RHE} represent the potential vs RHE, $E_{Ag/AgCl}$ is the experimentally measured potential, $E^0_{Ag/AgCl}$ is the standard potential across the Ag/AgCl electrode, and pH is the pH value of the electrolyte solution.

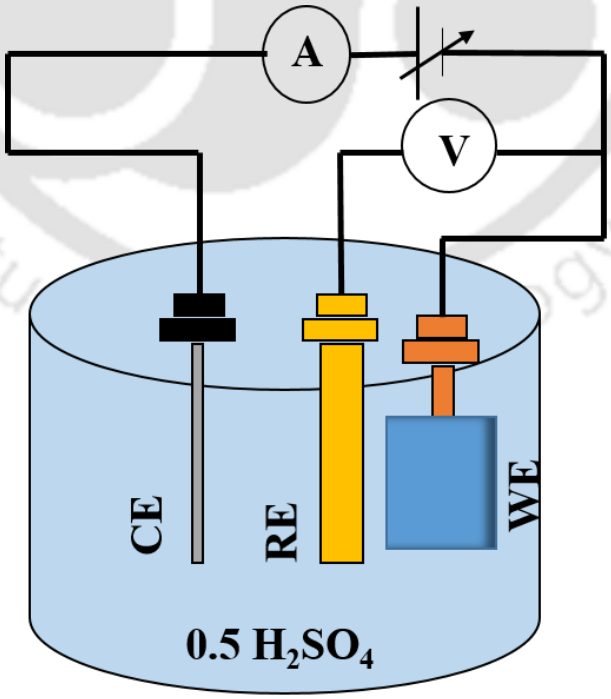

2.11 Schematic diagram of three electrode HER setup.

2.8 Characterization techniques

The following diagnostic techniques were utilized to characterize the crystallinity, morphology, nanostructure and optical properties of MoS_2 and WS_2 thin films as well as QDs.

Stylus profilometer: The film thickness was measured using stylus profilometer (Veeco Dektak 150). The profilometer provides 4 angstrom measurement repeatability.

X-ray diffraction: The crystallinity of the deposited films was analyzed by recording X-ray diffraction (Rigaku, model TTRAX III) pattern at 3 degrees/min scanning speed with a step size of 0.03°. The X-ray source was CuK_α line (λ = 1.5406Å). Along with crystalline phase, other information like crystalline size, lattice parameters, stress and strain in the film were also determined using the XRD pattern.

Raman spectroscopy: Raman and PL spectra were recorded (Horiba Jobi Yvon, LabRam HR 800) in the backscattering geometry using an excitation wavelength of 488 nm (Ar-ion laser). The exciting laser was focused onto the sample with the 100X objective lens. The spatial resolution of the Raman measurement was ~ 1 μm and the spectral resolution was ~ 0.62 cm^{-1}. The PL spectra were measured with a spectral resolution of 0.013 nm. Raman spectra are extensively used for 2D materials to determine number of layers, crystallinity and defect state, stress-strain in the films.

Field emission scanning electron microscope (FESEM): Surface morphology of the films was investigated by analysis the FESEM images (recorded by Sigma, Zeiss). Prior to every measurement, the films were coated with fine gold layers to avoid charging effect during measurement.

Energy dispersive X-Ray spectroscopy (EDX): Thin films elemental components and their atomic ratio were measured by EDX spectroscopy (Sigma Zeiss).

Field emission transmission electron microscope (FETEM): Transmission electron microscopy (JEOL-JEM 2100, 2100F operating voltage 200 kV) was performed to analyze the particle size and crystallinity of the deposited films and QDs. Along with the TEM images, high-resolution TEM images (HRTEM) and SAED patterns of MoS_2 and WS_2 nanostructures were also collected during the measurement. MoS_2 and WS_2 Nanostructures were observed in TEM images and crystallinity of the nanostructure was determined by HRTEM and SAED pattern.

Atomic force microscope (AFM): The surface morphology of all the films was recorded via AFM (Bruker- Innova) to image the surface morphology, determine thin film height profile, and to study the dynamic scaling and growth mechanism of MoS_2 and WS_2 films deposited via PLD technique**.** All the measurements were performed in non-contact mode. The AFM images were collected over the surface area of 2 μm × 2 μm. The 2 μm size images were recorded by 512 number of line scan where the resolution of each line scan was 2/512 μm or 3.90 nm.

UV-VIS-NIR spectrometer: UV - VIS - NIR Spectrophotometer (*Perkin Elmer-Lambda 950*) was used to measure absorption spectra and diffuse reflectance spectra (DRS). All the spectra were recorded in the range of 200-1200 nm with the spectral resolution of 1 nm.

Fluorescence spectrometer: The PL (*Horiba Jobin Yovon Fluoromax4*) measurement of the QDs solutions was carried out over various excitation wavelengths from 290 to 390 nm with the spectral resolution of 1 nm. Xenon lamp was used as an excitation source.

Spectroscopic ellipsometry: The spectroscopic ellipsometry (SE) measurement was performed to explore the linear optical behavior of the MoS_2 and WS_2 thin films. Figure 2.12 shows the schematic diagram of spectroscopic ellipsometer and figure 2.13 shows the photograph of the ellipsometer setup (model: Semilab GES5-E). In any ellipsometric experiment, the changes in the state of the polarization of an incident beam, upon reflection

from the sample surface, is measured. The changes are expressed in terms of two parameters, ψ, and Δ, given by the following equation,[116]

$$\rho = \frac{r_p}{r_s} = \left|\frac{r_p}{r_s}\right| e^{i(\Delta_p - \Delta_s)} = tan\psi e^{i\Delta} \quad (2.8)$$

where r_p and r_s are the Fresnel reflection coefficients for a plane wave polarized parallel (p) and perpendicular (s) to the plane of incidence, respectively while Ψ and Δ are the ellipsometric angles.

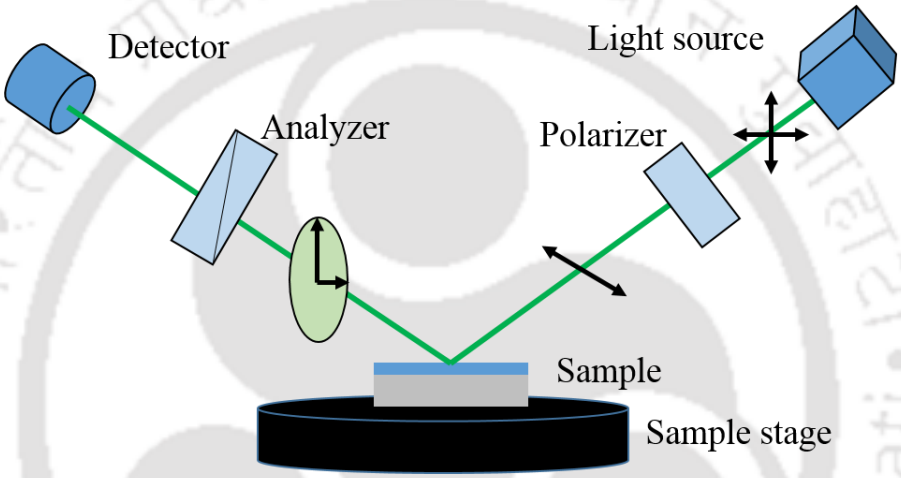

2.12 Schematic diagram of ellipsometer setup.

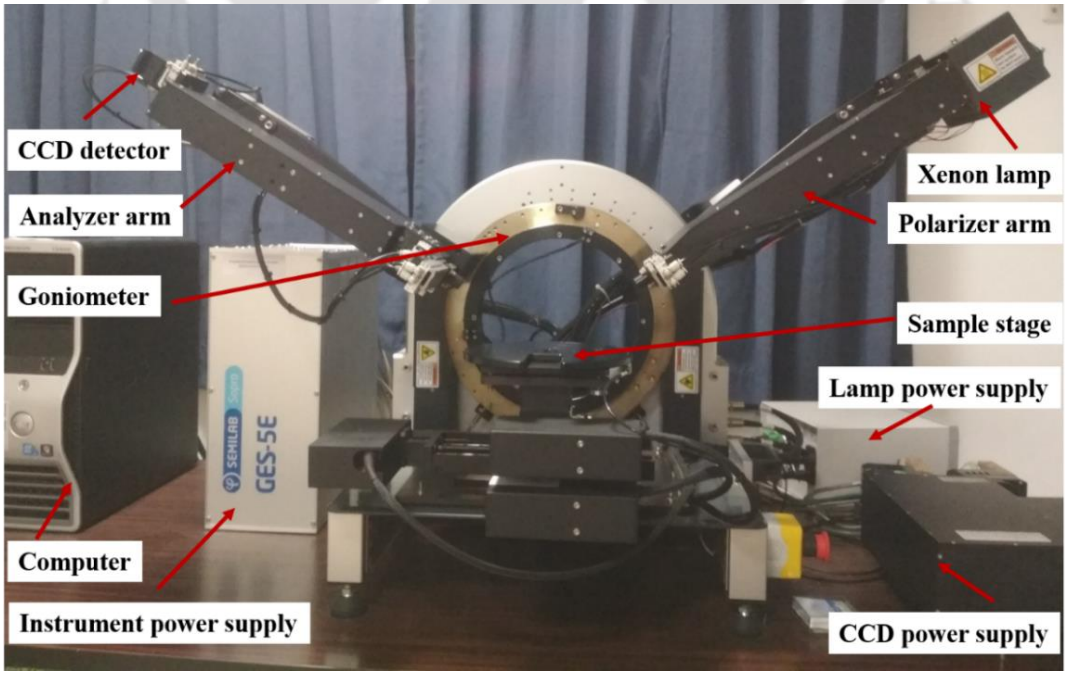

Figure 2.13 Photograph of spectroscopic ellipsometer setup.

Ψ is the angle whose tangent gives the ratio of the magnitude of the reflection coefficient of electric field components along the *p* and *s* polarization and Δ gives the difference between the phase shifts of electric field components of *p* and *s* polarizations, Δ_p and Δ_s, experienced upon reflection. The ellipsometric parameters cos (Δ) and tan (ψ) are directly recorded as a function of wavelength at different angles of incidence. In the particular case of an abrupt interface between two semi-infinite media the ellipsometric data are related to the pseudo complex dielectric function ε by the following relation [116]

$$\varepsilon = \varepsilon_1 + i\varepsilon_2 = sin^2\Phi\{1 + [(1-\rho)/(1+\rho)]^2 tan^2\Phi\} \qquad (2.9)$$

where Φ is the angle of incidence. Using equation (2.8) and (2.9), the real (ε_1) and imaginary (ε_2) part of pseudo dielectric function can be expressed as a function of Δ and ψ. Hence refractive index (*n*) and extinction coefficient (*k*) spectra can also be estimated from ellipsometric parameters (Δ and ψ). These spectra are fitted to appropriate optical models and suitable layered structure to obtain the parameters of the dispersion model, thickness, *n*, and *k*. The goodness of fitting of the experimental data (E) with the optical dispersion model (S) is presented by 'root mean square error' expressed as

$$RMSE = \sqrt{\frac{1}{3m-l}\sum_{i=1}^{m}[(N_{E_i} - N_{S_i})^2 + (C_{E_i} - C_{S_i})^2 + (G_{E_i} - G)^2]} \times 1000 \qquad (2.10)$$

where *m* and *l* are the numbers of measured wavelength and number of fit parameters. The other parameters *N*, *C* and *G* are defined as cos(2Ψ), sin(2Ψ)cos(Δ) and sin(2Ψ)sin(Δ), respectively. Levenberg- Marquardt nonlinear regression algorithm is usually applied to minimize the RMSE value in fitting of the SE spectra [116].

In the present thesis, the SE measurements were carried out over the spectral range of 1.32–3.50 eV using Variable Angle Spectroscopic Ellipsometer (*Semilab SOPRA: GES-5E*) equipped with goniometer at incident angles of 65°, 70°, and 75°. Data acquisition and analysis

were performed using spectroscopy ellipsometry analyzer (*SEA*) software. The analysis of SE data was carried out by screening several realistic physical models for semiconductors to obtain the best fit. In the present case, only the SE spectra recorded at incident angles of 70° is presented though the corresponding spectra at incident angles of 65°and 75° were also fitted with the same modeling which exhibited almost similar results.

2.9 Conclusion

In this chapter, the experimental setups used for the deposition of thin film and nanoparticle synthesis are discussed. Various characterization tools used in the present study for layered thin films to QDs are also discussed.

Chapter 3

MoS_2 and WS_2 monolayer to multilayered thin films synthesis by pulsed laser deposition

3.1 Introduction

Possessing a large scale of applications, the controlled synthesis of layered MoS_2 and WS_2 films is gaining momentum. The 2D layered films of MoS_2 and WS_2 have been synthesized by various techniques. Among different approaches, mechanical exfoliation from a geological bulk sample is a promising technique to obtain good structural layered MoS_2 film [44]. In this technique, it is a challenge to get control over the film thickness and exfoliate a large area film, though, large area MoS_2 film grown via chemical vapor deposition (CVD) technique has been reported in the literature [65-67]. The control over film thickness in a systematic manner remains a problem. In PLD technique one can easily control the film thickness using different number of laser pulses. In the present work, monolayer to multilayer MoS_2 and WS_2 thin film are deposited using PLD onto SiO_2/Si substrate by varying the deposition time and laser fluence. The number of layers and thickness of the films are measured by Raman spectroscopy and AFM image height profile. Crystallinity of the films is studied by XRD pattern and TEM image analysis. Optical behavior is characterized by photoluminescence spectra, UV-vis spectra and ellipsometer spectra of the respective thin films. Along with 2H phase, 1T structured MoS_2 phase is also detected in the MoS_2 films. 1T phase shows metallic character with a volatile nature and can easily be transformed into 2H phase with high-temperature treatment. In the present work, a 2H-1T mixed-phase mono and few-layered MoS_2 film has been realized by PLD in a very short time span of only 20 sec at various deposition

temperatures. The tunability of the ratio of the two phases with deposition temperature as well as deposition time is investigated extensively.

3.2 Experimental details

MoS_2 and WS_2 thin films were deposited using PLD technique where sintered MoS_2 and WS_2 pellets were used as the target. The PLD setup was described in detail in chapter 2, section 2.4. MoS_2 films were deposited onto SiO_2/Si substrate heated to 600 ℃ under vacuum ($\sim 5 \times 10^{-6}$ mbar) for the time duration of 14, 24, 30 sec and 6 minutes. To study the effect of substrate temperature on the crystalline phase of the films, the experiment was performed at the substrate temperatures of room temperature (RT ~25 ℃), 300, 400, 500, 600 and 720 ℃ with 200 number of laser pulses (20 sec deposition time) while all others parameters were kept constant. After 10 minutes of completion of deposition, the substrate was cooled down to room temperature at the cooling rate of 5°/min. Further MoS_2 films were deposited onto various substrate to study the effect of substrate on phase ratio. The WS_2 films were deposited onto SiO_2/Si substrate heated to 400 ℃ under vacuum ($\sim 5 \times 10^{-6}$ mbar). The substrate was kept 5 cm away from the target. WS_2 films were deposited for the time duration of 1 minute at the laser energy of ~ 20, 25 and 30 mJ while other parameters were kept constant.

3.3 Layered MoS_2 films deposition by PLD

3.3.1 Determination of the number of layers of MoS_2 thin films

Raman spectroscopy is a useful tool to determine the film thickness of a few layered 2D materials [117]. MoS_2 shows four first-order Raman active modes. Among them, E^1_{2g} and A_{1g} Raman modes show layer sensitive peak position. The blue shift of A_{1g} and red shift of E^1_{2g} with an increase in the number of layers from monolayer to higher order is reported for MoS_2 films [117]. The blue shift and the red shift of the two Raman modes increases the peak position difference (ΔF) between A_{1g} and E^1_{2g} from 20.5 cm^{-1} for monolayer to 25.5 cm^{-1} for bulk

MoS_2. Figure 3.1(a) shows the Raman spectra of the MoS_2 films deposited for 14, 24, 30 sec and 6 minutes. Each spectra exhibit twin peaks corresponding to A_{1g} and E^1_{2g} Raman modes of MoS_2. Raman peaks position and their difference of the deposited films are shown in fig. 3.1(b). The peak positions corresponding to A_{1g} were observed at 405.6, 406.3, 406.9 and 407.5 cm^{-1} while that corresponding to E^1_{2g} at around 385.1, 383.9, 383.2 and 382.6 cm^{-1} for the films deposited for the time duration of 14, 24, 30 sec and 6 minutes, respectively. ΔF in the respective films was found to be 20.5, 22.4, 23.7 and 24.9 cm^{-1}, corresponding to monolayer, bilayer, trilayer and bulk-like MoS_2 films which is in accordance with the literature [44].

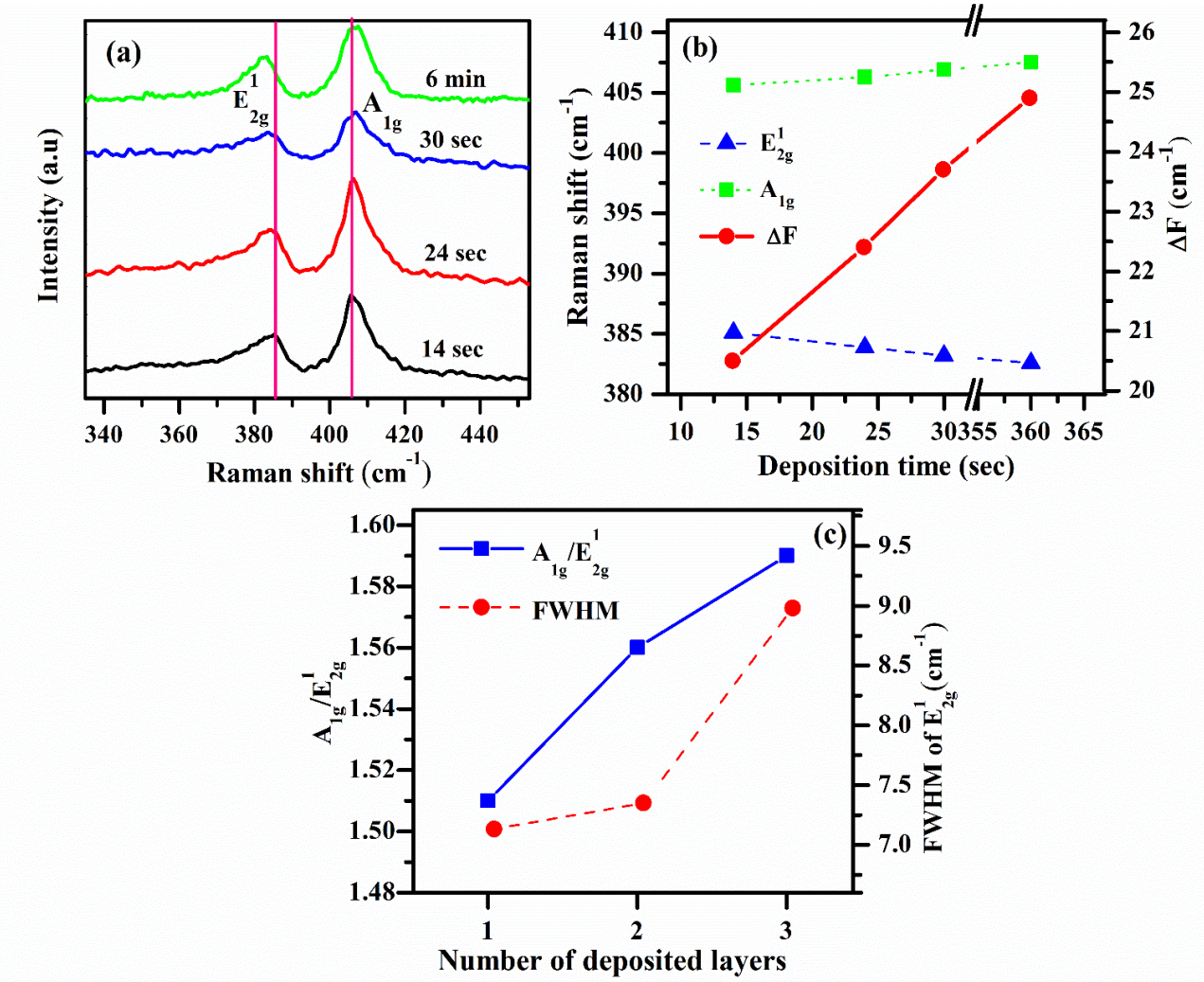

Figure 3.1. (a) Raman spectra of monolayer, bilayer and trilayer MoS_2 films, (b) Raman peak positions and their difference with respect to the deposition time and (c) FWHM of E^1_{2g} and A_{1g}/E^1_{2g} intensity ratios of the films with number of deposited layers.

The Raman peaks are observed to be blue shifted compared to mechanically exfoliated MoS_2 films [117]. The blue shift in E_{2g}^1 mode of monolayer, bilayer, and trilayer MoS_2 films were 0.6, 0.6, 0.0 cm^{-1} while for the A_{1g} mode were 2.8, 0.8 and 0.4 cm^{-1}, respectively. It is observed that the shift is maximum for monolayer and it becomes insignificant with the increase in the number of MoS_2 layers. The vibration energy varies proportionally to the square root of force constant. Increase in the out-of-plane compressive strain as confirmed by XRD studies, is the cause of higher force constant of lattice vibration, resulting in the blue shift in Raman modes [118,119]. Figure 3.1(c) shows the full width at half maxima (FWHM) of E_{2g}^1 mode and the amplitude ratio of the two Raman modes A_{1g} and E_{2g}^1. A_{1g} Raman peak intensity is higher than that of E_{2g}^1 for all the films which is consistent with the literature on MoS_2 films grown by PLD [94]. The reduction in A_{1g}/E_{2g}^1 peak ratios and FWHM of E_{2g}^1 modes are attributed to better crystalline structure [65,89,120]. The FWHMs of E_{2g}^1 are 7.13, 7.35 and 8.98 cm^{-1} while A_{1g}/E_{2g}^1 peak ratios are 1.51, 1.56 and 1.59 for monolayer, bilayer and trilayer films, respectively. Both the FWHM and peak intensity ratios are enhanced with the number of deposited layers. This result suggests that crystalline quality has been reduced with increasing the number of layers. This result can be understood with the help of nucleation and growth theory. At the initial growth stage of the film, lateral growth takes place following "Frank-Van Der Merwe" model [121] and results in a uniform monolayer with higher crystallinity. But with an increase in deposition time the vertical growth of the film dominates over lateral growth which results in a thoroughly distributed islands formation [122] over the higher layered MoS_2 film following Stanski-Krastanov growth model [121]. With the presence of island, the uniformity of bilayer and trilayer decreases which causes a reduction in the crystallinity. A large number of island formation over the bilayer film and the reduction of crystallinity of the corresponding film was confirmed by TEM and XRD analysis presented in section 3.3.2.

Further, the height profile of the films was measured by analyzing AFM images. During deposition a silicon mask was used on a portion of the substrate; as a result, a clear junction of bare substrate and deposited film was created. AFM image was collected from this junction area to obtain the height profile of the deposited film with respect to the bare substrate. Fig. 3.2(a) and fig. 3.2(b) represent typical height profile of MoS_2 films deposited for 14 and 24 sec, respectively. The inset shows corresponding AFM image of the masked and unmasked area of the film. The height profile extracted from AFM images shows that the film thicknesses are 0.75 and 1.4 nm which indicates deposition of the monolayer and bilayer MoS_2 films [123].

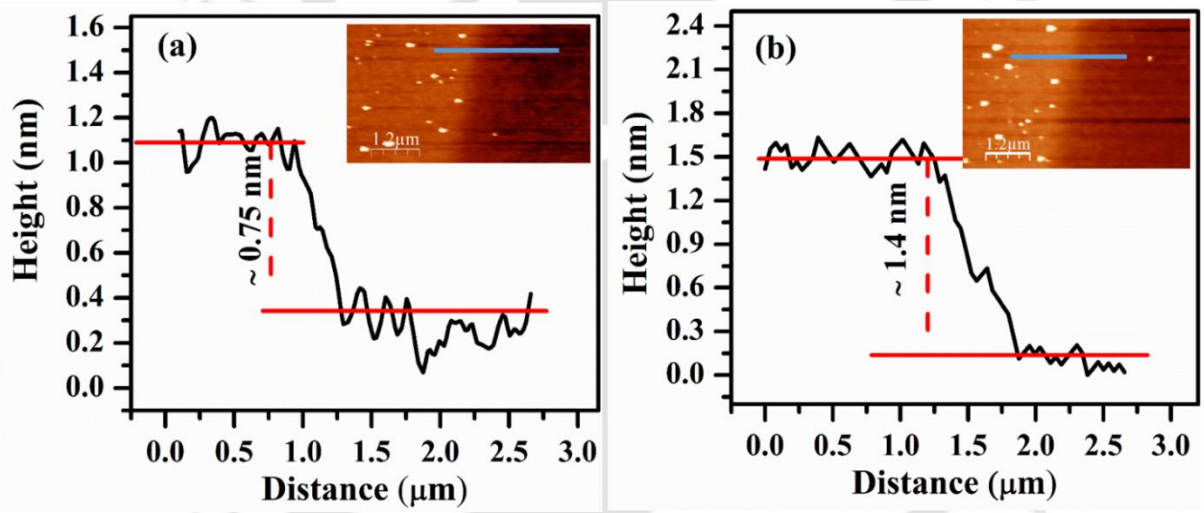

Figure 3.2 AFM height profile of (a) monolayer and (b) bilayer MoS_2 films deposited on SiO_2/Si substrate. The insets are the AFM images of the respective films.

3.3.2 Characterization of Crystalline structure of MoS_2 thin films

XRD patterns of layered MoS_2 films along with MoS_2 pellet and the bare SiO_2/Si substrate were collected in grazing incident angle mode. Figure 3.3(a) and 3.3(b) show the XRD patterns of MoS_2 pellet and the bare SiO_2/Si substrate while Fig. 3.3(c) and 3.3(d) shows the XRD pattern of monolayer and bilayer MoS_2 films deposited on SiO_2/Si substrate. XRD pattern of SiO_2/Si substrate shows a broad amorphous like peak at 23° while MoS_2 pellet shows

peaks at 14.52°, 29.13° and 44.28° corresponding to (002), (004), and (006) crystal planes of MoS_2. The pellet exhibits highly crystalline behavior with *c*-axis orientation. XRD pattern of monolayer and bilayer films also shows *c*-axis epitaxial growth with the presence of (002) peak. The crystallite size of the films was estimated with Debye-Sherrer formula,

$$D = \frac{0.89\lambda}{\rho Cos\theta} \tag{3.1}$$

where D is the average crystallite size, ρ is the FWHM of XRD peak and θ is the diffraction angle of the corresponding peak. Being highly intense, (002) peak was used to determine the average crystallite size using Debye-Sherrer formula. The deposited monolayer MoS_2 film shows a higher average crystallite size of 40.2 nm than that of the bilayer MoS_2 film which was found to be 29.3 nm.

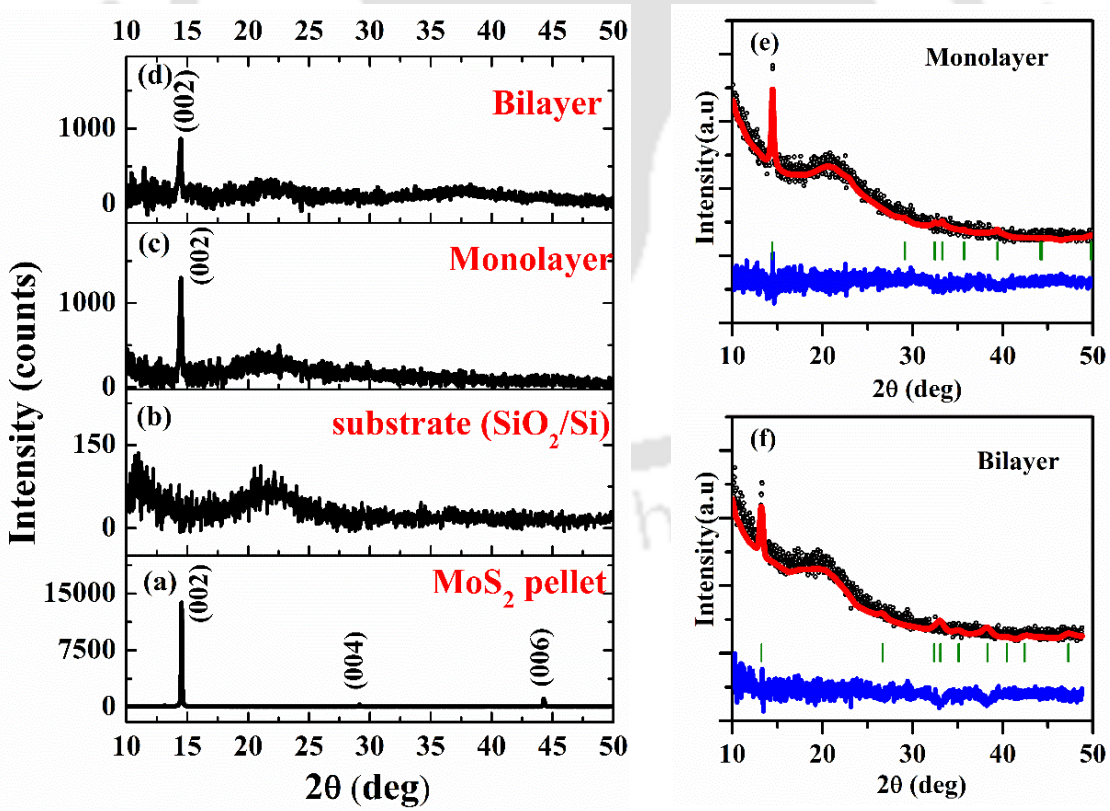

Figure 3.3 XRD patterns of (a) MoS_2 pellet, (b) Bare SiO_2/Si substrate, (c) Monolayer of MoS_2 and (d) Bilayer of MoS_2. Riet-Veld refinement of (e) Monolayer and (f) Bilayer MoS_2 films. The blue lines are the difference between the measured and simulated spectra.

The Riet-Veld refinement of the diffracted spectra were performed with the help of Full Prof Program, which confirmed the crystalline MoS_2 film growth with P63/mmc phase. Figure 3.3(e) and 3.3(f) are the Riet-Veld fitted XRD patterns of monolayer and bilayer MoS_2 films, respectively. The lattice parameters of the layered films were obtained by Riet-Veld refinement. The crystallite size, space group and lattice parameters (*a* & *c*) are listed in table 3.1. From table 3.1, it is evident that the lattice parameters *a* and *b* of the monolayer are larger than the bilayer and pellet (bulk) while *c* parameter of the monolayer is shorter than the bilayer and pellet. This suggests that the films experienced an in-plane tensile strain and out-of-plane compressive strain. This compression of the MoS_2 sheet could be due to its adhesion to the substrate.

Table 3.1 Space group, lattice parameters and crystallite size of MoS_2 pellet and films

MoS_2 Sample	**Space group and Crystal structure**	**Lattice parameters (Å)**	**Crystallite size (*D*) (nm)**
Pellet	P63/mmc	$a = b = 3.16$	103.0
	Hexagonal	$c = 12.30$	
Monolayer	P63/mmc	$a = b = 3.18$	40.2
	Hexagonal	$c = 12.25$	
Bilayer	P63/mmc	$a = b = 3.16$	29.3
	Hexagonal	$c = 12.27$	

To further elucidate the crystalline structure of the MoS_2 thin films, the TEM images of the MoS_2 film deposited for 14, 24 sec and 6 min were analyzed systematically. A uniform layer of MoS_2 with sporely populated spherical nanostructures of different sizes are shown in fig. 3.4(a). Figure 3.4(b) and fig. 3.4(c) shows the formation of bilayer and multilayer MoS_2 films deposited for 24 sec and 6 min, respectively. The TEM images of the films show low island density for monolayer but for bilayer, it increased rapidly and at higher deposition time the island density decreased by mutual coalescence. In the bulk-like MoS_2 film, multiple layers

were stacked onto each other as can be seen from TEM image. To analyze the crystalline properties of the film, the HRTEM images and selected area electron diffraction (SAED) patterns were also recorded. Figure 3.4(d) and fig. 3.4(e) are the corresponding HRTEM image with the FFT plot and SAED pattern of the MoS_2 nanostructure as depicted in Fig. 3.4(a). The *d* spacing obtained from HRTEM image was 0.27 nm corresponding to the (100) plane of MoS_2. SAED pattern shown in fig 4(d) exhibited a sharp diffraction spot corresponding to a crystalline structure.SAED pattern also confirmed (100) plane. The (100) crystalline plane was also detected in SAED pattern and HRTEM images of bilayer and multilayer MoS_2 films.

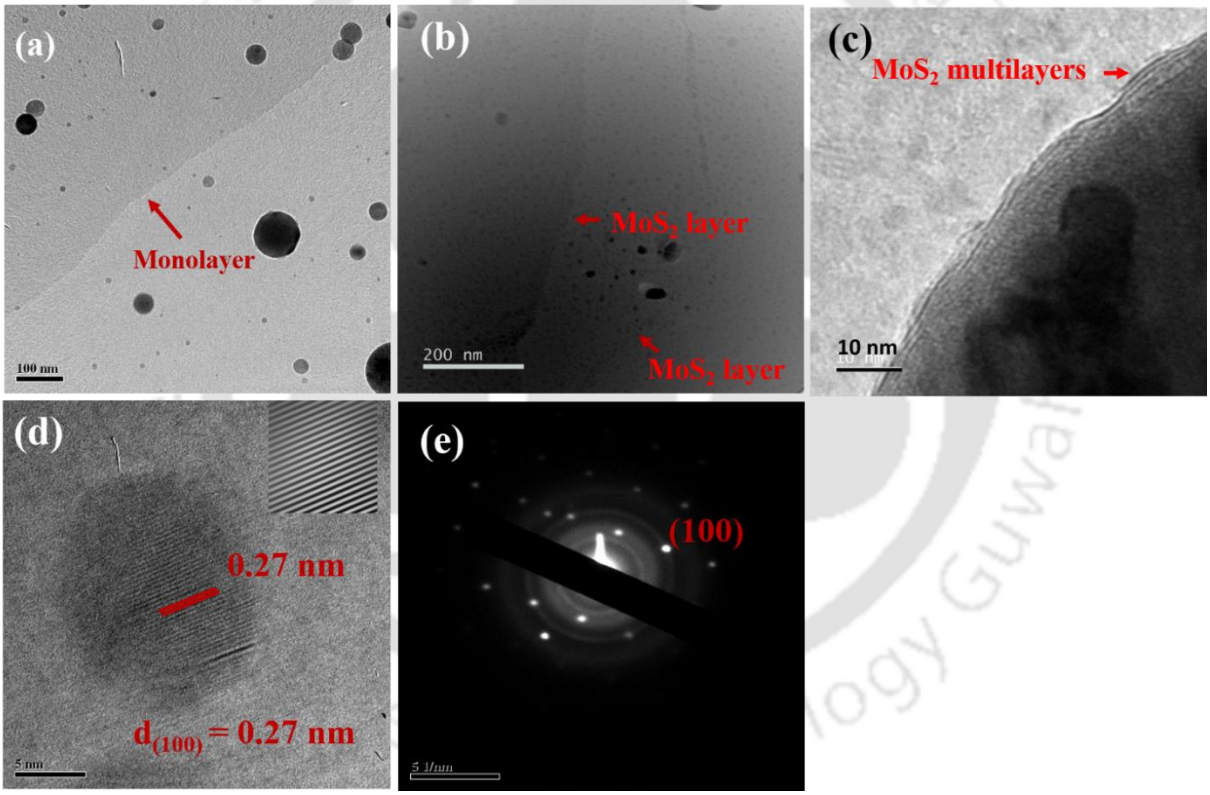

Figure 3.4 TEM images of (a) monolayer, (b) bilayer, and (c) multilayer MoS_2 film (d) HRTEM image of MoS_2 monolayer film and (e) SAED pattern.

3.3.3 Optical characterization

MoS_2 is an indirect band gap material except in monolayer form where it shows direct band gap of 1.9 eV. Due to its direct band gap nature, monolayer MoS_2 exhibits significantly

intense PL spectra. The recorded PL spectra of the MoS_2 monolayer thin film is shown in figure 3.5(a). The PL peak was observed at 1.81 eV. The PL emission of the MoS_2 films for deposition times of ~24, 30 sec and 6 min are shown in fig. 3.5(b). PL peaks at 1.78 and 1.72 eV correspond to the films deposited for 24 sec and 30 sec while the film of 6 min deposition duration did not show any significant PL emission. With an increase in the number of layers from monolayer to trilayer, the PL peak intensity decreased and peak energy shifted towards lower energy. The typical energy level diagrams of PL emission in the monolayer and bilayer MoS_2 film are shown in fig. 3.5 (c) and 3.5 (d). In monolayer MoS_2 a direct band transition

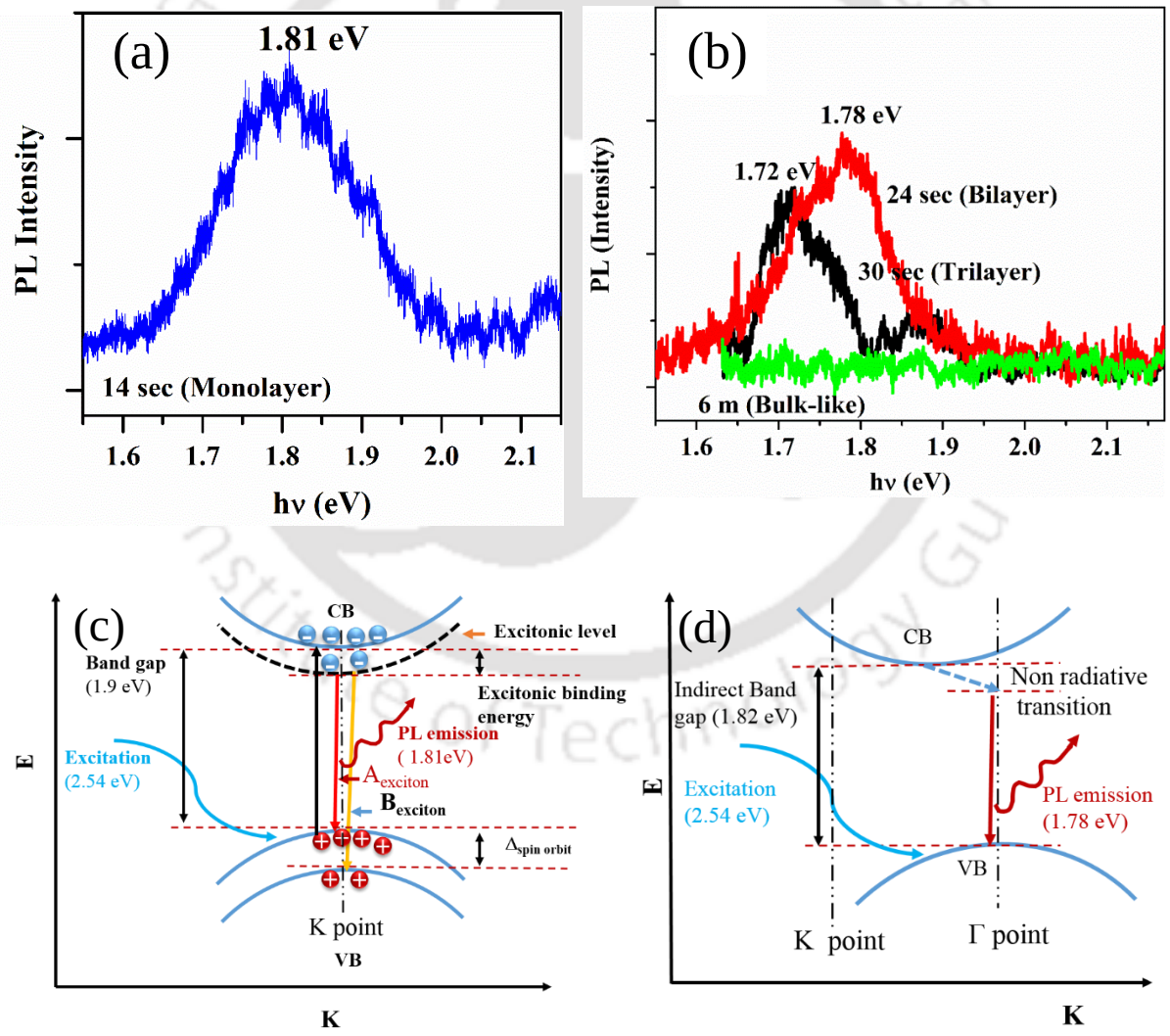

Figure 3.5 PL spectra of MoS_2 films for the deposition time of (a) 14 sec, (b) 24, 30 sec and 6 min. (c) The schematic of energy level diagram of PL emission of monolayer MoS_2 film and (d) The schematic of energy level diagram of PL emission of bilayer MoS_2 film.

occurs from conduction band minimum to valence band maximum of ~1.9 eV at the *K* point of the Brillouin zone while bilayer MoS_2 shows indirect band transition of ~1.82 eV which corresponds to the indirect transition in the Γ Brillouin zone along Γ-*K* direction [9]. In monolayer MoS_2 film, 'A excitonic' and 'B excitonic' transitions are the two possible direct optical transitions. In PL specra of chemical vapor deposited and mechanically exfoliated monolayer MoS_2 films, the 'A' and 'B' excitonic peaks were observed at 1.82 and 1.98 eV [9,124]. Thus, the PL peak at 1.81 eV (Fig. 3.5 (a)) indicates that the PL emission of the monolayer MoS_2 films is dominated by 'A' excitonic transition. In case of the indirect band gap bilayer MoS_2 film the carrier makes non-radiative transition to intermediate energy state and then radiative transition to ground state with a resulting PL emission of energy 1.78 eV. The direct-indirect band gap transition of MoS_2 films from mono- to bilayer to bulk-like structure and the weak interlayer coupling of the MoS_2 layers causes a visible reduction in the PL emission [6,125]. Due to the quantum confinement effect, the MoS_2 film shows an increase in band gap energy with a decrease in layer number from a bulk-like structure to a monolayer.

3.4 Deposition of 1T/2H mixed-phase MoS_2 thin films

It is known that single layer to a few-layered MoS_2 films shows intense PL spectra due to their direct band gap nature. In the present case, though, PL spectra were observed in the layered MoS_2 films, the spectra were noisy and less intense compared to the reported PL spectra. Hence various factors like defect in the films, metallic 1T phase, amorphous structure, etc. may be the possible causes. To investigate these causes, MoS_2 films were deposited at various deposition conditions and analyzed in detail.

3.4.1 MoS_2 thin films deposited at various substrate temperatures

The substrate temperature affects the film thickness, morphology as well as crystalline properties significantly.

(a) Raman characteristics: Figure 3.6(a) shows the Raman spectra of the MoS_2 films deposited at RT (25 °C), 300, 400, 500, 600 and 720 °C, respectively. The Raman spectra of all the films except film deposited at RT shows J_2 Raman mode corresponding to 1T phase along with the other two visibly prominent E^1_{2g} and A_{1g} modes corresponding to 2H phase of the MoS_2 films. J_2 peak originated from the motion of two zigzag S-Mo-S chains relative to each other [126]. J_2 peak appears at 227 cm^{-1} while the other Raman modes, J_1 and J_3 of 1T phase are significantly absent in the films. A pressure-dependent 1T –MoS_2 vibrational mode studied by Nayak et al. showed that at a pressure of 10 GPa, J_3 mode starts to merge with E^1_{2g} mode, resulting in a broadening in E^1_{2g} mode and J_1 mode was almost suppressed at the pressure of ~27 GPa [126]. The phenomenon was attributed to the large hydrostatic pressure on the lattice.

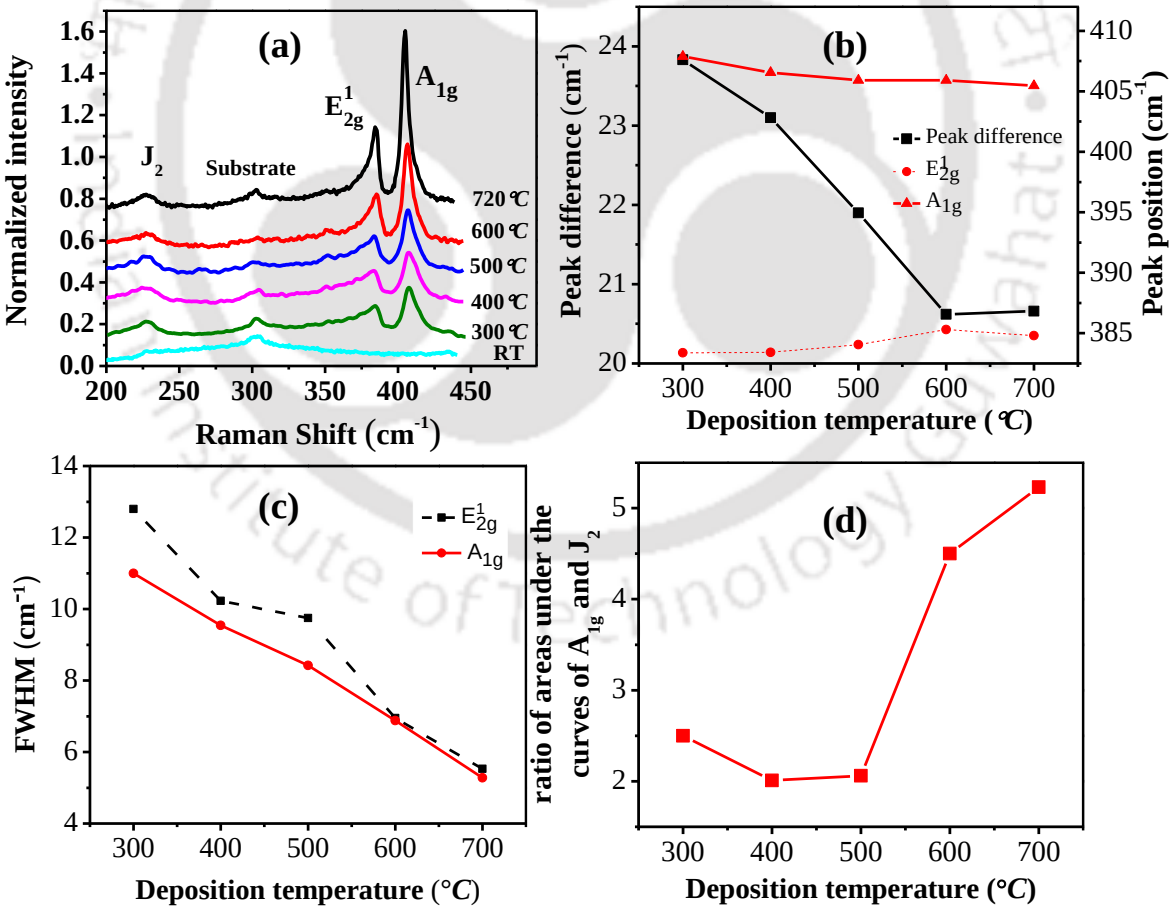

Figure 3.6 (a) Raman spectra of the MoS_2 films on SiO_2/Si substrate deposited at different temperatures for 20 sec, (b) A_{1g} and E^1_{2g} peak position and their difference, (c) Raman peak FWHM variation and (d) Ratio of the area under the A_{1g} and J_2 peak of the MoS_2 films.

Interestingly, in the present experiment, MoS_2 films deposited at high vacuum showed the same Raman characteristics. Fig. 3.6(b) shows the Raman peak position and the difference of A_{1g} and E^1_{2g} mode of the corresponding films. The A_{1g} mode frequencies were observed at 407.89, 406.55, 405.92, 405.92 and 405.46 cm^{-1} while that of E^1_{2g} modes were observed at 384.02, 383.42, 384.05, 385.30 and 384.60 cm^{-1}, of films deposited at 300, 400, 500, 720 600 and ℃, respectively. It was observed that at higher deposition temperature A_{1g} mode was red shifted while E^1_{2g} mode blue shifted i.e. Raman peak position difference (Δf) of the two modes, decreased with an increase in the deposition temperature. The frequency difference (Δf) of the two Raman modes were 23.87, 23.13, 21.88, 20.63 and 20.66 cm^{-1} for the films at the deposition temperature of 300, 400, 500, 600 and 720 °C, respectively. The Raman peaks confirmed that the films were in a few layers to monolayer regime i.e. the increase in substrate temperature led to a decrease in the film layers. Fig. 3.6(c) shows the FWHM of the two Raman modes of 2H phase of the respective MoS_2 films. The FWHMs of E^1_{2g} mode were 12.8, 9.54, 8.42, 6.88 and 5.53 cm^{-1} while the same for A_{1g} mode were 11, 10.23, 9.75, 6.95 and 5.28 cm^{-1} for the films deposited at 300, 400, 500, 600 and 720 °C, respectively. The FWHMs of the twin Raman modes decreased with an increase in the substrate temperature. The Raman peak intensity also increased monotonically with deposition temperature and the E^1_{2g}/A_{1g} peak intensity ratio was higher for the film deposited at 720 °C. For layered MoS_2 films small FWHM of the two Raman modes and the higher ratio of the amplitude of E^1_{2g} to A_{1g} corresponds to better crystalline films [89,120]. The higher substrate temperature provides activation energy for surface migration of adatoms and the phenomena help to enhance the film crystallinity by coalescence of the islands which is reflected in the result. Figure 3.6(d) shows the area under the curve (integrated intensity) ratio of A_{1g} and J_2 Raman modes. The ratio, quantify the on an average 2H and 1T phase distribution in the respective films. At 720 °C the film consisted of ~84% 2H phase which decreased to ~82, 67, 66 and 71% at the deposition

temperature of 600, 500, 400 and 300 °C, respectively. It was observed that A_{1g} to J_2 phase ratio increased with the higher deposition temperature which suggests high deposition temperature favors 2H MoS_2 film formation than 1T phase.

(b) XRD analysis: Figure 3.7 shows the XRD patterns of the MoS_2 thin films deposited at the substrate temperatures of 400, 500, 600 and 720 °C. Sharp XRD peaks corresponding to the (001) plane of 1T-MoS_2 and (002) and (006) plane of 2H-MoS_2 are visible in the films at 720 and 600 °C while a peak corresponding to (002) plane of 2H-MoS_2 was observed only in the film of 500 °C and no significant XRD peak was found in the film deposited at 400 °C. Hence it was observed that high deposition temperature improved the crystallinity in both 1T and 2H phase MoS_2. The XRD result is in agreement with the Raman mode characterization of the respective MoS_2 films where an increase in crystallinity of the films with an increase in deposition temperature was also observed.

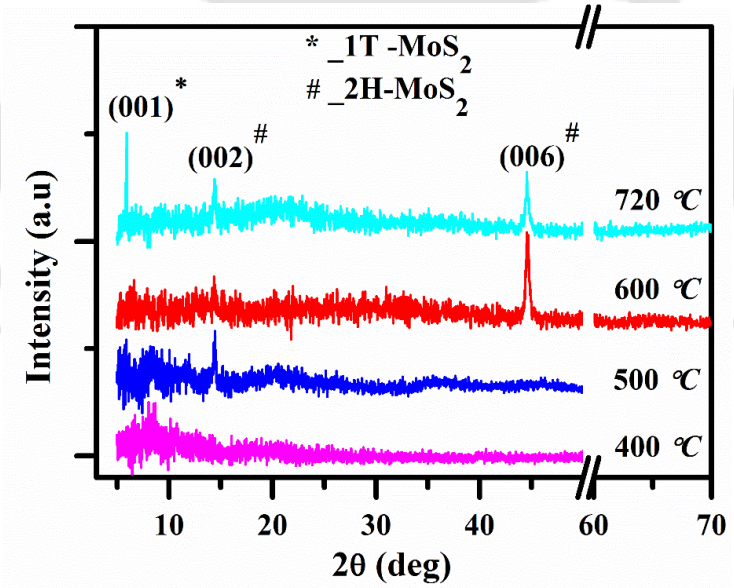

Figure 3.7 XRD patterns of the MoS_2 films deposited at various substrate temperatures.

(c) AFM analysis: Figure 3.8 shows the AFM images of MoS_2 films deposited at substrate temperatures of 300, 400, 500 and 600 °C. A clear difference in the morphology of the films deposited at different substrate temperatures was observed from the AFM images. For the film

deposited at 300 °C, sparsely distributed large-sized clusters were observed while for the film of 400 °C, a large number of clusters of comparatively smaller size are distributed throughout the substrate and for films at 500 and 600 °C the surface becomes smoother with the presence of only a few small sized nanoclusters.

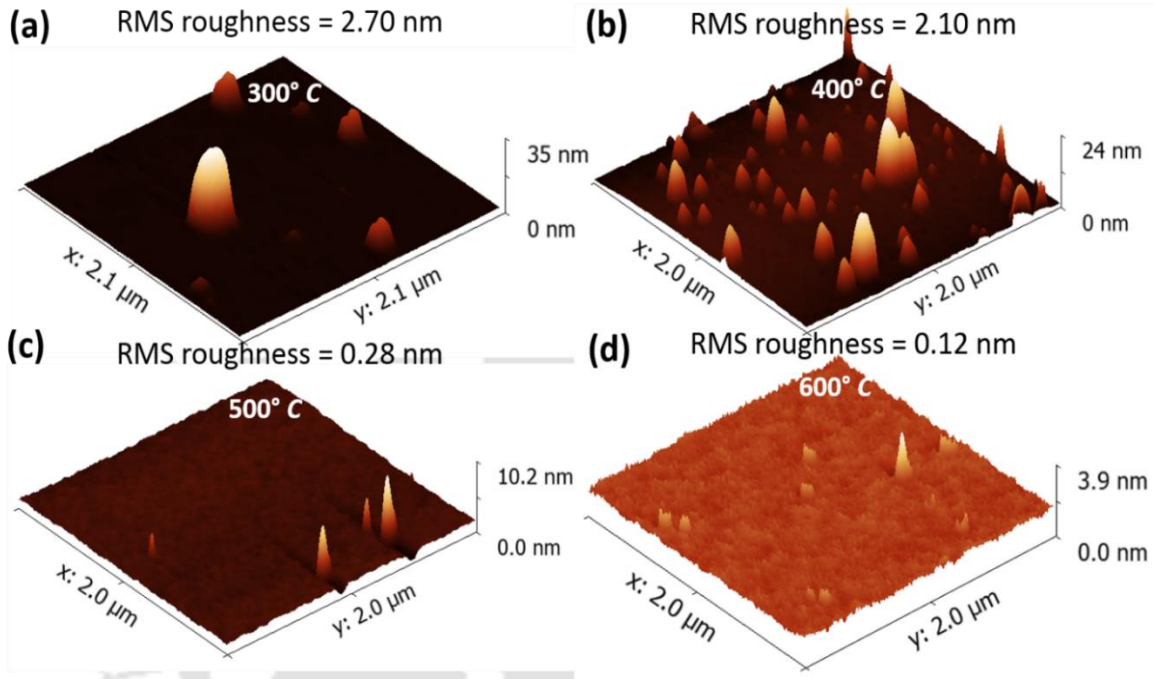

Figure 3.8 AFM images in 3D topography of the MoS_2 films deposited at (a) 300 ℃ (b) 400 ℃ (c) 500 ℃ and (d) 600 ℃.

The root means square (RMS) roughness of the films deposited at 300, 400, 500 and 600 °*C* were 2.70, 2.10, 0.28 and 0.12 nm, respectively. It was observed that the surface roughness decreased at higher substrate temperatures. So the films deposited at higher temperatures were more uniform, smoother and crystalline than the films at lower deposition temperatures as confirmed by Raman spectra and AFM images of the films. The film thickness and surface morphology of a film are regulated by the physical phenomena like sticking coefficient, re-evaporation rate of the impingement particles and surface diffusion coefficient of adatoms. With an increase in the substrate temperature the sticking coefficient decreases while the re-evaporation rate of the particle from film or substrate surface increases which leads to a

decrease in film thickness [127]. The relationship between the surface diffusion coefficient (D_S) and the temperature (T), [128] is given by

$$D_S = D_{S0}\, exp\, (-E_A/k_B T) \tag{3.2}$$

where D_{SO} is the pre-exponential factor, E_A is the activation energy for a surface-diffusion jump, k_B is the Boltzmann constant and T is the substrate temperature in Kelvin. According to equation (3.2), an increase in substrate temperature causes a high diffusivity of the adatoms which leads to the formation of a smoother surface. The experimental result also follows the same trend. The Raman and AFM analysis suggest that at 300 °C there was only three-dimensional island formation while at 400 and 500 °C, layered MoS_2 films growth took place along with the three-dimensional island and at 600 °C, two-dimensional full monolayer growth took place. So the film deposited at 300 °C followed the Volmer-Weber nucleation and growth model. Sranski-Krastanov model was followed by the films deposited at 400 and 500 °C. The growth of the film deposited at 600 °C followed the Frank-Van Der Merwe model [129].

(d) Optical microscope images: Figure 3.9 shows the optical microscope images of the MoS_2 films on SiO_2/Si substrate deposited at 300, 400, 500 and 600 °C substrate temperatures for 20 sec. Prominent color contrast is visible in between the bare substrate and deposited film area as observed in fig. 3.9(b),(upper side substrate and lower side film) 3.9(c), and 3.9(d) (left side substrate and right side film). The images show a uniform MoS_2 film formation throughout the substrate irrespective of deposition temperatures.

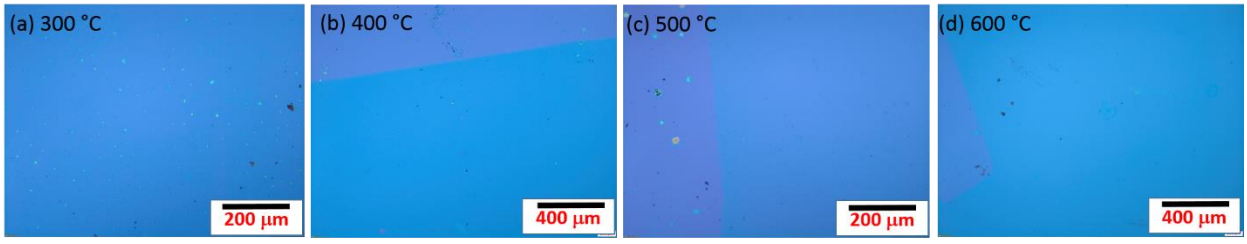

Figure 3.9 Optical microscope images of the MoS_2 films deposited at (a) 300, (b) 400, (c) 500 and (d) 600 °C.

(e) FETEM characterizations: In order to unveil the nanostructure and crystallinity of the deposited film, TEM images were analyzed. The TEM images of the MoS_2 films deposited at 400 and 720°C, where 1T/2H phase ratio is maximum and minimum, were analyzed in detail. Figure 3.10(a) represents the TEM image of the MoS_2 film deposited at 400 °C. The film was uniformly distributed throughout the substrate. Further, the HRTEM images of the films were collected to analyze the crystalline properties. Figure 3.10(b) shows the HRTEM image of the film with FFT in the inset. The *d* spacing obtained from the image was 0.225 nm corresponding to the (103) plane of 2H-MoS_2 and (201) plane of 1T-MoS_2. Figure 3.10(c) shows the SAED pattern of the MoS_2 film at 400 °C. The SAED pattern depicts a mixed 1T-2H heterogeneous phase of MoS_2 with polycrystalline nature. (004) and (100) plane of the 2H phase and (110) and (003) plane of 1T phase are visibly prominent in the SAED pattern [130,131]. Figure 3.10(d), (e) and (f) shows TEM, HRTEM and SAED pattern of the MoS_2 film deposited at 720 °C. The HRTEM image shows a prominent *d* spacing of 0.27 nm

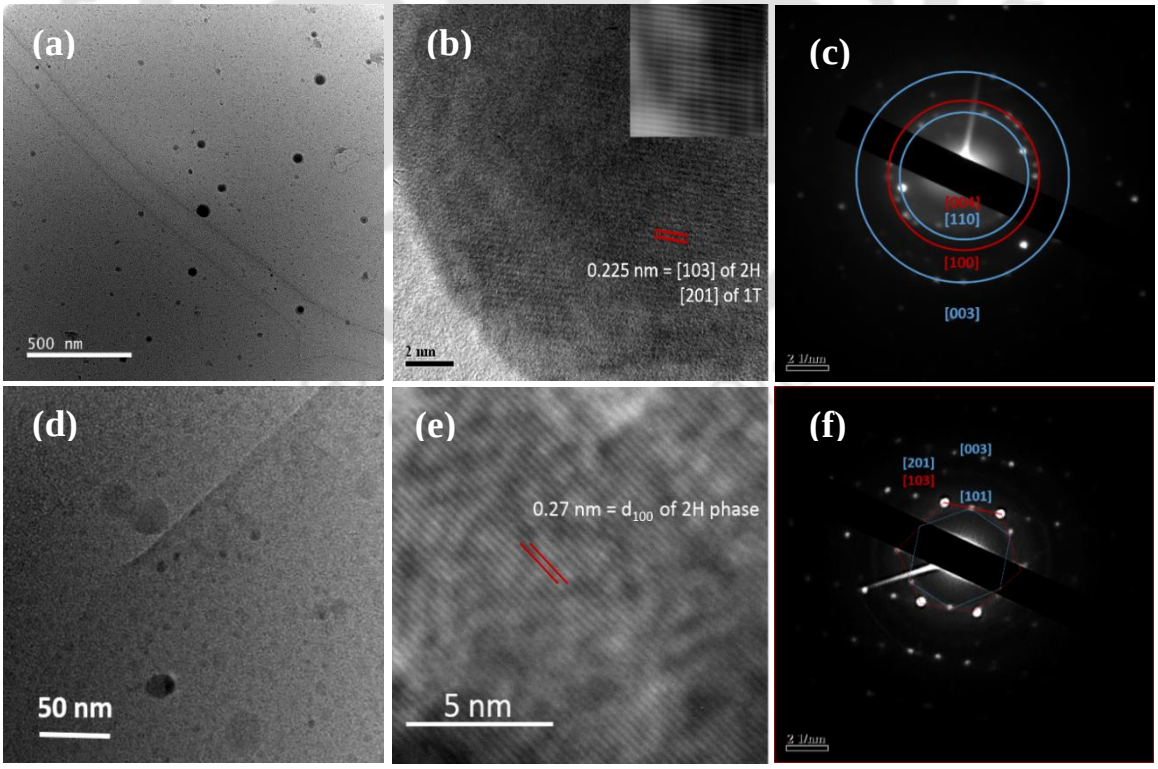

Figure 3.10 TEM analysis of MoS_2 films deposited at 400 °C (a) TEM image, (b) HRTEM image with FFT in inset, (c) SAED pattern, and at 720 °C (d) TEM image, (e) HRTEM image and (f) SAED pattern.

corresponding to the (100) plane of 2H-MoS_2. The presence of (103) plane of 2H phase with (101), (201), (003) plane of 1T was confirmed in the SAED pattern of the film at 720 °C [130,131]. It was observed that the film showed polycrystalline nature at 400 °C while the film at 720 °C showed a crystalline structure with the presence of both 1T and 2H phase.So in the light of the nucleation and growth, the higher deposition temperature leads to a uniform as well as highly crystalline film which was obtained at 720 °C for MoS_2.

(f) EDX analysis: Figure 3.11 (a), (b) and (c) shows the EDX spectra of the MoS_2 films at 300, 500 and 720 °C with inset showing atomic % of each element of MoS_2. Sulfur (S) and Molybdenum (Mo) atomic % and their atomic ratio of the respective films is presented in figure 3.11(d). The atomic percentage of S was found to be 73.1, 46.8 and 31.9% for the MoS_x thin films corresponding to x = 2.7, 0.88 and 0.47, deposited at 300, 500 and 720 °C respectively.

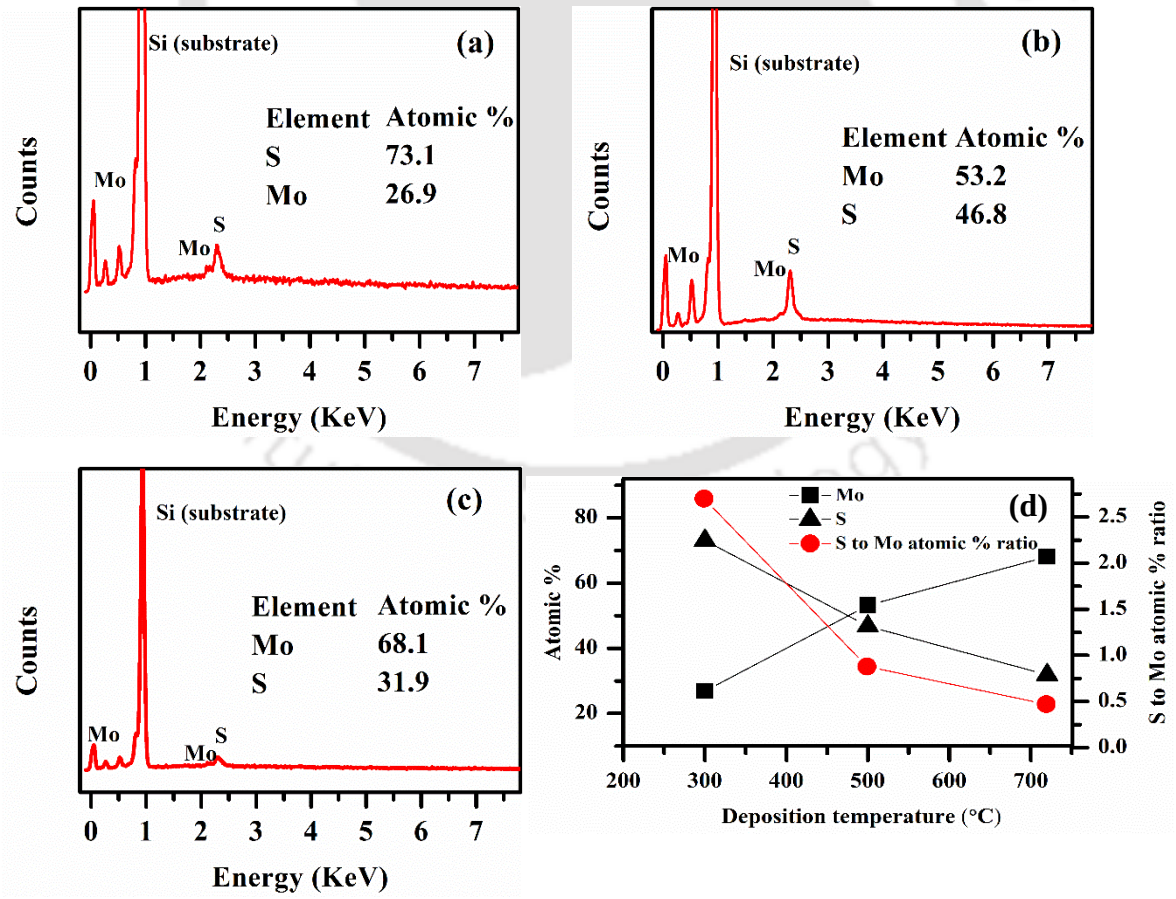

Figure 3.11 EXD spectra of the MoS_2 films deposited at (a) 300, (b) 500 and (c) 720 °C and (d) the elemental atomic % of S and Mo and their ratio in the respective MoS_2 films.

At low temperature sufficient S was present in the film while with an increase in deposition temperature the S to Mo atomic ratio reduced gradually i.e. higher temperature led to S deficient MoS_2 films.

(g) Spectroscopic ellipsometry: SE measurement was performed to investigate the optical properties of the MoS_2 films deposited on SiO_2/Si substrate for 20 sec at different substrate temperatures. The optical properties of films are often extracted from ellipsometry measurements in an indirect way by modeling the optical response of the material. Since the metal and semiconductors interact differently with the light on an interface, it is important to find out the effects of the mixed-phase MoS_2 structure on its optical properties. The optical parameters are also obtained by fitting the SE spectra of the respective MoS_2 films. As discussed in section 2.8, the ellipsometric parameters ψ (amplitude ratio of *p* and *s* component of the reflected light) and Δ (Phase difference of *p* and *s* component) are related to optical and structural properties of the samples and are defined as: $\rho = r_s/r_p = \tan \psi \exp(j\Delta)$, where r_p and r_s represent the complex reflection coefficients of polarised light parallel and perpendicular to the incidence plane, respectively. The ellipsometer spectra were recorded at 70° angle of incidence of the plane polarized light. Spectroscopy ellipsometry analyzer (SEA) software was used to fit the measured spectra with a dispersion model. To fit the recorded spectra a five-layer model consisting of Si/SiO_2/MoS_2/MoS_2 rough surface/ambient air was considered (as shown in fig. 3.12(a)) where SiO_2/Si is the substrate, MoS_2 is the film deposited on the substrate and the fifth layer is the air medium above the film. MoS_2 rough surface layer is excluded for the film deposited at 500 and 600 °C, as these films were very smooth. During simulation, *n-k* file (from SEA database) was used for Si and SiO_2, and ambient air. The thickness of Si and SiO_2 was known (380µm and 300 nm, standard substrate). MoS_2 roughness layer was modeled using Bruggeman effective medium approximation (EMA) formed by a mixture of 50% MoS_2 and 50% voids. To fit the experimental spectra a dispersion model with the contribution of

single Drude and three Lorentz oscillators were used. Lorentz equation for dielectric permittivity is given by

$$\varepsilon_1(E) = \frac{fE_0{}^2(E_0{}^2 - E^2)}{(E_0{}^2 - E^2)^2 + \Gamma^2 E^2} \text{ and } \varepsilon_2(E) = \frac{fE_0{}^2 \Gamma E}{(E_0{}^2 - E^2)^2 + \Gamma^2 E^2} \quad (3.3)$$

where E is the photon energy and f, E_0, Γ are the oscillator strength, oscillator position and damping coefficient of Lorentz oscillator in eV. On the other hand, Drude model is generally used to describe the electrical conductivity of quasi-free electrons in metals and charge carriers in semiconductor materials. The Drude model corresponding to the dielectric function for ellipsometer fitting is usually given by

$$\varepsilon_1(E) = -\frac{(\frac{E_p}{E})^2}{1+(\frac{E_p}{E})^2} \quad \text{and} \quad \varepsilon_2(E) = \frac{E_\Gamma}{E}\frac{(\frac{E_p}{E})^2}{1+(\frac{E_p}{E})^2} \quad (3.4)$$

where E_p and E_Γ are the plasma energy and broadening energy parameters related to the scattering frequency. The electrical conductivity (δ), as well as carrier concentration (N_n) of a film, can be extracted from the Drude parameters E_p and E_Γ as follows: $\delta = \frac{\varepsilon_0 E_p^2}{E_\Gamma \hbar}$ and $N_n = \frac{m_n^* \varepsilon_0 E_p^2}{\hbar^2 e^2}$ where ε_0 is the free space permittivity and m^* is the effective scalar mass of the charge carrier. The root means square error (RMSE) presents the goodness of the fittings. The minimum value of RMSE (i.e. ~ 0) corresponds to a more accurate fitting of the simulated spectra with the experimental one. The experimental and simulated SE spectra (ψ and Δ) of the MoS_2 films along with the bare SiO_2/Si substrate are shown in fig. 3.12(b), (c) and (d). The ψ and Δ spectra of all the films were almost overlapping on the ψ and Δ spectra of bare substrate. The MoS_2 layers were so thin that the ellipsometer spectra were mostly dominated by underlying substrate. At one of the extreme points (2.65 eV) of ψ the peaks of the films were red-shifted by ~ 0.05 to 0.1 eV with an increase in peak intensity of 2-5 deg. The same phenomenon was also observed in the Δ spectra of the films where the peak intensity

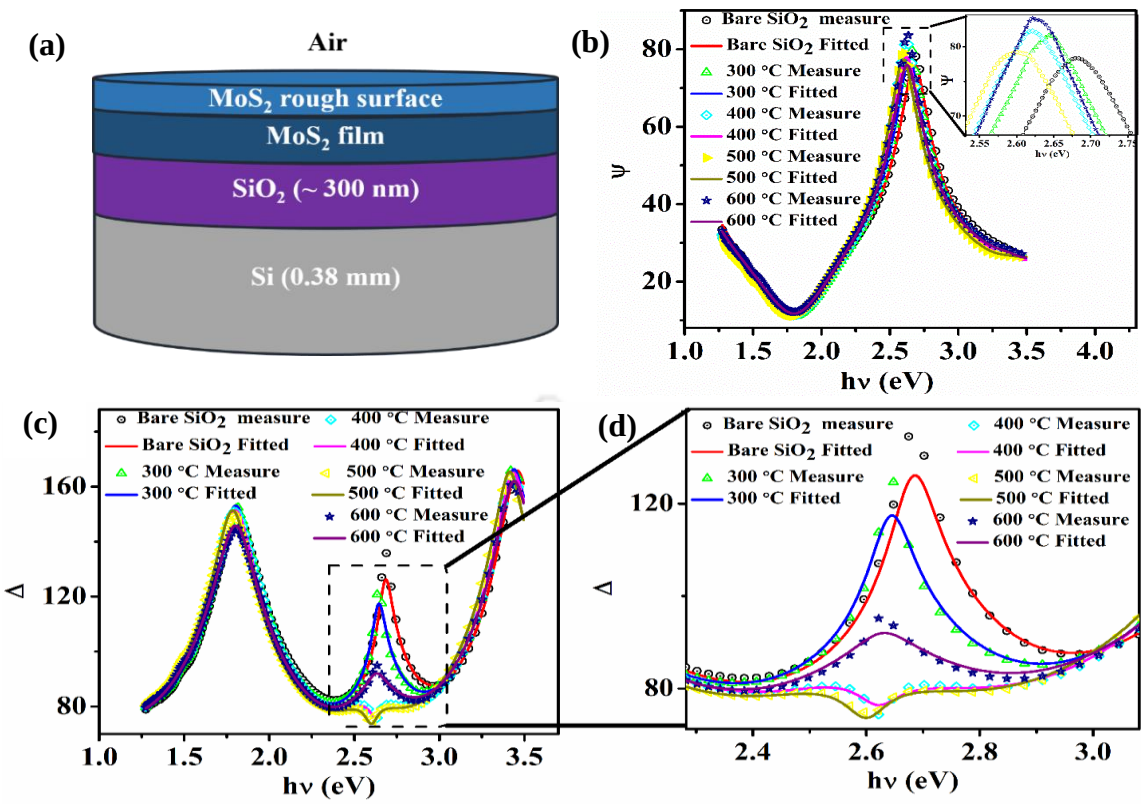

Figure 3.12 (a) Five-layered model considered for the ellipsometer fitting, (b) and (c) SE spectra (ψ and Δ) of the MoS_2 films and bare SiO_2/Si substrate fitted with single Drude and 3 Lorentz oscillator relation and (d) magnification in SE spectra for Δ in the range of around 2.3 - 3.1 eV.

(phase difference) decreased by 10-50 deg along with a red shift of ~0.05-0.1 eV. Film thickness (*d*), surface roughness (*r*), refractive index (*n*), and extinction coefficient (*k*) are the important parameters obtained through the best fitting of experimental *ψ* and *Δ* spectra. The optical parameters and dispersion law parameters obtained from the fitting are listed in table 3.2. The thicknesses of the MoS_2 film deposited at 600, 500, 400 and 300 °C are 0.7, 1.25, 2.11, and 1.21 nm, respectively which were almost the same as estimated from Raman analysis. The surface roughnesses were 1.93 and 2.24 nm for the films deposited at 400 and 300 °C which are similar to the AFM result. The second Lorentz oscillator peak energies were in the range 1.82-1.98 eV which corresponds to *A/B* excitonic transitions (typically 1.8-2.0 eV region) attributed to direct *d-d* transitions between the lowest conduction band and valence

band doublet at the high symmetry *k* point in the Brillouin zone and the 3rd Lorentz oscillator energies 2.79-2.96 eV corresponds to *C/D* excitonic transitions (occur in the range of 2.7-3.1 eV) [132].

Table 3.2 The film thickness, surface roughness and single Drude and three Lorentz oscillator parameters along with electrical conductivity, carrier concentration and RMSE values of the MoS_2 films deposited at various substrate temperatures.

Parameters		**600 °C**	**500 °C**	**400 °C**	**300 °C**
Thickness	d_e	0.70	1.25	2.12	1.12
Roughness	r_e	-	-	1.93	2.42
Drude	E_p	2.22	2.96	1.59	0.72
	E_Γ	0.66	1.06	1.27	0.45
Lorentz 1	f_1	0.26	0.25	0.21	0.21
	E_{01}	0.0005	0.0005	0.0001	0.0001
	Γ_1	0.189	0.13	0.19	0.19
Lorentz 2	f_2	0.06	0.33	0.12	0.06
	E_{02}	1.85	1.95	1.98	1.82
	Γ_2	0.13	0.33	0.30	0.18
Lorentz 3	f_3	0.13	1.28	0.60	0.15
	E_{03}	2.96	2.86	2.93	2.79
	Γ_3	1.89	0.83	0.84	0.54
δ (S/m)		1.01×10^5	1.1×10^5	2.68×10^4	1.56×10^4
N_n (at/cm^3)		8.96×10^{20}	1.58×10^{21}	4.6×10^{20}	9.45×10^{19}
RMSE		0.02	0.02	0.02	0.02

The Drude model used in modeling helps in extracting the film conductivity, carrier concentration of the respective films as shown in table 3.2. MoS_2 film deposited at 500 °C showed maximum conductivity with the presence of very high carrier concentration (electron) while the conductivity, as well as carrier concentration of other films, decreased on both sides of the deposition temperature of 500 °C. Presence of 1T phase with high proportion, S vacancy, overall highly crystalline structure may cause high conductivity of the film deposited at 500 °C. A very low RMSE value of ~ 0.02 suggested a good quality of fitting.

Figure 3.13(a) and (b) shows *n* and *k* spectrum of the MoS_2 films extracted from the optical model resulting best fit of SE spectra. The *n* of the films is maximum at ~1.9 eV. The *k* spectra of all the films shows peaks at ~2.0 eV and ~3.2 eV attributed to *A/B* excitonic transition and *C/D* excitonic transition, respectively. The optical band gap of the respective films is estimated by applying Tauc-plot as shown in fig. 3.14. The absorption coefficient (α) in terms of *k* and λ is expressed as $\alpha=4\pi k/\lambda$. The Tauc-plot is given as $(\alpha h\nu)^{1/m} = \phi(h\nu - E_g)$ where, $h\nu$ is the photon energy, ϕ is a constant called band tailing parameter, *n* is a number that represents the band transition character. The number *m* is ½ for direct band transition and 2 for indirect band transition. The above mentioned Tauc-plot relation is solely developed on

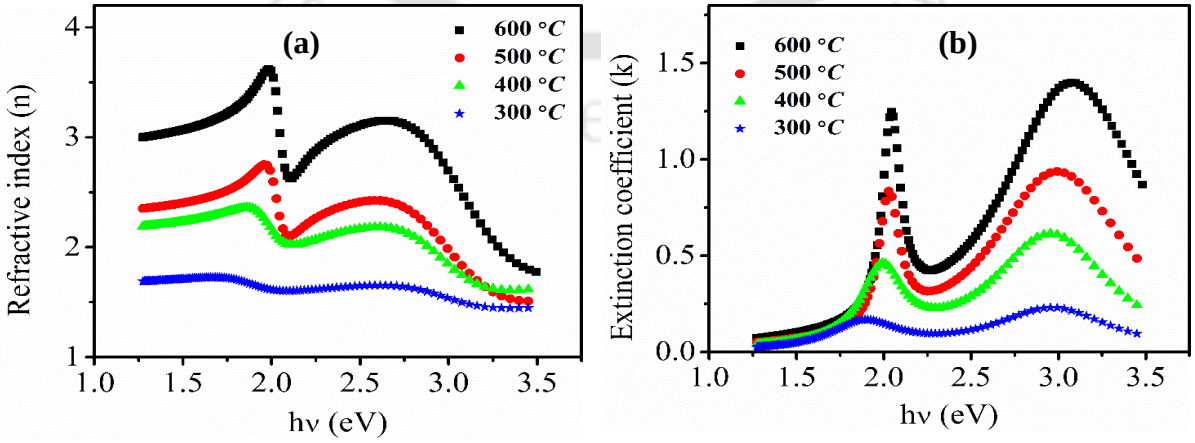

Figure 3.13 The plot of (a) refractive index and (b) extinction coefficient of the MoS_2 films deposited at various substrate temperatures.

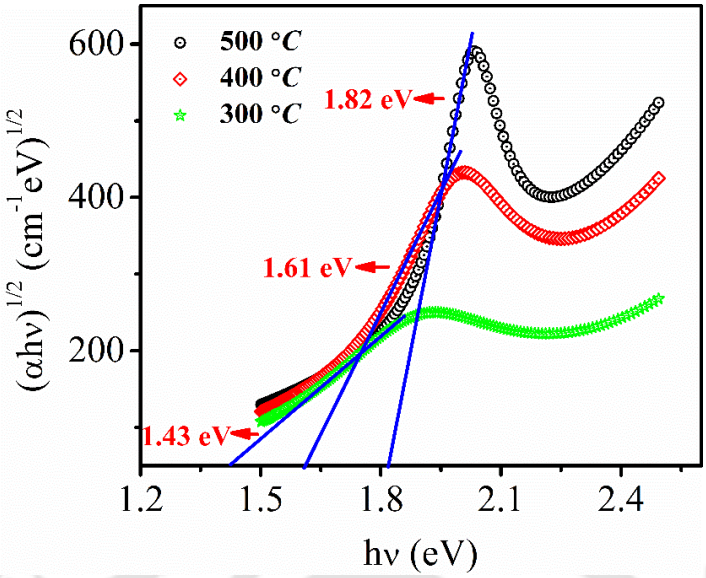

Figure 3.14 Tauc-plot of the MoS_2 films deposited at 300, 400 and 500 °C.

the basis of the density of state (DOS) of bulk (3D) material and is not valid for 2D, 1D or 0D structured material [133]. So the Tauc-plot is not applicable for the MoS_2 monolayer formed at 600 °C and higher temperature while the band gap is estimated for the multi-layered films deposited at 500 °*C* and other films at lower temperatures. It is observed that the band gap of the films reduced from 1.82 to 1.43 eV by lowering the deposition temperature from 500 to 300 °C, following the thickness dependent bang gap modification properties of the MoS_2 layered film.

(h) Diffuse reflectance spectroscopy: As the films are deposited onto an optically opaque substrate, the diffuse reflectance of the films is shown in fig. 3.15(a). The absorption equivalent of the films has been extracted from their diffuse reflectance using the relation: $F(R) = (1-R)^2/2R$, where R is the measured diffuse reflectance. The $F(R)$ spectra of the films are shown in fig. 3.15(b). The observed absorption peaks at ~ 2 and 3.3 eV corresponds to the *A/B* and *C/D* excitonic transitions in the layered MoS_2 films which were discussed earlier.

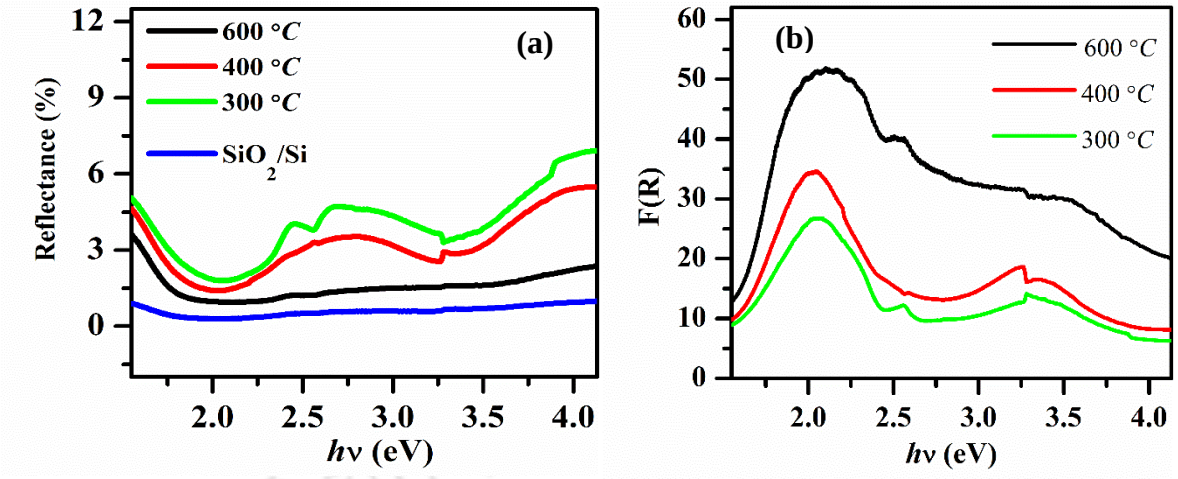

Figure 3.15 (a) Diffuse reflection spectra and (b) Kubelka-Munk absorption spectra of the MoS_2 films.

Hence with the reported results, it was found that deposition temperature significantly effects the film thickness, surface morphology, crystallinity as well as MoS_2 stoichiometry. All the MoS_2 films, deposited at 300 to 720 °C showed a 1T-2H mixed-phase MoS_2 film formation with different proportionality. Most reports suggested 1T phase as a metastable phase and a 1T to 2H phase transition occur by annealing above 300 °C. But in the present case, 1T phase MoS_2 coexisted with 2H-MoS_2 even at the 720 °C deposition temperature. At the low deposition temperature, the impinging MoS_2 plasma onto SiO_2/Si substrate did not get enough energy to redistribute to the most stable 2H-MoS_2 phase which led to a mixed-phase MoS_2 film. On the other hand, even though films at 500 °C and other higher temperature got enough energy to rearrange themselves to the 2H-MoS_2, but 1T phase MoS_2 also existed in those films. The result can be explained as follows. During the deposition, the higher substrate temperature causes re-evaporation of the relatively light S material which leads to S deficient MoS_2 films as confirmed by EDX analysis. The S deficiency causes a defect in the MoS_2 structure and generates excess negative charge in the films. The semimetal like large negative charge was estimated from the ellipsometric analysis. Defect and excess negative charge provided favorable conditions to form the 1T phase even at the high deposition temperature.

3.4.2 MoS_2 thin films deposited on various substrates

Along with the SiO_2/Si substrate, MoS_2 films were deposited on Corning glass under the same deposition temperatures. The formation of deposition temperature-independent mixed-phase 1T-2H MoS_2 on the corning glass is also confirmed by Raman spectra as shown in fig. 3.16(a). Raman analysis (fig. 3.6(d)) showed that 1T phase MoS_2 deposited on SiO_2/Si substrate mostly dominates at 400 °C.

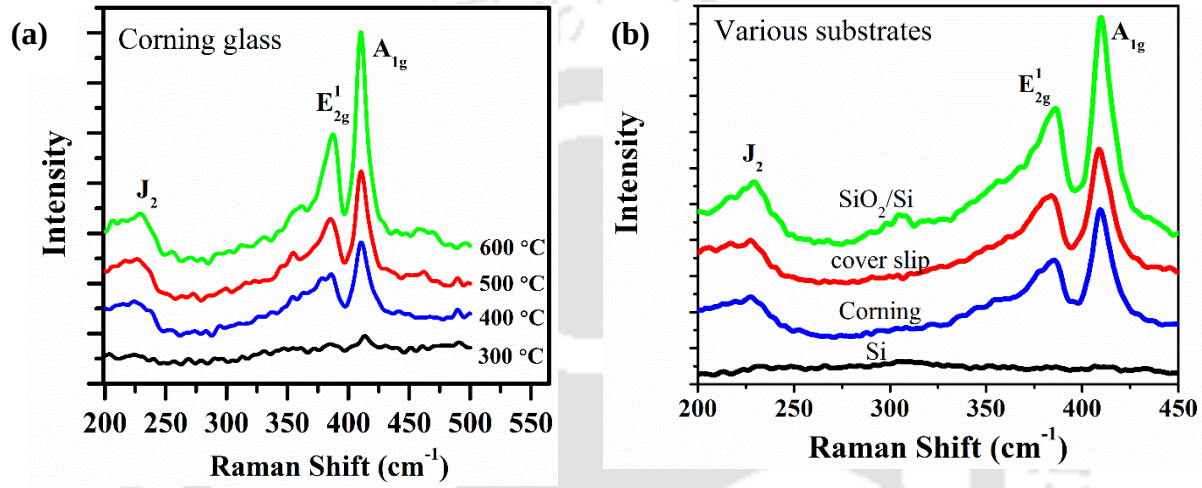

Figure 3.16 (a) Raman spectra of the MoS_2 films on Corning glass substrate deposited at different temperatures and (b) Raman spectra of the MoS_2 films deposited on various substrates for 20 sec.

To understand the effect of the substrate, MoS_2 films were deposited on various substrates like SiO_2/Si, cover slips, corning glass and Si (100) for 20 sec at 400 °C. Figure 3.16(b) shows the Raman spectra of MoS_2 films on various substrates. The 1T phase is present in all the films except the one deposited on Si (100) where the sign of 2H phase is missing.

3.4.3 MoS_2 thin films deposited at various deposition times

Figure 3.17(a) shows the Raman spectra of MoS_2 films on SiO_2/Si substrate exhibiting the evolution of both 1T and 2H phase with deposition time varying from 1 min to 10 min. It was observed that with the increase in deposition time from 1 min, the 1T phase started to diminish and at 10 min the phase almost vanished. A similar phenomenon was observed by

Loh et al. in case of 1T-WS_2 films deposited via PLD technique where the imprinting energetic ions in prolonged deposition time disintegrated the metastable 1T-WS_2 into metallic tungsten [96]. Figure 3.17(b) shows the peak position difference between the two Raman modes A_{1g} and E^1_{2g} and the % of 2H-MoS_2 present in the films, deposited at 1, 2, 5 and 10 min.

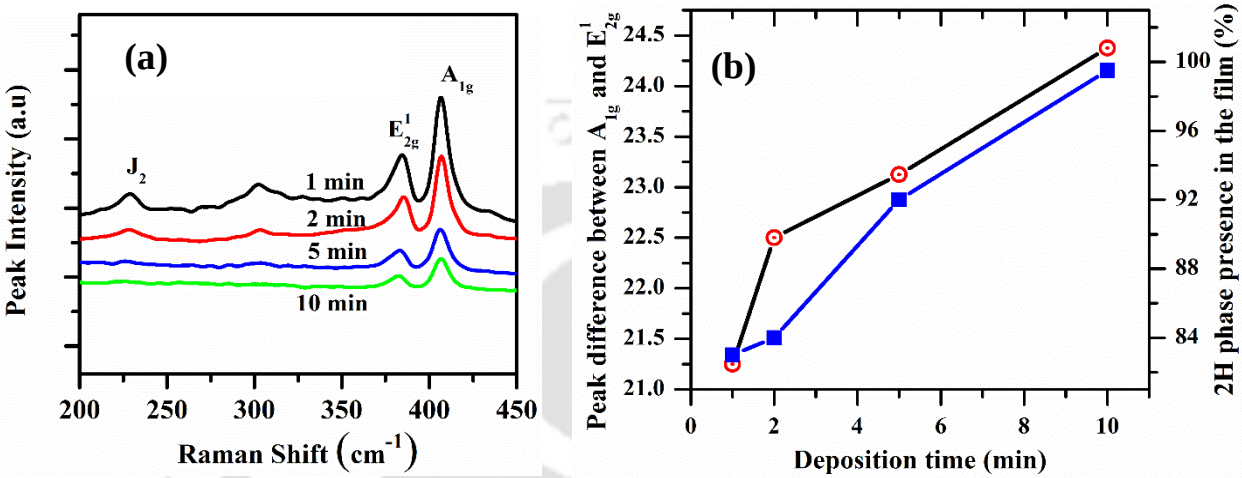

3.17 (a) Raman spectra of MoS_2 films deposited at different deposition time and (b) Peak difference of A_{1g} and E^1_{2g} and % of 2H phase present in the MoS_2 films deposited at various deposition time.

Further, with the increase in deposition time, the peak position difference increased from 21.25 to 24.38 cm^{-1} corresponding to an increase in film thickness. Hence with the increase in deposition time the 2H-MoS_2 phase also increased from ~83% for 1 min deposited film to ~99.5% for 10 min deposited film. Most of the reported 1T phase MoS_2 were synthesized in the form of nanosheet via intercalation exfoliation, chemical exfoliation, while 1T phase generated inside a 2H- MoS_2 nanosheets via electron beam irradiation, plasmonic hot electron injection treatment [112,134-136].

To the best of our knowledge, two groups reported on spin-coated and dip-coated 1T-2H mixed-phase MoS_2 thin films of very high thicknesses (550 nm, and 150 nm) [137,138]. In the present case, the 1T-2H mixed-phase MoS_2 layers were deposited in the form of thin film of large dimension (~1×1 cm^2) in a bottom-up route. In thin films, the MoS_2 layers strongly adhere

to the underlying substrate which provides good stability and durability in terms of device application. A lot of efforts were made to create S vacant MoS_2 nanosheets by α particle irradiation, [139] argon plasma treatment, [140] electrochemical desulfurization [141] like post synthesis processes, while S deficient MoS_2 films were obtained in a single step growth process at high deposition temperatures. S vacancy generated highly crystalline 1T MoS_2 films at high deposition temperatures resulted in more active edge sides along with an active basal plan, which may act as an efficient photocatalyst.

3.5 Layered WS_2 thin films deposition by PLD

3.5.1 Determination of layer number of WS_2 films

WS_2 films showed similar Raman spectroscopic characteristics as MoS_2 films. Like MoS_2, in WS_2 also the two Raman active modes E^1_{2g} and A_{1g} showed layer sensitive peak position. The blue shift of A_{1g} and red shift of E^1_{2g} with an increase in layers numbers from monolayer to higher order has been reported for WS_2 films [117]. This resulted in an increase in peak position difference (ΔF) between A_{1g} and E^1_{2g} from 62.5 cm^{-1} for monolayer to 68.5 cm^{-1} for bulk WS_2. Figure 3.18 shows the Raman spectra of the WS_2 films deposited at the laser

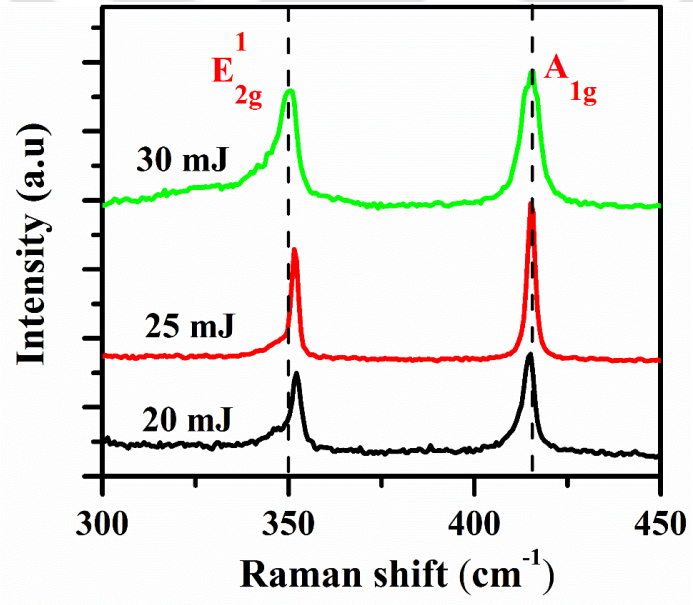

Figure 3.18 Raman spectra of layered WS_2 films.

energy of 20, 25 and 30 mJ, respectively. The peak positions corresponding to A_{1g} were observed at 414.5, 417.8, and 419 cm^{-1} while that corresponding E^1_{2g} were seen at 356, 353 and 349 cm^{-1} for the films deposited at the laser energy of 20, 25 and 30 mJ, respectively. The peak difference between the two Raman modes, ΔF, in the respective films was found to be 63, 64.8, and 65.5 cm^{-1}, corresponding to monolayer, bilayer, and multilayer WS_2 films which are in accordance with the literature [142].

The film thicknesses were also estimated using AFM images. Fig. 3.19(a), (b) and (c) represent typical height of WS_2 films with respect to bare substrate at the laser energy of 20, 25 and 30 mJ. The height profile extracted from AFM images show that the film thicknesses were 0.69, 1.4 and 4.1 nm which were equivalent to monolayer, bilayer and multilayer WS_2 films.

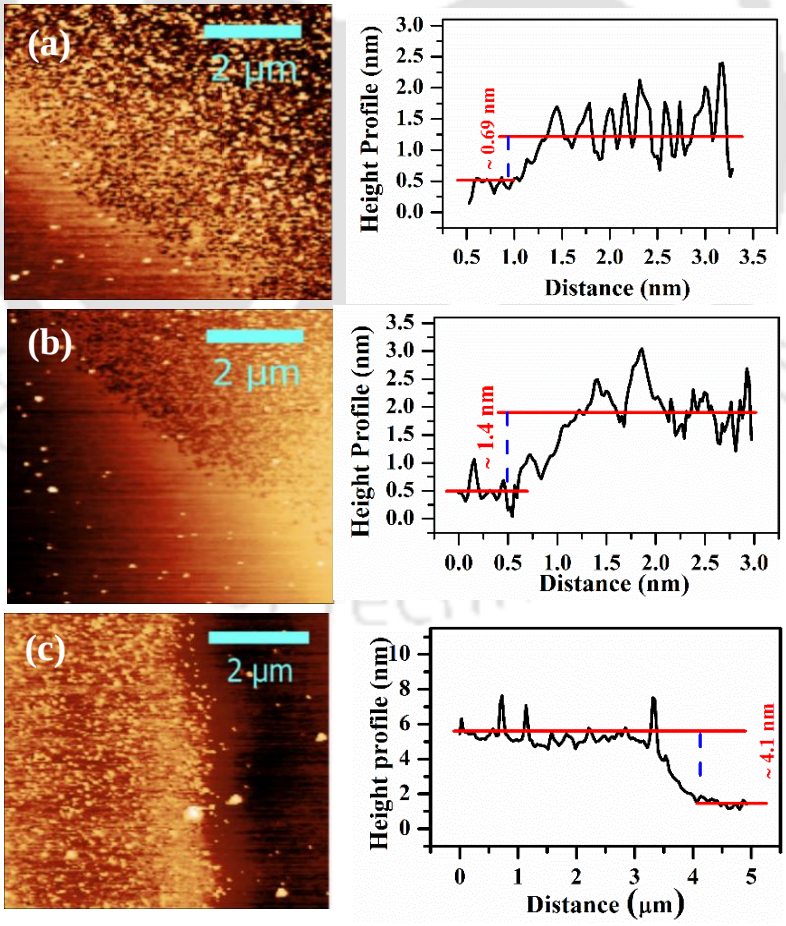

Figure 3.19 AFM height profile of (a) monolayer, (b) bilayer and (c) multilayer WS_2 films deposited on SiO_2/Si substrate.

3.5.2 Crystalline structure of the WS_2 thin films

Figure 3.20 shows the XRD patterns of WS_2 pellet and layered WS_2 films. All the films showed *c*-axis epitaxial growth with the presence of (002) peak. XRD pattern of WS_2 pellet showed characteristic peaks of WS_2 (002), (004), (100), (103), (006) and (105) crystalline planes. The pellet exhibited polycrystalline nature. XRD pattern of monolayer and bilayer films also showed *c*-axis epitaxial growth with the presence of (002) peak. The crystallite size of the films was estimated with Debye-Sherrer formula (equation 3.1). Being mostly intense, (002) peak was used to determine the average crystallite size using Debye-Sherrer formula. The estimated crystalline size of monolayer, bilayer, multilayer WS_2 films and WS_2 pellet was 44, 37.8, 36 and 66 nm, respectively. A similar result was also observed in the case of MoS_2 layered films where MoS_2 Monolayer showed large crystalline size compared to multilayered films.

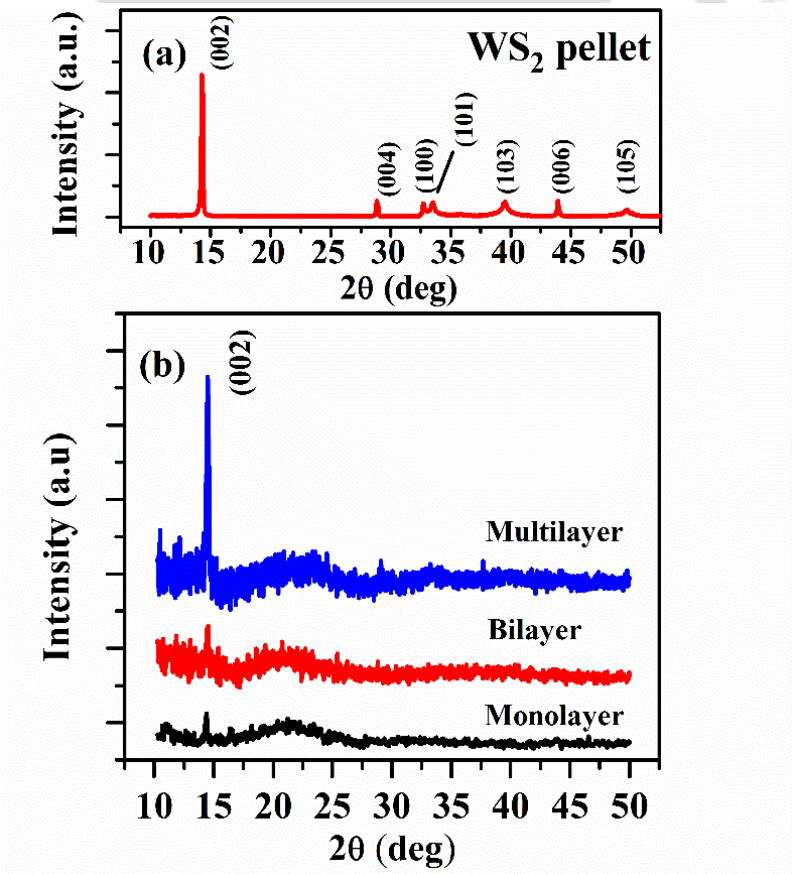

Figure 3.20 XRD patterns of (a) WS_2 pellet and (b) layered WS_2 films.

3.5.3 Optical characterizations

The PL spectra of the monolayer, bilayer and multilayer WS_2 films are shown in fig. 3.21 (a). Significant PL emission peaks were detected at 2.14, 1.88 and 1.79 eV corresponding to the monolayer, bilayer and multilayer WS_2 films. With an increase in the number of layers from monolayer to trilayer, the PL peak intensity decreased and peak energy shifted towards lower energy [9]. The direct-indirect band gap transition of WS_2 films with an increase in film thickness caused a visible intensity reduction in the PL emission [6,125]. The typical energy level diagrams of PL emission in the monolayer WS_2 film is shown in fig. 3.21 (b).

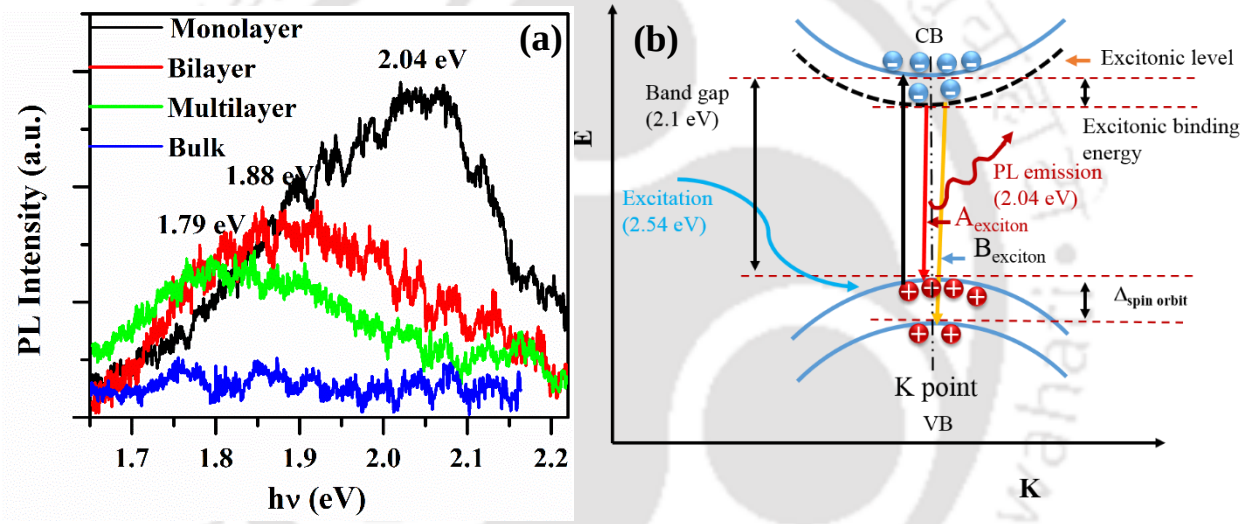

Figure 3.21(a) PL spectra of WS_2 films deposited with laser energy of 20, 25 and 30 mJ and (b) The schematic of energy level diagram of PL emission of monolayer WS_2 film.

The band structure of monolayer WS_2 is similar to monolayer MoS_2 as discussed earlier in section 3.3.3. In monolayer WS_2 the direct band transition occurs from conduction band minimum to valence band maximum of ~2.1 eV at the *K* point of the Brillouin zone and the PL emission of 2.04 eV corresponding to the A excitonic transition.

3.6 Conclusion

Monolayer, bilayer to multilayered MoS_2 thin films were deposited using PLD technique. The layered numbers of the deposited films were controlled by applying different

number of laser pulses. Number of layers of the MoS_2 films were determined by measuring layer sensitive E^1_{2g} and A_{1g} Raman modes peak position difference and height profile of AFM images of the respective films. XRD patterns of the films, showed characteristic peak corresponding (002) plane, thus indicating highly crystalline *c*-axis oriented epitaxial thin film growth. The lattice spacing of the *as*-grown film measured from HRTEM image was 0.27 nm (corresponding to 002 plane) which further confirmed the XRD result. Photoluminescence emission peaks in monolayer, bilayer and multilayer MoS_2 films were observed at 1.81, 1.78 and 1.72 eV, respectively. The red shift of the luminescence peak position with increase in layer numbers clearly indicated the decrease in band gap energy of MoS_2 and WS_2 films with increase in film thickness. Along with semiconductor phase 2H structure, a metallic phase 1T was detected in the layered MoS_2 films. 1T/2H mixed phase mono and a few layered MoS_2 thin films were realized by PLD for a very short span of time of 20 sec. The 1T/2H phase ratio in monolayer to a few-layered MoS_2 films was modulated by altering the substrate temperatures and deposition time. Irrespective of deposition temperatures all the films showed a mixed phase structure while the 2H to 1T phase ratio increased from 66 to 84% with an increase in deposition temperature from 400 to 720 °C. The presence of 1T-2H mixed phase MoS_2 layers was confirmed and their structural and optical properties were analyzed in nano (TEM), micro (Raman, AFM) and macro (ellipsometer) scale. The ellipsometric analysis confirmed the *A*/*B* and *C*/*D* excitonic absorption peaks corresponding to 2H phase while the presence of 1T phase caused excess semimetal like charge density of the order of ~10^{20} cm^{-3}. At lower deposition temperatures, lack of sufficient energy to redistribute the impingement plasma particle to the most stable 2H-MoS_2 phase led to a mixed phase of MoS_2 film while S deficiency induced defects and excess negative charges attributed to form 1T phase at the high deposition temperatures. Along with MoS_2 layered films, WS_2 thin films were also deposited using PLD technique. The layered number of the deposited films were controlled by applying

different laser energies. Like the MoS_2 films, the number of layers of the WS_2 films were determined by measuring layer sensitive E_{2g}^1 and A_{1g} Raman modes peak position difference and height profile of AFM images of the respective films. XRD patterns of the films showed (002) plane oriented crystalline structure. The photoluminescence peak in monolayer, bilayer and multilayer WS_2 films were observed at 2.14, 1.88 and 1.79 eV, respectively. From the PL spectra it is clearly observed that the band gap energy of WS_2 films decreases with an increase in film thickness.

Chapter 4

Surface evolution of a few-layered to bulk-like MoS_2 and WS_2 thin films during growth under pulsed laser deposition

4.1 Introduction

Growth dynamics of thin films expressed by scaling theory is a useful tool to quantify statistical properties of surface morphology of the thin films. The morphology and nanostructure of thin films strongly depend on the deposition method and growth conditions (i.e. deposition time and temperature, growth rate, etc.) [143,144]. Surface morphology of thin films can control many physical and chemical properties (such as optical, catalytic, mechanical, electronic, etc.) which can strongly affect the device performance of the films. Therefore, understanding the growth dynamics of the deposited thin films is very important.

In chapter 3, monolayer to multilayered films were deposited at various ablation times. In the present chapter, a detailed study on the evolution of surface morphology of a few-layered to multilayered to further bulk-like MoS_2 films was carried out to understand the growth dynamics and scaling behavior involved in MoS_2 thin film growth under PLD. A comparative study on the growth evolution of a few-layered to bulk-like WS_2 films on two different substrates, in the light of scaling theory and stochastic growth equation was also performed. The height-height correlation function (HHCF) was fitted with an appropriate theoretical model to extract the interface width (w), lateral correlation length (ξ) as they evolve with deposition time. The film properties were quantified statistically in terms of short-range (local) as well as long-range (global) roughness exponents (α_{loc} and α), growth exponent (β), dynamic scaling exponent (1/z), etc. to determine the type of scaling and growth mechanism involved. This understanding can enable one to attain controlled growth of a film required in different

applications. Spectroscopic ellipsometry (SE) studies enabled us to estimate the refractive index (*n*) and extinction coefficient (*k*) spectra for various film thicknesses. Their variation with increasing film thickness was correlated with RMS roughness (interface width *w*) and island size (correlation length ξ) variation which unveiled the important role played by surface roughness and film density. Moreover, the SE studies were also used to support the anomalous scaling behavior of MoS_2 film growth as concluded from AFM analysis.

4.2 Experiment details

MoS_2 thin films were deposited onto corning glass substrate via PLD technique at various deposition times of 20 sec, 1, 2, 5, 10 and 15 min duration at a substrate temperature of 600 ºC. WS_2 thin films were deposited onto corning glass and oxidized Si (SiO_2/Si) substrate via PLD. The films were deposited at various deposition times of 30 sec, 2, 5, 10, 15 and 20 min duration at a substrate temperature of 400 ºC. The surface morphology of all the films was recorded via AFM to study the dynamic scaling and growth mechanism of MoS_2 and WS_2 films deposited via PLD technique**.** Further, layered structure, crystallinity, optical behavior of the thin films were characterized by Raman spectroscopy, X-ray diffractometer, and spectroscopic ellipsometer**.**

4.3 Growth dynamics study of MoS_2 thin films

4.3.1 Structural characterization of MoS_2 films

Figure 4.1 shows Raman spectra of MoS_2 films at the deposition time of 20 sec, 1, 2, 5 min and MoS_2 pellet in backscattering configuration. Each spectrum shows twin peaks corresponding to A_{1g} and E^1_{2g} Raman modes of MoS_2. The E^1_{2g} and A_{1g} Raman modes show layer sensitive peak positions. The peak position difference of A_{1g} and E^1_{2g} of MoS_2 films increased with an increase in layer numbers from monolayer to higher order [117]. The Raman peak position difference of the deposited films are shown in the inset of fig. 4.1. The peak positions corresponding to A_{1g} mode were observed at 407.5, 407.5, 405.6 and 406.2 cm^{-1}

while that corresponding to E^1_{2g} at around 385.6, 385, 382.5 and 380 cm^{-1} for the films deposited for the time duration of 20 sec, 1, 2 and 5 minutes, respectively.

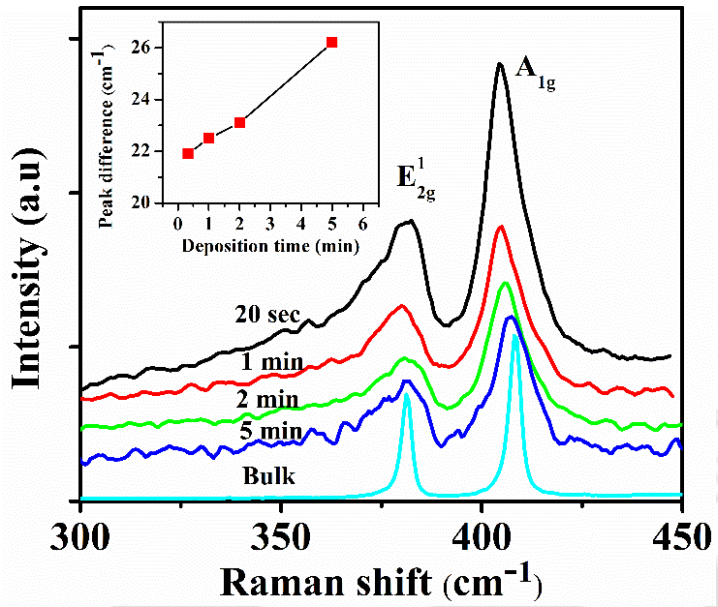

Figure 4.1 Raman spectra of the MoS_2 films as a function of deposition time (t).

The peak differences between the two Raman modes, ΔF, in the respective films were found to be 21.9, 22.5, 23.1 and 26.2 cm^{-1}, corresponding to bilayer, trilayer, multilayer and bulk-like MoS_2 films [19]. The Raman analysis of the films confirmed an increase in film thickness with the deposition time. Using surface profilometer the thicknesses of the films deposited for 1, 2, 5, 10 and 15 min deposition time were estimated to be 2.5, 6.4, 19.9, 39.6 and 81.2 nm, respectively while thickness of film deposited at 20 sec could not be measured accurately due to much lower thickness (< 2 nm). Figure 4.2 shows XRD pattern of the MoS_2 thin films. The XRD spectra of MoS_2 films show peaks at 2θ = 13.71° and 40.62° which corresponds to MoS_2 (002) and MoS_2 (103) planes, respectively, with former being more intense [20]. The peak intensity of both peaks increased while the corresponding FWHM decreased with increasing deposition time as the MoS_2 film thickness increased showing increase in crystallinity.

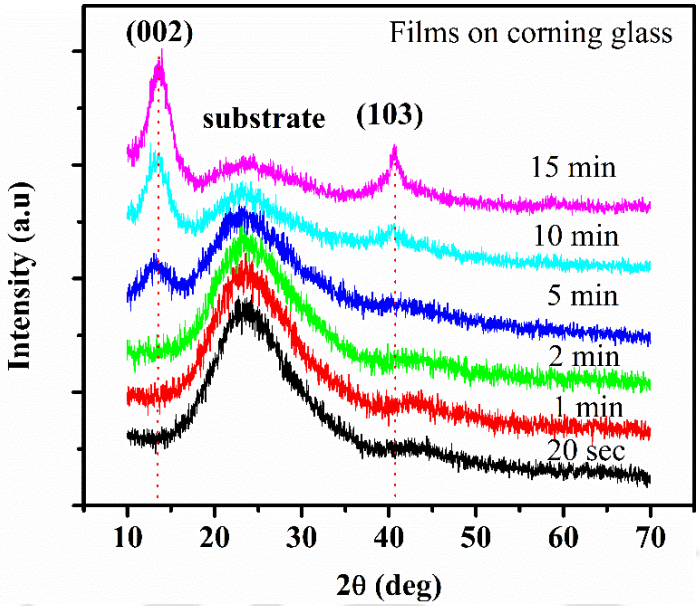

Figure 4.2 XRD spectra of PLD MoS_2 thin films deposited on Corning glass substrate for different deposition times, t (20 sec –15 min).

4.3.2 Scaling studies of MoS_2 film growth using AFM image analysis

The post growth surface morphology of the films was characterized systematically using AFM to study the surface microstructure and dynamics of the growth. Figure 4.3(a)–(f) shows the AFM images of MoS_2 films grown onto the corning glass surfaces at 600 °C substrate temperature with 20 sec, 1, 2, 5, 10 and 15 min deposition time, respectively. The AFM micrograph confirmed that the grains were uniformly distributed within the film scanning area (2μm × 2μm). The scaling exponents (α_{loc}, *ß, 1/z*) were estimated from the height-height correlation function (HHCF), *H(r,t)* by analyzing the surface morphology recorded using AFM to understand the growth processes and the dynamic scaling behavior involved during PLD of MoS_2 films. *H(r,t)* is defined as statistical average of the mean square of height difference between two positions (*x, y*) and (*x′, y′*) on the surface separated by a distance *r* ($=\sqrt{(x-x')^2+(y-y')^2}$) along horizontal direction as $H(r,t) = \langle|h(r+r',t) - h(r',t)|^2\rangle$, where $h(r+r',t)$ and $h(r',t)$ are the heights of the surface at (*x, y*) and (*x′, y′*) and each pair of points are obtained from AFM image.

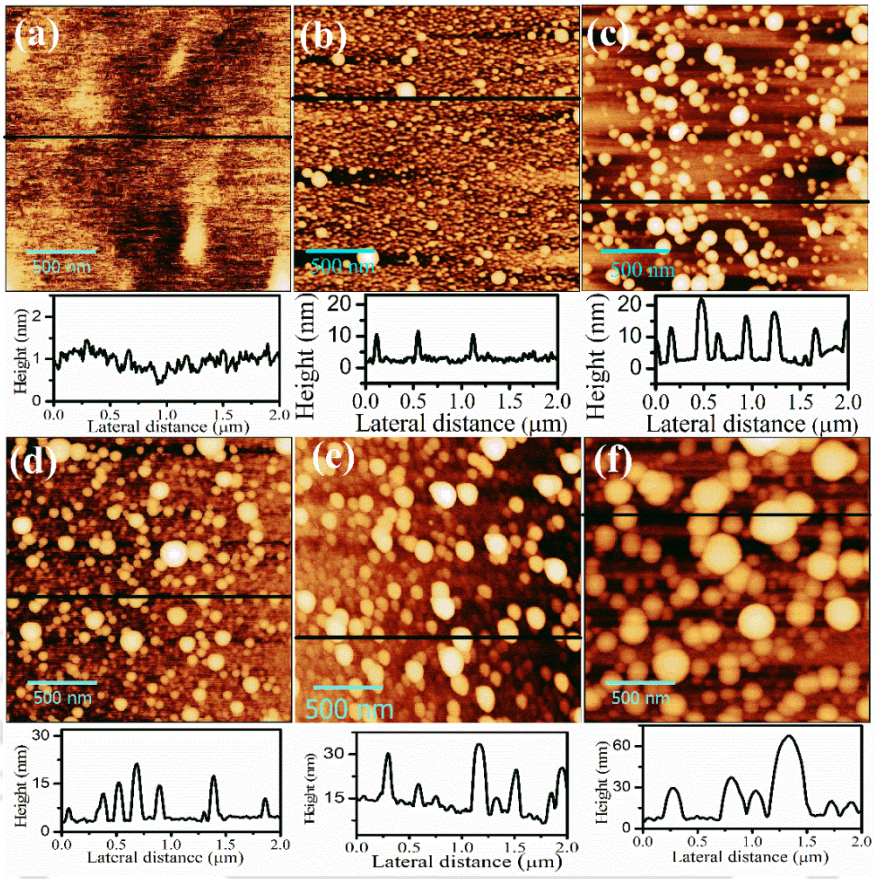

Figure 4.3 AFM images of top surface of PLD MoS_2 films, showing the surface morphology at different deposition times (a) 20 sec, (b) 1, (c) 2, (d) 5, (e) 10 and (f) 15 min. Each image consists of 2×2 μm scanned area and scale bar is 500 nm. The height profile of each image is shown at the bottom of the respective images.

HHCF can be evaluated from AFM images by spatial averaging over one or several regions, which should be much larger than r to avoid edge effects. HHCF shows two distinct behaviors based on the relative magnitudes of r and the lateral correlation length ξ; (i) for $r << \xi$, $H(r,t) \sim [m(t)r]^{2\alpha}$; where $m(t)$ is the local slope and α_{loc} ($0 \leq \alpha_{loc} \leq 1$) is the local roughness exponent, which describes short-range roughness of a self-affine surface, and (ii) for $r >> \xi$, $H(r,t) \sim 2w^2$, where $w = \sqrt{\langle [h(r,t)]^2 \rangle}$ is the RMS roughness (interface width). w evolves following a simple dynamic scaling known as Family-Vicsek relation, expressed as

$$w = t^{\beta} f\left(\frac{r}{t^{\frac{\beta}{\alpha_{loc}}}}\right) \tag{4.1}$$

where

$$f\left(\frac{r}{t^{\frac{\beta}{\alpha_{loc}}}}\right) \sim \begin{cases} contant & when, r \gg t^{\frac{\beta}{\alpha_{loc}}} \\ \left(\frac{r}{t^{\frac{\beta}{\alpha_{loc}}}}\right)^{\alpha_{loc}} & r \ll t^{\frac{\beta}{\alpha_{loc}}} \end{cases} \quad (4.2)$$

and $r \leq L$ (L is system size) while α_{loc} and β are the roughness and growth exponents, respectively [145,146]. The above relation suggests that for small r (i.e. $r \ll t^{\beta/\alpha_{loc}}$), w is independent of deposition time t and scales as $r^{\alpha_{loc}}$, but for large r, β *is* independent of r and follow the power laws as $w \sim t^{\beta}$. The crossover between these two behaviors occurs at $r = \xi$, the lateral correlation length within which surface heights are significantly correlated. For dynamic scaling, the parameters w and ξ are dependent on the deposition time, t, and follow the power laws as $w \sim t^{\beta}$ and $\xi \sim t^{1/z}$ [146]. The set of exponents α_{loc}, β and $1/z$, corresponds to a specific universality class and is suggestive of the underlying mechanism that governs the evolution of surface. The HHCF can be defined by exponential correlation model, which satisfies the requirement for self-affine surface and manifests anisotropic scale invariance, given by [146],

$$H(r) = 2w^2\left[1 - exp\left[-\left(\frac{r}{\xi}\right)^{2\alpha}\right]\right] \quad (4.3)$$

From fig. 4.4 (a), it is observed that HHCF, $H(r, t)$ increased linearly with r at small r and saturated at large r, with the asymptotic behavior predicted by equation (4.3) [146]. It is clear from fig. 4.4(a) that $H(r, t)$ shifted upward as the film thickness increased with increasing growth time, which confirmed that the RMS roughness increased with the film growth, indicating roughening in the growth process. The HHCF curves were fitted using equation (4.3) to estimate $w(t)$, $\xi(t)$, and α_{loc}. The variation of these parameters with deposition time were studied to understand the growth dynamics. Figure 4.4(b), 4.4(c) and 4.4(d) show Log−Log variations of w, ξ and α_{loc} versus time (t), respectively. Figure 4.4(b) shows the increasing nature of w from 0.27 to 18.6 nm as the film grows with t from 20 sec to 15 min and it clearly indicates the film roughening during the growth.

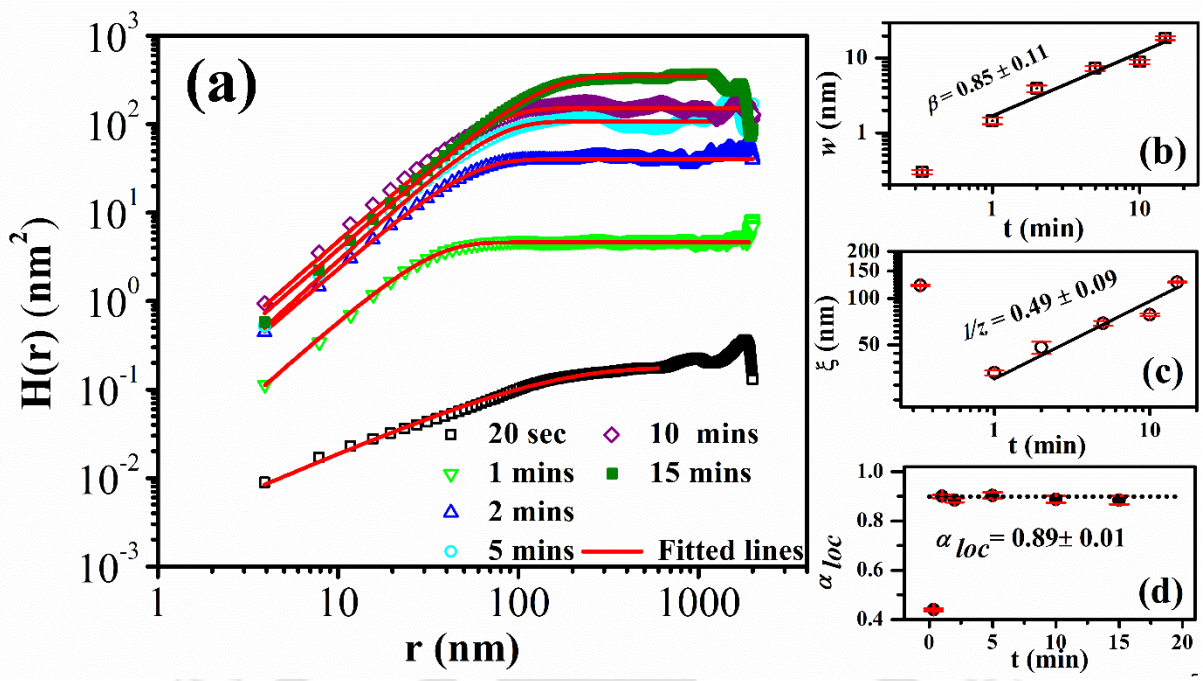

Figure 4.4 (a) Log-Log plot of HHCF, H(r) as a function of distance r with best fitted theoretical curve for MoS_2 thin films on Corning glass substrate at different deposition times (20 sec-15 min). The symbols are experimental data and the red solid lines are fitted with equation (4.3). Plot of (b) surface roughness w, (c) correlation length ξ, and (d) roughness exponent α_{loc} as a function of deposition time, t.

Figure 4.4(c) shows ξ versus t plot. Initially, at 20 sec the value of ξ was 120.3 nm beyond which the value of ξ dropped to 33.2 nm at 1 min deposition time. However, with increasing t from 1 to 15 min an increasing nature of ξ was observed, as shown in Fig. 4.4(c). This indicates the lateral growth of the islands with $\xi \sim t^{0.49\pm0.09}$. This confirmed that as the deposition time increased, the island growth took place both vertically as well as laterally and the overall film became rough. The lateral growth could be attributed to the increased nucleation of more incoming flux and the increase in crystallite size with increasing deposition time. The unusual large value of ξ at early stage of film growth at 20 sec deposition time is due to layered (bilayer) MoS_2 film growth supported by Raman results (fig. 4.1). At this nucleation and growth stage only lateral growth took place (following Frank-Van Der Merwe model) while with an increase in deposition time the vertical growth of the MoS_2 film dominated over the lateral growth (following Sranski-Krastanov model) and the RMS roughness increased

drastically as shown in Fig. 4.4(b) [129]. The parameters w and ξ showed power law dependency as $w \sim t^{\beta}$ and $\xi \sim t^{1/z}$ with $\beta = 0.85 \pm 0.11$ and $1/z = 0.49 \pm 0.09$, respectively. β is called growth exponent signifying the pace of surface roughening with $\beta > 0.5$ represents rapid roughening in thin films due to different non local effects like shadowing, high stickiness of substrate, bulk diffusion of incoming particles, etc. $1/z$ is called dynamics scaling exponent which corresponds to rate of lateral growth of correlated structure (islands). The value of α_{loc} for the film deposited for 20 sec was 0.41 and beyond that, it raised sharply and remained almost similar for all deposition time at around ~ 0.89 ± 0.01. α_{loc} lies between 0 to 1, where, a smaller value of α_{loc} corresponds to the more locally rough surface while the larger α_{loc} of the films corresponds to locally smooth surface.

For dynamic scaling to prevail, $\alpha_{loc} = \beta z$ but in our case $\alpha_{loc} \neq \beta z$, hence the dynamic scaling failed which implies that the scaling did not follow Family-Vicsek relation. In such a case, the height profile may follow another scaling called anomalous scaling where the global and local interface widths scale differently and the global (α, β) and local (α_{loc}, β_{loc}) exponents are also different from each other. Such behavior has been observed where the conventional scaling laws can be modified by introducing new behavior in the interface width, w, which is represented by the anomalous scaling *ansatz*:

$$w(r,t) = \begin{cases} t^{\beta^*} \; r^{\alpha_{loc}}, & if \; r \ll \xi \ll L \\ t^{\beta}, & if \; r \gg \xi \end{cases}, \qquad (4.4)$$

where α_{loc} is the local roughness exponent and β^* is the anomalous growth exponent indicating the time dependence of the w at length scales smaller than ξ and is given by $\beta^* = \beta - \beta_{loc} = (\alpha - \alpha_{loc})/z = \beta - \alpha_{loc}/z$ [145,147-150]. For such a case, there exists a global roughness exponent α ($\sim \beta z$) different from local roughness exponent α_{loc}. Now, for the case of Family-Vicsek relation, $\beta^* = 0$, $\alpha = \alpha_{loc}$ and equation (4.4) gives back $w(r,t)$ for dynamic scaling. The non-zero value of β^* (~ 0.41 ± 0.02) obtained from parameters estimated from HHCF suggests that the growth

process follows anomalous scaling behavior which can be further categorized into super-rough, intrinsic anomalous or new class scaling as will be discussed later. In order to identify the growth mode, local slope $m(t)$ was plotted as a function of deposition time, as shown in Fig. 4.5. For exponential model expressing self-affine surface represented by equation (4.3) , $m = \frac{(w\sqrt{2})^{1/\alpha_{loc}}}{\xi}$ [146].

If $m(t)$ is independent of deposition time, it is called stationary type of growth. In stationary growth, for $r < \xi$ the HHCF will merge for different t values. However, for the non-stationary case, $H(r)$ will shift upward as the local slope, $m(t)$, will change with the duration of deposition [21]. In the present case, the growth was obviously non-stationary as $m(t)$ was not constant. It was observed that the local slope, $m(t)$ increased with time and varied as, $m \sim t^{0.41\pm0.11}$ as depicted in Fig. 4.5. Such a behavior where local slope m evolves with a power law in time, $m(t) \sim t^{\beta^*}$ was observed for anomalous scaling [146,147]. From this observation β^* is found to be ~ 0.41 ± 0.11 which is close to the value obtained from growth exponents. The combination of growth exponents α, $ß$ and $1/z$ is $\alpha = ßz$, then under anomalous scaling also $w \sim t^{ß} = t^{\alpha/z}$. As $\xi \sim t^{1/z}$, one can easily observe that $w \sim \xi^{\alpha}$ and the value of α can be found using the slope of log w versus log ξ as shown in Fig. 4.6. From the plot, the value α = 1.72 ± 0.14 was estimated, which is close to that obtained from $\alpha = ßz$ ~1.70 ± 0.13.

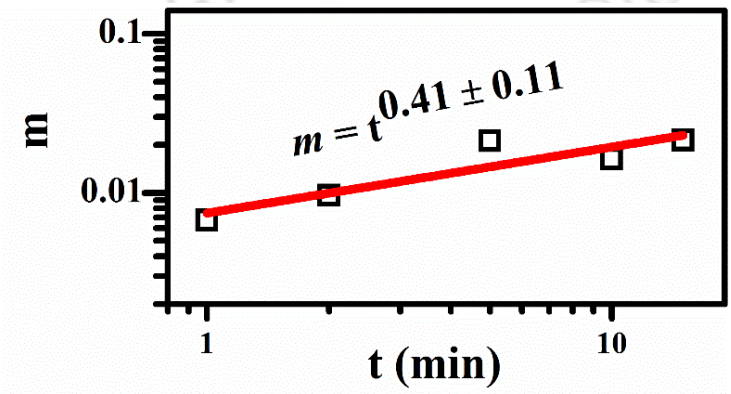

Figure 4.5 The plot of local slope m as a function of deposition time, t.

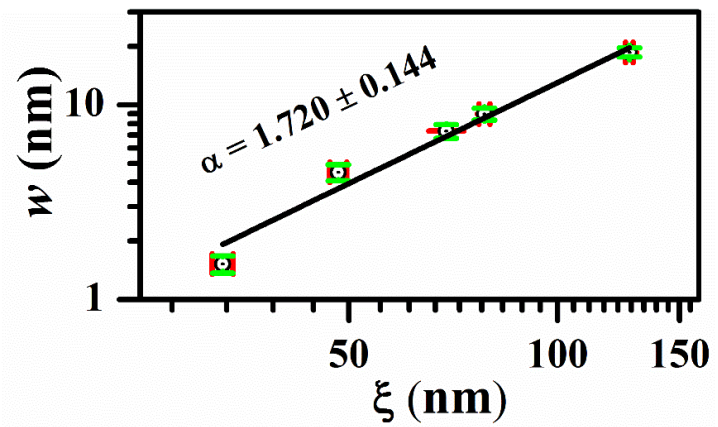

Figure 4.6 Log-log plot of w versus ξ showing linear behavior.

The observed $\alpha > 1$ suggest domination of vertical growth over the lateral growth i.e. the films roughening increased with the deposition time in the MoS_2 films.The nonzero value of β^* (as a result of inequality of α and α_{loc}) indicated that scaling behaves anomalously and reconfirms the presence of a roughness exponent in global scale.

To further investigate the anomalous scaling behavior, the power spectral density function (PSDF) of the MoS_2 films of various thicknesses was plotted in reciprocal space, *k*. The PSDF given as $P(k,t) = \frac{1}{(2\pi)^d}\left|\langle h(r,t)e^{-ik.r}\rangle\right|^2$ [146] is related to *d*-dimensional Fourier transform of surface heights, *h(r,t)* defined in reciprocal space, *k*. For an anomalous (*d* +1) dimensional system, the PSD function for anomalous scaling can be represented in frequency and time scale as, [145,151,152]

$$\text{PSD}\ (k,t) \sim \begin{cases} t^{(2\alpha+d)/z} & kt^{1/z} \ll 1 \\ k^{-\gamma}t^{2\beta^*} & kt^{1/z} \gg 1 \end{cases} \qquad (4.5)$$

where γ is $2\alpha_s + d$, *d* is spatial dimension for the scanned system, α_s is the spectral roughness exponent and $\beta^* = (\alpha - \alpha_s)/z$. On the basis of α_s, α_{loc} and α value the growth scaling behavior can be classified by Ramasco *et al.* [145] into four probable categories, namely, (i) $\alpha_s < 1$, $\alpha_{loc} = \alpha_s = \alpha$, corresponds to Family–Vicsek standard scaling; (ii) for $\alpha_s > 1$, $1 = \alpha_{loc} \neq \alpha_s = \alpha$, super-rough scaling; (iii) $\alpha_s < 1$, $\alpha_{loc} = \alpha_s \neq \alpha$, called intrinsic anomalous scaling; and (iv) $\alpha_s > 1$, $\alpha_{loc} \neq \alpha_s \neq \alpha \neq 1$ suggest a new class of scaling .

Figure 4.7(a) shows Log-Log plot of PSD versus k of the surfaces from the representative AFM images of MoS_2 films deposited on glass substrates for the duration of 20 sec, 1, 2, 5, 10 and 15 min. The PSD function did not show any characteristics peak at k_m inferring that the film grew as self-affine surface and not mounded [146]. In the PSD spectra two distinct regions, $k < t^{-1/z}$ and $k > t^{-1/z}$ represented by equation (4.5) are clearly visible. At lower k values PSD is almost saturated for all the films while at higher k regimes PSD value linearly decreased with k as PSD(k) ~ $k^{-(2\alpha_s+d)}$ where d = 2 in our case. The value of PSD increased with deposition time and the transition point between linearly decreasing and saturated regions which corresponds to ~1/ ξ are shifted towards lower k regimes corresponds to an increase in island size (~ξ) of the MoS_2 films with time.

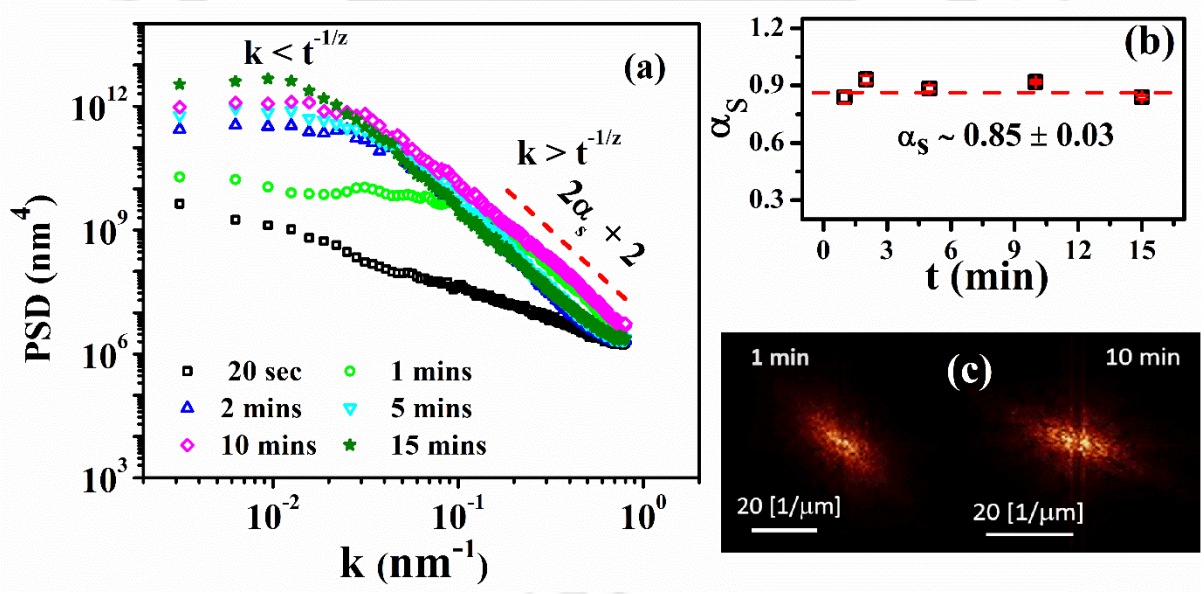

Figure 4.7 Log-Log plot of (a) PSD (k) as a function of k for MoS_2 thin films deposited on the glass substrate with different deposition times. (b) Plot of α_s of the MoS_2 films as a function of deposition time. (c) 2D FFT pattern of the AFM images of MoS_2 films deposited for 1 and 10 min.

Figure 4.7(b) shows the values of α_s estimated from the slope of each PSD plots (except that of the film deposited for 20 sec) from $k > t^{-1/z}$ regime. The average value α_s for the MoS_2 films was observed to be ~ 0.85 ± 0.03. The relevant exponents α, α_s and α_{loc} required for

classifying the category of scaling were obtained from above analysis which shows that α_{loc} $(0.89 \pm 0.01) \sim \alpha_s$ $(0.85 \pm 0.03) \neq \alpha$ (1.72 ± 0.14) and $\alpha_s < 1$. This indicates an intrinsic anomalous scaling behavior for surface growth of MoS_2 thin films [145,151]. Figure 4.7(c) showed 2D fast Fourier transform (FFT) of AFM images corresponding to MoS_2 films deposited for 1 min and 10 min. It showed a diffuse structure and absence of any bright ring-like structure in *k*-space which supports the self-affine like growth morphology excluding any type of mound formation in the surface of the films during growth [153].

In order to further verify the anomalous scaling behavior of growth of the MoS_2 films, the collapse of the HHCF and PSD dependent functions for different growth times were also investigated. Under anomalous scaling, HHCF is given as [154],

$$H(r,t) = r^{2\alpha} g_A\left(r/t^{\frac{1}{z}}\right) \tag{4.6}$$

where the anomalous scaling function, $g_A\left(r/t^{\frac{1}{z}}\right)$, behaves as

$$g_A\left(r/t^{\frac{1}{z}}\right) \sim \begin{cases} \left(r/t^{\frac{1}{z}}\right)^{-2(\alpha-\alpha_{loc})} & , \quad r/t^{\frac{1}{z}} \ll 1 \\ \left(r/t^{\frac{1}{z}}\right)^{-2\alpha} & , \quad r/t^{\frac{1}{z}} \gg 1 \end{cases} \tag{4.7}$$

Hence the function $H(r,t)/r^{2\alpha}$ when plotted as a function of $(r/t^{\frac{1}{z}})$ in the log-log scale for different deposition times should collapse into single curve and from their slopes both α and α_{loc} can be estimated [147]. Similarly, PSD function can also be expressed under anomalous scaling as [147,154],

$$PSD(k,t) = k^{-(2\alpha+d)} \psi_A\left(kt^{\frac{1}{z}}\right) \tag{4.8}$$

where the spectral scaling function, $\psi_A\left(kt^{\frac{1}{z}}\right)$, behaves as

$$\psi_A\left(kt^{\frac{1}{z}}\right) \sim \begin{cases} \left(kt^{\frac{1}{z}}\right)^{2\alpha+d} & , \quad kt^{\frac{1}{z}} \ll 1 \\ \left(kt^{\frac{1}{z}}\right)^{2(\alpha-\alpha_s)} & , \quad kt^{\frac{1}{z}} \gg 1 \end{cases} \tag{4.9}$$

Hence the function $PSD(k,t)k^{(2\alpha+d)}$ when plotted as a function of $(kt^{\frac{1}{z}})$ in the log-log scale for different deposition times should collapse into one curve and from their slopes both α and α_s can be estimated. For our case, $d = 2$, hence $PSD(k,t) = k^{(2\alpha+2)}\psi_A\left(kt^{\frac{1}{z}}\right)$ [147]. Figure 4.8(a) and Fig. 4.8(b) shows the plot of log $H(r,t)/r^{2\alpha}$ versus log $(r/t^{\frac{1}{z}})$ and plot of log $PSD(k,t)k^{(2\alpha+2)}$ versus log$(kt^{\frac{1}{z}})$, respectively for the MoS_2 films deposited for various time period (1-15 min). In fig. 4.8(a), all the curves corresponding to different time period of growth collapsed to a single curve confirming the existence of anomalous scaling with slope values of $2(\alpha - \alpha_{loc}) \sim 1.66 \pm 0.01$ and $2\alpha \sim 3.42 \pm 0.02$, for $r/t^{1/z} << 1$ and $r/t^{1/z} >> 1$, respectively. From these slopes, the values of α and α_{loc} were estimated to be 1.71 ± 0.01 and 0.88 ± 0.01, respectively, which are similar to their respective values obtained directly from the HHFC analysis as discussed earlier.

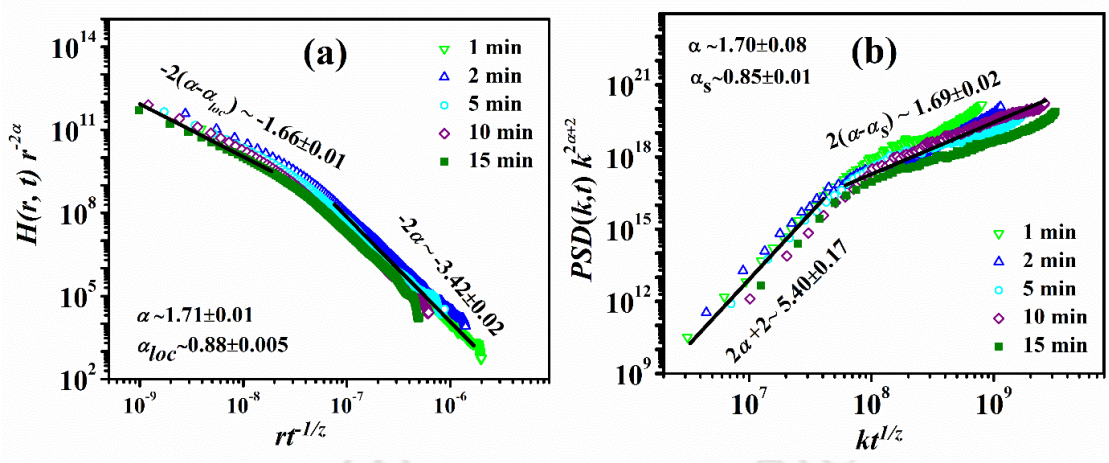

Figure 4.8 Plots of (a) log $H(r,t)/r^{2\alpha}$ versus log $(r/t^{\frac{1}{z}})$ and (b) log $PSD(k,t)k^{(2\alpha+2)}$ versus log $(kt^{\frac{1}{z}})$ showing data collapse of the anomalous scaling functions of the MoS_2 films deposited for different time periods.

Similarly, in Fig. 4.8(b), the collapse of all the PSD related curves, corresponding to different time period of growth, to a single curve confirming the existence of anomalous scaling with slope values of $(2\alpha + 2) \sim 5.40 \pm 0.17$ for $kt^{1/z} << 1$ and $2(\alpha - \alpha_s) \sim 1.69 \pm 0.02$ for $kt^{1/z} >> 1$, respectively [147]. The values of α and α_s were extracted from the average values of slopes

and were found to be 1.70 ± 0.08 and 0.85 ± 0.01, respectively. The values of α and α_s obtained from the collapse of the PSD functions were also in agreement with the values obtained above. The inequality in $\alpha > 1 > \alpha_{loc} \sim \alpha_s$ reconfirmed the presence of intrinsic anomalous scaling in the present case.

Different local models like Mullins diffusion model [155], Edwards-Wilkinson model [156] and KPZ model[157] provided ß = 0.25,0 and 0.24, α = 1,0 and 0.38 while z = 4, 2 and 1.58, respectively for 2+1 dimensions which did not match with the values of ß, α and z observed in the present case. Thus, none of the local models depicting different Universality class can exactly explain the type of growth observed here. Although the exact mechanism has not been well understood, some studies in recent years have proposed that the anomalous kinetic roughening of the surfaces with a high growth exponent arise as a consequence of nonlocal effects. Yao and Guo [158] modified the non-local KBR model [159] in sputtering growth where shadowing instability leads to the development of a mounded surface resulting in $w \sim t^{1.0\pm0.04}$ and $\xi \sim t^{0.33\pm0.02}$. Moreover, Drotar *et al.* [160] modeled the growth of a surface under shadowing (roughening effect) and higher zeroth-order sticking coefficient corresponds to minimal reemission ($s_0 = 1$ and $s_n = 0$ for $n > 0$), using a stochastic continuum growth equation,

$$\frac{\partial h}{\partial t} = v\nabla^2 h(r,t) - k\nabla^4 h(r,t) + s_0 F_0(r,t)\sqrt{1+|\nabla h|^2} + \eta(r,t)), \qquad (4.10)$$

with $F_0 = \int_0^{2\pi}\int_0^{\theta_{max}} R(\theta,\Phi)[sin\theta(\hat{\imath}cos\Phi + \hat{\jmath}sin\Phi) + \hat{\jmath}cos\theta]\,.\,\hat{n}(r)(sin\theta)d\theta d\Phi$, where θ is the local polar angle, Φ is the local azimuthal angle and $R(\theta, \Phi)$ is the distribution of the incoming flux. They simulated the film surface growth using equation (4.10) by Monte Carlo method in 2+1 dimensions giving ß = 1 and $1/z$ = 0.93 ± 0.01. The ß value predicted by the model formulated by Yao *et al.* [158] and Drotar *et al.* is close to the present work (ß = 0.88 ± 0.07) while the $1/z$ value ($1/z$ = 0.51 ± 0.08) is in between their reported values. As PLD process is directional, (flux distribution ~ $\cos^p\theta$) substrate receives incoming species at a wide distribution of angle varying from 0° to nearly $\theta_{1/2}$ (= $\cos^{-1}(1/2)^p$) [161]. $\theta_{1/2}$ is the angle between

target surface normal and flux direction where flux density becomes half of maximum in vacuum and *p* (varies from 8-20) is the parameter decided by laser spot size, laser fluence and degree of ionization of plasma . Hence, growth process occurs overwhelmingly under shadowing mechanism due to angle-dependent variable particle flux density. Hence these deposition conditions promoting large shadowing and high sticking coefficient of substrate (due to high substrate temperature of 600˚C) are suitable for surface growth under the non-local models discussed above [160].

4.3.3 Optical characterization of MoS_2 films using spectroscopic ellipsometric studies

According to the thin film structures in this work, the SE spectra were analyzed by considering a four-layered model from top to bottom as ambient/roughness/MoS_2/corning glass substrate. The roughness layer was modeled using Bruggeman effective medium approximation (BEMA) for a mixture composed of 50% MoS_2 and 50% voids within top roughness layer. BEMA is a polynomial equation and mostly use in ellipsometer to analyze the surface roughness of thin films. The objective of the approximation is to derive the optical parameters of the microscopically heterogeneous (composite state of MoS_2 and void) rough surface. Here for MoS_2 part, a dispersion relation using two Lorentz oscillators is used while for void part, the *n-k* file of void from SEA database was used. The *n-k* file database contained the predetermined optical parameters of standard materials like air, Si, Ge, SiO_2, glass, etc. For the film layer which is sandwiched between the top layer and substrate, a dispersion relation using four Lorentz oscillators was used while for corning glass and ambient *n-k* file from database of SEA software was employed to fit the experimental ψ and Δ spectra for all MoS_2 films. The numbers of Lorentz oscillators, two for surface roughness and four for thin-film layer were optimized for the best fit of the simulated spectrum with the experimental data. The real (ε_1) and imaginary (ε_2) part of dielectric permittivity considering Lorentz model are defined as,

$$\varepsilon_1(E) = \frac{f{E_0}^2(E_0{}^2 - E^2)}{(E_0{}^2 - E^2)^2 + \Gamma^2 E^2} \quad \text{and} \quad \varepsilon_2(E) = \frac{f{E_0}^2 \Gamma E}{(E_0{}^2 - E^2)^2 + \Gamma^2 E^2} \tag{4.11}$$

where E is the photon energy and f, E_0, Γ are the oscillator amplitude/strength, oscillator position and damping coefficient of Lorentz oscillator in eV. Figure 4.9(a) and 4.9(b) shows ψ and Δ spectra of the MoS_2 films fitted with the four-layered model described in the optical energy range of 1.5-3.5 eV. All the curves show good fitting with average root mean square error (RMSE) value ~ 0.7. The ψ value of MoS_2 films deposited for 15, 10 and 5 min increases in higher optical energy region while that of 1 and 2 min shows the opposite trend. The overall Δ increaseed with the increasing deposition time. The Bruggeman effective medium approximation (BEMA) model used for top layer of MoS_2 films provides two parameters called the layer thickness (d_s) and the fraction of the species (f_v - 50%, fixed in our analysis). The value of d_s is generally assumed to reflect the RMS roughness of the real surface. So far, there is no established straightforward relation between the RMS roughness, w and d_s, obtained from AFM images and ellipsometric analysis of the thin films, respectively.

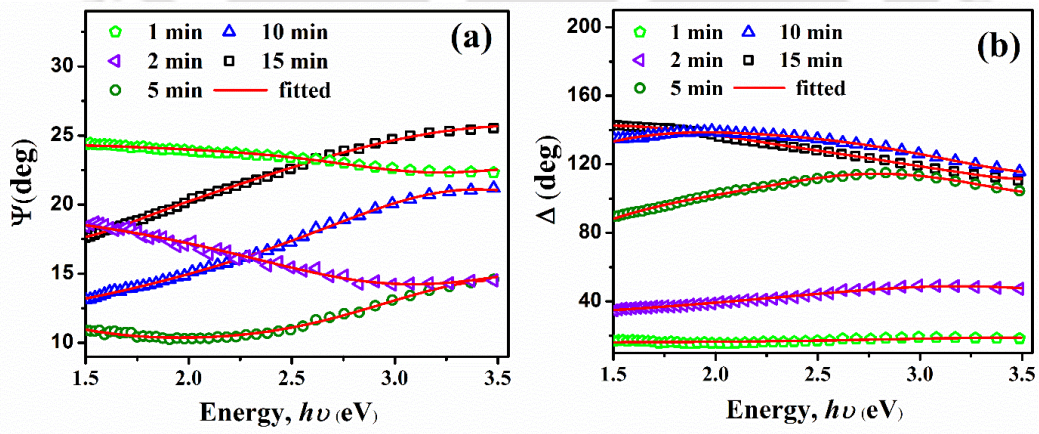

Figure 4.9 Plots of experimental and simulated SE parameters- (a) ψ and (b) Δ spectra of the MoS_2 films fabricated for 1 to 15 min.

A linear correlation between w and d_s was estimated by Fujiwara et al. for a-Si: H films though they also reported different w/d_s ratios for different growth conditions even for the same material [162,163]. In case of self-affine surfaces, the BEMA roughness (d_s) is given as the product

of average surface slope ($\delta \sim w/\xi^{\alpha}$) and the AFM surface roughness (ω), $d_s \sim \omega\delta$[164]. The average surface slope is expected to remain constant for films following dynamic scaling. On the other hand for anomalous scaling δ is not constant but varies with time as $\delta \sim t^k$, where k is a constant for a set of films deposited for different duration [165]. The values of d_s estimated from BEMA for MoS_2 films fabricated at different deposition duration were not similar to that of w (fig. 4.4 (b)) for each film. Figure 4.10 shows the variation of d_s as a function of w which shows that d_s does not vary linearly with w and their slope ($\sim\delta$) also varies with time. The inset shows the log-log plot of δ vs t where their slope $k = 0.36 \pm 0.04$. The δ estimated from growth exponents ($\delta \sim w/\xi^{\alpha}$) extracted from AFM analysis also scales with t as $\delta \sim t^{0.43\pm0.01}$ which is close to that of estimated from the slope of d_s vs w curve. The behavior of average local slope, $\delta \sim t^{0.36\pm0.04}$,

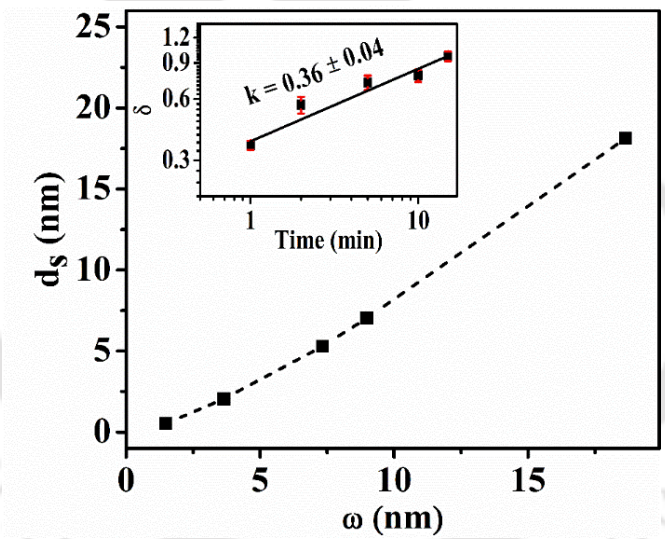

Figure 4.10 Plot of d_s vs w with an inset showing of δ vs t in log-log scale.

reconfirms the presence of anomalous scaling of growth exponents during the PLD of the MoS_2 films. Now, let us consider the SE analysis of the MoS_2 layer, sandwiched between top roughness layer and the corning glass substrate, for which a dispersion relation using four Lorentz oscillators was used. The thicknesses of the main MoS_2 layer, estimated from SE analysis, were found to be ~ 2.1, 5.5, 15.7, 37 and 77 nm for films deposited for 1, 2, 5, 10 and 15 min, respectively, which are similar to that measured from the profilometer.

Figure 4.11(a) and (b) shows the *n* and *k* spectra of the main MoS_2 layer. Both refractive index (*n*) and extinction coefficient (*k*) spectra shows an overall increase with increasing deposition duration. The *n* and *k* spectra are nearly similar to those reported by Yim *et al.* for MoS_2 films deposited on SiO_2/Si substrate by vapor phase sulfurization process [55]. The *k* spectra shows absorption peak in the range of 2.8-3.3 eV corresponding to *C/D* excitonic transitions. Figure 4.12 shows variation of (a) amplitudes (f_1, f_2, f_3, and f_4) and (b) broadening parameters (Γ_1, Γ_2, Γ_3 and Γ_4) of four Lorentz oscillators, used to describe the dispersion law for the MoS_2 film layer, as a function of deposition duration.

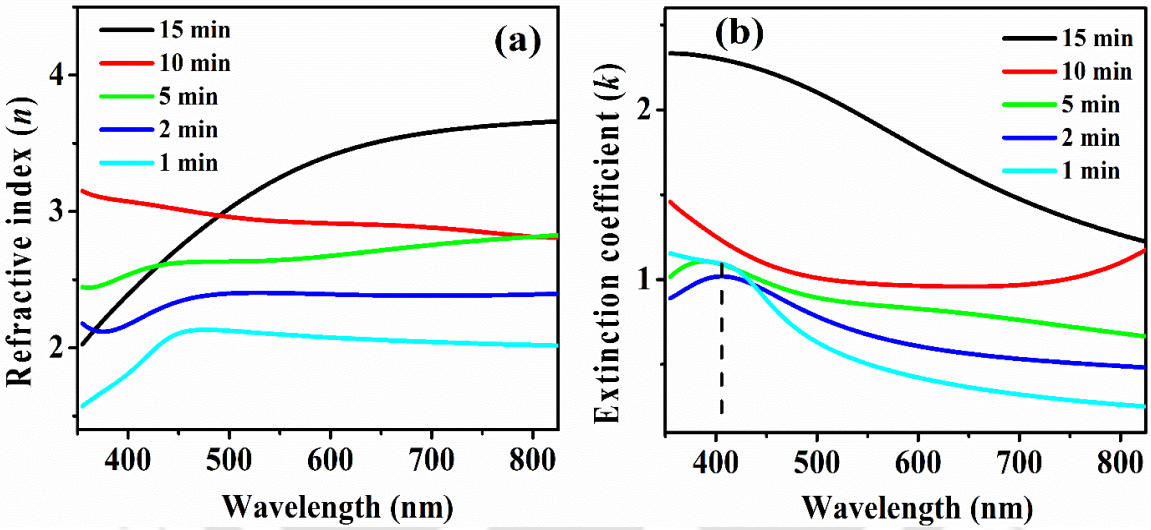

Figure 4.11 Plots of (a) n and (b) k spectra of MoS_2 films deposited for different time durations.

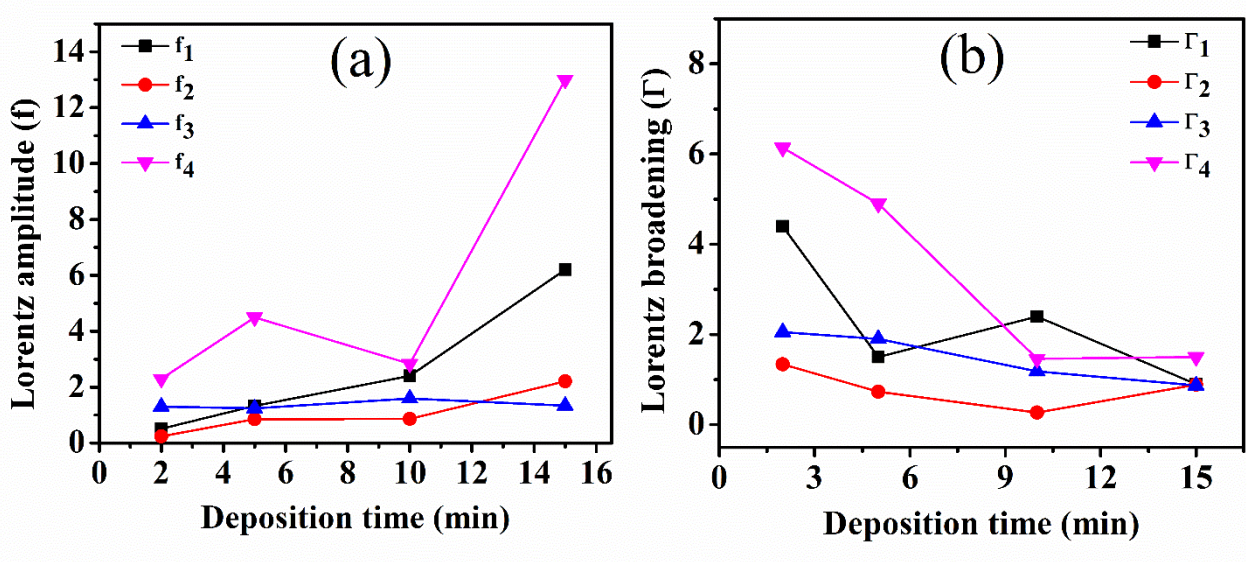

Figure 4.12 plot of (a) oscillator strength and (b) broadening of the four Lorentz oscillator used for MoS_2 layer of 2-15 min films as a function of deposition duration.

For all the four oscillators their oscillator amplitudes/strengths were observed to increase with increasing deposition duration and thickness which is an indication of the formation of denser films at longer deposition time [116]. Moreover, from AFM images (fig. 4.3) it was observed that at early stage of film growth MoS_2 clusters were sparsely distributed throughout the film but at longer deposition duration, densely packed larger clusters were formed. This morphology variation as a function of deposition duration is due to the addition of new nucleation centers as well as continuous growth of already formed nuclei at the early stages of film growth. The increase in coverage of film and cluster size ($\sim \xi$) with increasing deposition duration results in decrease in void density and consequent increase in material density of the film. From fig. 4.12 (b), a gradual decrease in broadening parameter was also observed with *t*. It was observed that, the correlation length (ξ) and crystalline grain size (shown by XRD analysis, fig. 4.2) of the MoS_2 films also increased with deposition time. Hence, the decline in Γ_1, Γ_2, Γ_3, and Γ_4 with *t* can be viewed as a result of increasing ξ (fig. 4.4(c)). The result is quite similar to the reported decrease in broadening parameter with the grain size of polycrystalline and microcrystalline silicon thin films [166]. The broadening of Lorentz oscillator is a consequence of surface scattering and lattice defect which represents the structural disorder in a sample. Thus, the reduction in Lorentz broadening parameter with growth time in the film indicates an increase in their structural order and hence enhancement in crystallinity of films was observed with increasing ξ. This enhanced structural order and crystallinity resulted in increased film compactness and density for thicker films. Now, considering similar layered model as above (depicted in fig. 4.13(a)) and considering BEMA for middle layer (sandwiched between the top roughness layer and substrate) composed of voids and a MoS_2 dispersion matrix, the void percentages within the films were estimated from SE data [167]. The void fraction present in the MoS_2 films deposited for 1, 2, 5, 10 and 15 min are found to be 15.6, 14.1, 13.6, 8.8 and 6.0 %, respectively, showing a decrease in void % with thickening of the film as

depicted in fig. 4.13(b) [168]. The increase in *n* with increasing deposition duration is due to an increase in the film density which is well supported by above observations. The increase in *k* with increasing deposition duration can also be explained as a result of an increase in the film density as well as their increasing RMS roughness. The increased surface roughness might have facilitated increased absorption due to increased surface area and enhanced light-matter interaction due to local field effect. Hence both *w* and ξ seem to play a vital role in controlling the optical parameters of MoS_2 films during their growth.

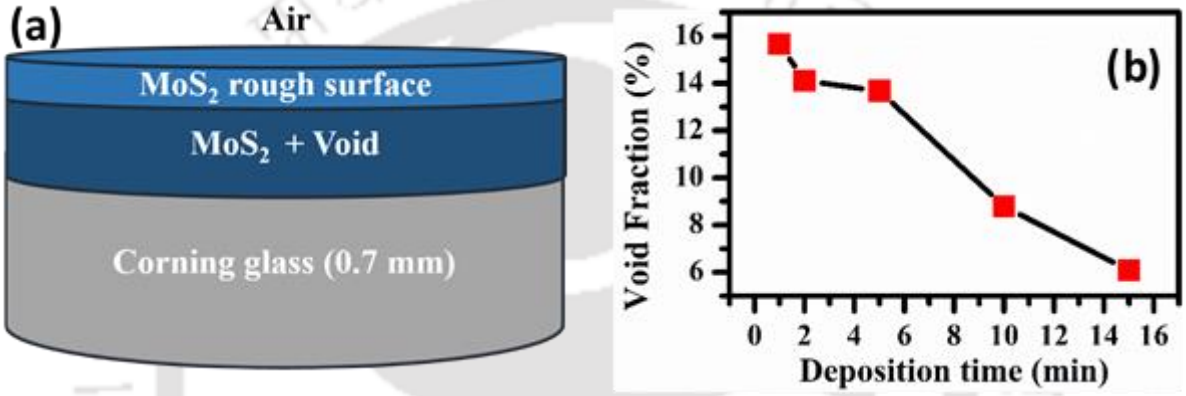

Figure 4.13 (a) 4-layer model used to extract the void % in MoS_2 films and (b) Void fraction (%) variation in the MoS_2 films with the deposition duration (min).

4.4 Growth dynamics of WS_2 thin films

4.4.1 Structural characterization of the films

Figures 4.14(a) and (b) shows the XRD pattern of WS_2 films grown on Corning glass and oxidized Si substrate, respectively. There is no significant XRD signal in the WS_2 films on glass substrate up to deposition time of 5 min and thereafter prominent XRD peaks correspond to WS_2 (002), (101) and (103) crystalline plane were observed. The XRD pattern of the films confirmed an increase in crystallinity with the deposition time. The XRD spectra of MoS_2 films deposited on oxidized Si from 30 sec to 10 min showed a sharp peak corresponding to WS_2 (104) crystalline plane while with an increase in deposition time, XRD peaks correspond to WS_2 (002), (101), (103) planes started appearing after 10 min. Hence, all the XRD peaks

(excluding (104) plane on Si substrate) showed a high broadening which suggests a poor crystalline nature of the PLD WS_2 films.

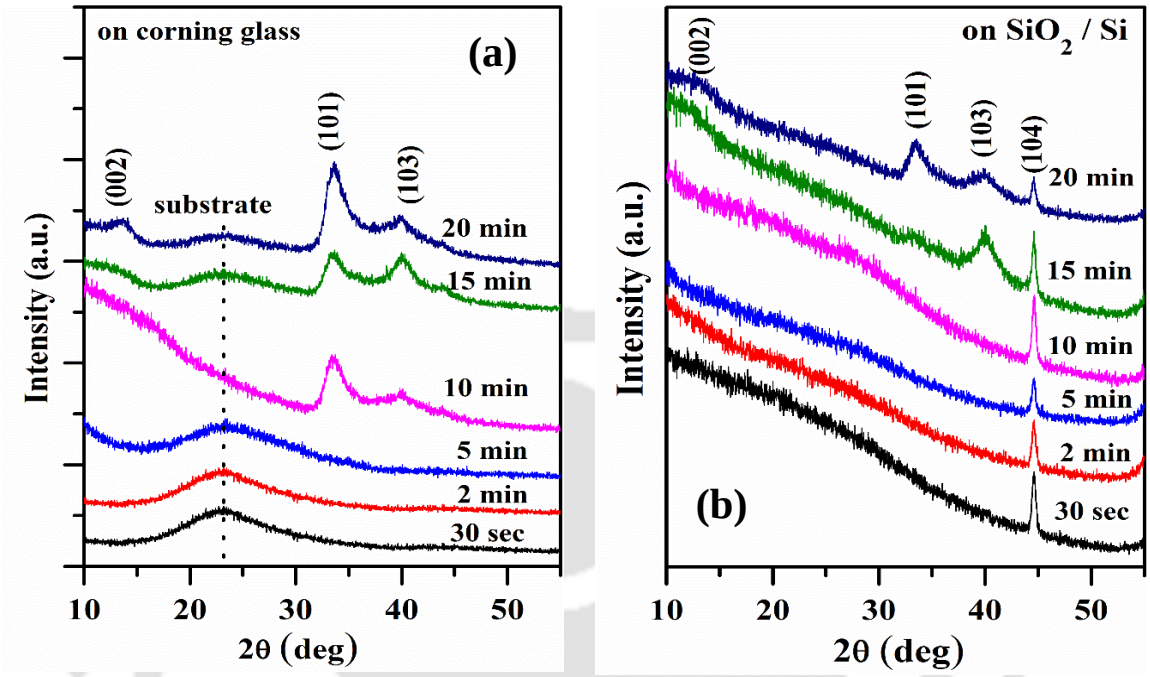

Figure 4.14. XRD pattern of WS_2 films on (a) corning glass and (b) oxidized Si substrate for different deposition times (30 sec-20 min).

4.4.2 Scaling studies of WS_2 film growth on various substrates using AFM image analysis

The surface morphology and growth dynamics of the films were characterized systematically using AFM images. Figure 4.15(a) and 4.16(a) shows the AFM images (2µm × 2µm) of WS_2 films grown onto the Corning glass and oxidized Si substrate at 400 °C substrate temperature with 30 sec, 2, 5, 10, 15 and 20 min deposition time, respectively. The scaling exponents (α_{loc}, *ß*, *1/z*) have been estimated from HHCF, $H(r,t)$, (equation 4.3) to understand the growth processes and the dynamic scaling behavior involved during PLD of MoS_2 films. From fig. 4.15 (b) and 4.16(b), it is observed that HHCF, $H(r, t)$ corresponding to the WS_2 films on glass and oxidized Si substrate increased linearly with r at small r and saturates at large r, with the asymptotic behavior predicted by equation (4.3) [169]. It is clear from fig. 4.15(b)

that *H(r, t)* shifted upward as film thickness increased with growth time up to 5 min then they almost overlapped with each other during further deposition time, which confirmed that the RMS roughness increased initially as the films grew and then got saturated after deposition time of 5 min. Figure 4.16(b) shows a systematic increment in *H(r, t)* with increasing growth time suggesting the roughening of the films with the deposition time. The HHCF curves were fitted using equation (4.3), to estimate $\alpha_{loc,}$ *w(t)* as well as ξ *(t)*. The variation of these parameters with deposition time were studied to understand the growth dynamics. Figure 4.15(c) and 4.16(c) shows the variation of α_{loc} with deposition time. The average value of α_{loc} for the films deposited onto Corning glass and oxidized Si are ~ 0.93± 0.08 and ~ 0.88 ± 0.02 respectively. In general, α_{loc} lies between 0 to 1, where, a smaller value of α_{loc} corresponds to the more locally rough surface while the larger α_{loc} of the present films corresponds to locally smooth surface. Therefore the observed value of α_{loc} suggests that the top surface of the MoS_2 films deposited onto Corning glass were smoother than the top surface of the MoS_2 films deposited on the oxidized Si.

Figure 4.15(d) and 4.16(d) shows Log−Log variations of *w* versus time (*t*) for the films deposited onto Corning glass and oxidized Si. In the case of WS_2 films on corning glass, the RMS roughness (*w*) increased linearly up to 5 min and then saturated beyond it while WS_2 films on Si showed continuous increment in *w* with deposition time. The growth exponent (β) corresponding to the WS_2 films on Corning glass and Si are 0.34 ± 0.09 and 0.46 ± 0.04. The larger β value of WS_2 films on Si substrate suggested high rate of roughening of WS_2 films surface during growth on Si substrate. Figure 4.15(e) and 4.16(e) shows ξ versus *t* plot in log scale. In the case of both substrates, the value of ξ increased as $\xi \sim t^{1/z}$ initially from 30 sec to 5 min but beyond this ξ saturated. The values of 1/*z* extracted from ξ versus *t* plot are 0.20 ± 0.02 and ~ 0.38± 0.07 corresponding to WS_2 films on Corning glass and Si substrate,

respectively. A higher value of *1/z* of WS_2 films on Si suggested a rapid increase in island size of WS_2 nanoclusters onto Si substrate.

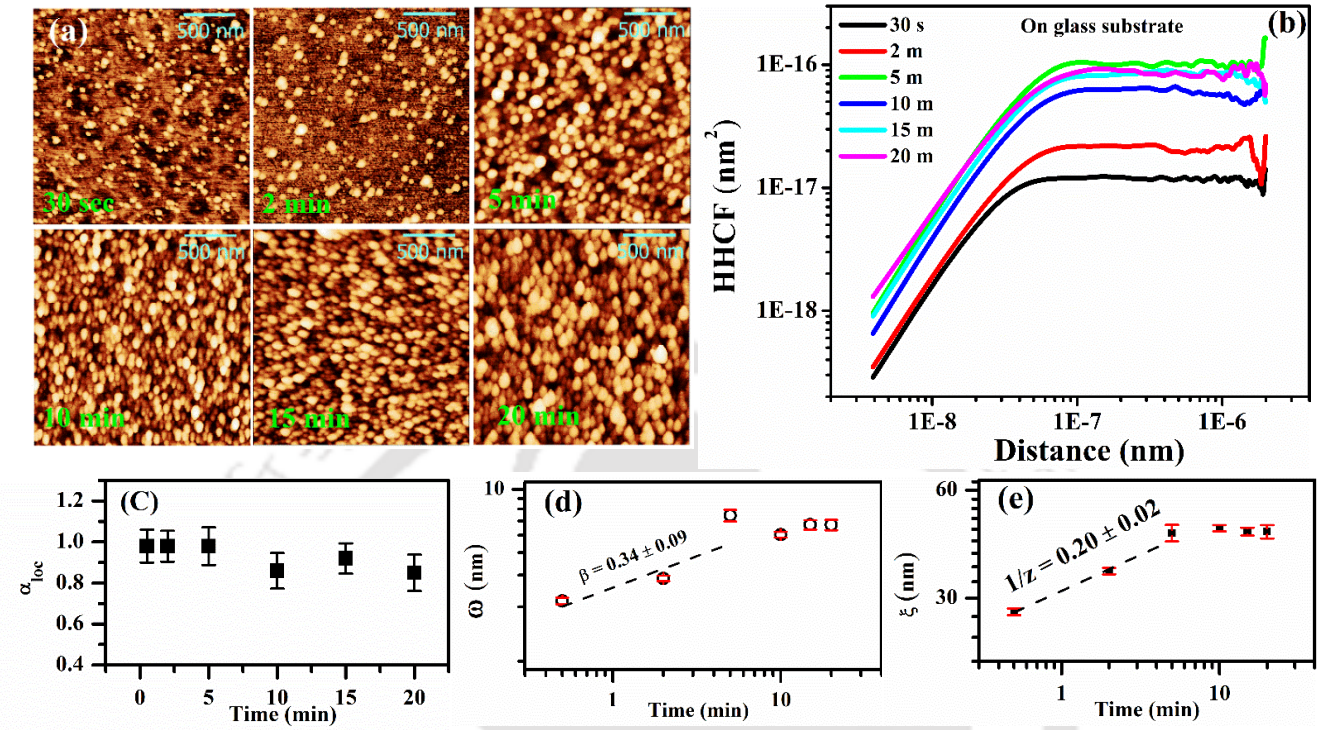

Figure

4.15 (a) AFM images of 2×2 µm scanned area of the top surface of PLD MoS_2 films on Corning glass for different deposition times 30 sec, 2, 5, 10, 15 and 20 min. (b) Log-Log plot of HHCF, H(r). The symbols are experimental data and the red solid lines are fitted with equation (4.3). Plot of (c) surface roughness w, (d) correlation length ξ, and (e) roughness exponent α_{loc} as a function of deposition time, t.

The large β and 1/z of the WS_2 films deposited onto Si compared to WS_2 films deposited onto Corning glass suggested high roughening as well as large size WS_2 nanoclusters islands formation onto Si substrate at the same deposition time. This can be attributed to comparatively high thermal conductivity and smoothness of surface of Si substrate which caused more diffusion of the adatoms to form the large size clusters in Si substrate. Hence, the WS_2 films deposited onto Corning glass grew in both vertical and lateral dimensions up to deposition time of 5 min and then saturated while the lateral growth of WS_2 films on Si substrate got fixed after 5 min deposition time but vertical growth continuously increased with the deposition time. Under dynamic scaling, $\alpha_{loc} = ßz$ but in the present study on both the substrates, dynamic

scaling failed ($\alpha_{loc} \neq ßz$) which implies the height profile may follow another scaling hypothesis called anomalous scaling where the global (α,β) and local (α_{loc}, β_{loc}) exponents are different from each other.

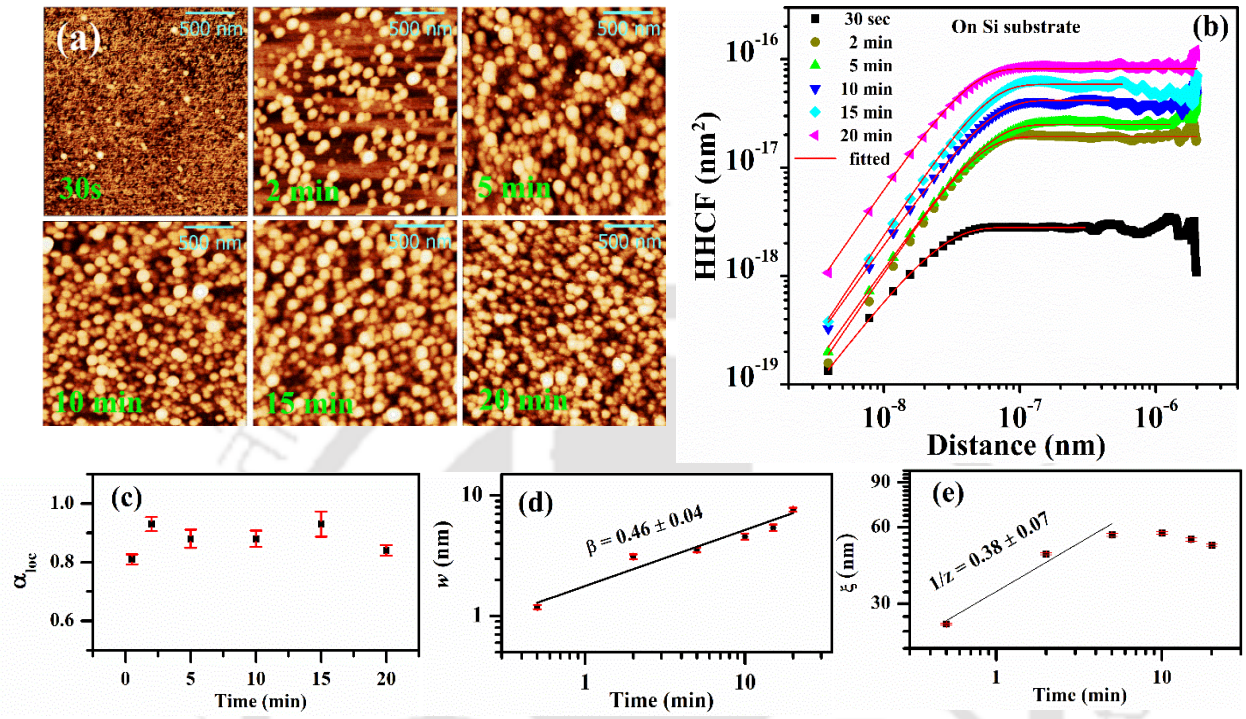

Figure 4.16 (a) AFM images of 2×2 µm scanned area of the top surface of PLD MoS_2 films on oxidized Si substrate for different deposition times 30 sec, 2, 5, 10, 15 and 20 min. (b) Log-Log plot of HHCF, H(r). The symbols are experimental data and the red solid lines are fitted with equation (4.3). Plot of (c) surface roughness w, (d) correlation length ξ, and (e) roughness exponent α_{loc} as a function of deposition time, t.

The global roughness exponents α *(~ßz)* are 1.75 and 1.21 in the case of glass and Si substrate, which are different from α_{loc}. The observed $\alpha > 1$ suggests a high surface roughening of the WS_2 films. The difference in surface evolution of WS_2 film on the two different substrates can be understood more conveniently by schematically analyzing the behavior of the evolution of ξ and ω with t as presented in fig. 4.17(a) and (b). At the initial stage of growth (30 sec) sparsely distribution of nucleated WS_2 nanoclusters were observed on both the substrates. The surface coverage of the substrate by nucleated WS_2 was less at this stage. Nucleation continued until the surface was fully covered by a maximum number of highly dense nuclei. With further deposition, the impinging adatoms were captured by the nuclei and

transformed in small size cluster. After that, around the deposition time of 2 min, a second different growth stage was observed where both ξ and ω were larger than the initial stage. This means that with increasing deposition time the WS_2 clusters grew both in lateral and vertical directions. The observation suggests that all the impinging atoms were captured by the pre-deposited WS_2 clusters and only a few new nuclei formed.

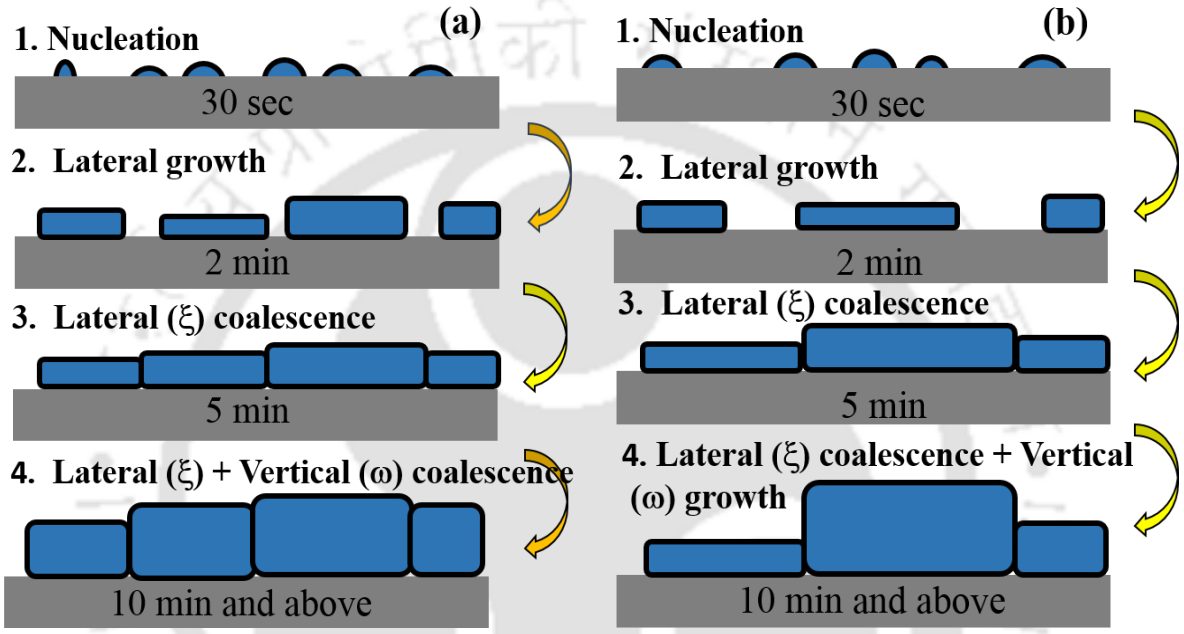

Figure 4.17 Schematic picture of the growth evolution of the WS_2 films as a function of deposition time (t) deposited onto (a) Corning glass and (b) oxidized Si substrate.

The typical vertical and lateral growth proceed by adsorption of fresh adatoms and diffusion of predeposited adatoms, and the film thickness, as well as surface coverage, increased rapidly. A further increase in the growth of ξ occurred at deposition time of 5 min. This growth stage was characterized by a coalescence of the WS_2 clusters leading to large sized clusters formation. At this stage, the cluster mobility was high and they moved along the surface and approached other clusters and led to a permanent diffusion-driven coalescence. Finally, after fully covering the substrate surface area by WS_2 clusters, lateral growth ceased while adsorptive growth progressed only in the vertical direction. During the vertical growth it was observed that while ω further increased for WS_2 films on Si substrate, it saturated in case

of WS_2 films on glass substrate [170]. The saturation of surface roughness (ω) in the case of glass substrate at higher deposition time can be realize as follows. On the glass substrate the underlying clusters (ξ) are of small sizes, as a result the freshly arrived adatoms onto the WS_2 film surface can easily equilibrate with the previous surface structure by only a small amount of particle diffusion which causes almost no change in surface roughness with further increase in deposition time above 5 min.

The growth mode and the dynamics of surface morphology of thin films can be expressed in linear and nonlinear stochastic partial differential equations. The gradients of the surface profile $h(x, t)$ for linear growth and nonlinear growth are expressed as [171],

$$\frac{\partial h}{\partial t} = a_1\nabla^2 h + a_2\nabla^4 h + \eta \qquad (4.12)$$

$$\frac{\partial h}{\partial t} = a_1\nabla^2 h + a_2\nabla^4 h + a_3\nabla^2(\nabla h)^2 + a_4(\nabla h)^2 + \eta \qquad (4.13)$$

where a_1, a_2, a_3 and a_4 are the material dependent scalar coefficients and η represents the deposition noise that exists during growth. In equation (4.13), the first term on the RHS corresponds to the deflection of the perpendicularly incident adatoms due to the interatomic forces between the pre-deposited surface atoms and the incident adatoms. The second and the third term on the RHS of equation (4.13) are associated with the microscopic mechanisms of the surface diffusion of adatoms and the equilibration of the inhomogeneous concentration of the diffusing adatoms on the surface. The fourth term on the RHS of equation (4.13) is the Kardar Parisi-Zhang (KPZ) form which corresponds to the additional volume increase caused by oblique particle incidence [157]. Films growth following equation (4.12) shows an initial increment in correlation length (ξ) with growth time (t) then saturates at higher deposition time whereas the surface roughness (ω) of the films continue to increase with the deposition time (t) [171]. On the other hand, films growth according to equation (4.13) shows an initial increment in correlation length (ξ) and surface roughness (ω) with growth time (t) then both the

parameters saturates at higher deposition time [171]. Hence in the present study growth of WS_2 films onto the glass substrate follow a nonlinear growth model (equation 4.13) while WS_2 films onto Si substrate follow the linear growth model (equation 4.12).

Different local models like Mullins diffusion model [155], Edwards-Wilkinson model [172] and KPZ model [157] provide $ß$ = 0.25,0 and 0.24, α = 1,0 and 0.38 while z = 4, 2 and 1.58, respectively for 2+1 dimensions which do not match with the values of $ß$, α and z observed in the present case. Thus, none of the local models depicting different Universality class can exactly explain the type of growth observed here. The value of growth exponentials (α, α_{loc}, $ß$, and 1/z) previously reported by Neeti *et al*., Dolbec *et al*. and Auger *et al*. in PLD and sputtered deposited metallic and semiconductor films are close to the present work [173-175]. As PLD process is directional, (flux distribution ~ $\cos^p\theta$) substrate receives incoming species at wide distribution of angle varying from 0° to nearly $\theta_{1/2}$ (= $\cos^{-1}(1/2)^p$) [161]. $\theta_{1/2}$ is the angle between target surface normal and flux direction where flux density becomes half of maximum in vacuum and p (varies from 8-20) is the parameter decided by laser spot size, laser fluence and degree of ionization of plasma. Hence, growth process occurs overwhelmingly under shadowing mechanism and angle-dependent variable particle flux density. These deposition conditions promoting non-local effects [160] like large shadowing for surface growth as observed in the PLD WS_2 films.

4.5 Conclusions:

In the present work, the kinetic roughening of MoS_2 and WS_2 thin films grown by the PLD technique was studied based on generic scaling *ansatz* using surface morphology information from AFM images of the films. In case of MoS_2 films, the characteristic exponents α_{loc} = 0.89 ± 0.05, α = 1.72 ± 0.11, α_s = 0.85 ± 0.03, 1/z = 0.49 ± 0.11 and β = 0.85 ± 0.09 were determined using the HHCF and PSD functions. The local slope increased with growth time as, $m \sim t^{\beta^*}$. The value $ß^*$ ~ 0.41 ≠ 0 confirmed that anomalous scaling occurred. The analyses

revealed the presence of intrinsic anomalous scaling of roughness with rapid roughening of the surfaces as $\alpha_s < 1 < \alpha$, $\alpha_{loc} \sim \alpha_s \neq \alpha$. The observed anomalous scaling behavior was also supported by the relation $\delta \sim t^{0.36 \pm 0.04}$ extracted from SE studies. Moreover the SE studies also suggested that the optical functions (*n* and *k*) increased during film growth depending on the evolution of *w* and ξ with *t* as they controlled their surface area and the film density. A comparative study on the growth evolution of WS_2 films with deposition time on glass and Si substrates was performed in the light of scaling theory and stochastic growth equation. The cluster size and RMS roughness of the WS_2 films on the two different substrates evolved differently with deposition time. The growth exponents (α_{loc}, *ß* and *1/z*) estimated in both MoS_2 and WS_2 films cannot be exactly related to any known universality classes based on both local and non-local growth models, suggesting that a different universality class needed to be defined. The models considering nonlocal effects like shadowing plays an important role in the evolution of growth front of these PLD thin films. Overall, the pulsed laser deposited thin films showed an increase in surface roughness with an increase in deposition time. The high roughness of the thick films provides large surface area, which is useful for various applications like photodetector, electro-photocatalyst, etc. In chapter 7, a systematic study was carried out to verify the effectiveness of the thin films of various roughness as a catalyst for hydrogen generation.

Chapter 5

Nonlinear optical characterizations of MoS_2 and WS_2 thin film

5.1 Introduction

Besides the interesting electrical and linear optical behavior, recently, notable optical nonlinearity was also observed in monolayer to few-layered MoS_2 and WS_2 thin films, nanosheets and their composite materials. As a nonlinear optical phenomenon, broadband saturation absorption was experimentally observed in MoS_2 nanosheets and its application as a passive laser mode locker was demonstrated by Zhang et al. [28]. Carlos et al. reported on the nonlinear optical properties and corresponding optical Kerr effect of mono- and few layer WS_2 films [29]. Zin et al. demonstrated a shift from saturable absorption to reverse saturable absorption of monolayer WS_2 with an increase in laser intensity [30]. In the present era, nonlinear optical materials are of great importance with their excellent modern applications like optical switcher, optical limiter, Q switcher, mode locker, harmonic generation, etc. . Nowadays various experimental techniques including degenerate four-wave mixing [176], nonlinear interferometry [177], Z-scan, ellipse rotation [178], etc. are used to determine nonlinear optical properties of materials. Among them, Z-scan technique is a simple and effective one [57]. Almost all the nonlinear optical parameters like nonlinear absorption (NLA) coefficient, nonlinear refractive index (NLR) coefficient, and nonlinear optical susceptibility can be easily obtained by Z-scan measurement. In PLD technique, among the deposition parameters, ambient gas pressure during deposition plays a significant role in deposition rate, crystallinity, stoichiometry as well as surface morphology of the deposited films [114,179]. It is known that stoichiometry, crystallinity, as well as surface morphology of a thin film strongly affects the linear and non-linear optical properties of the respective film.

In chapter 3 and 4 multilayered MoS_2 and WS_2 films were obtained by PLD for the deposition time of 5 min and with further increase in deposition time, the behavior of the films shifted to bulk-like structure. In the present chapter, the focus is to study the nonlinear optical properties of these multilayered MoS_2 and WS_2 films. In the present work, multilayered MoS_2 and WS_2 films were deposited by PLD at various argon (Ar) gas pressures. Applying various Ar pressure, film thickness, stoichiometry, crystallinity and surface morphology of the deposited films modified and their corresponding effects on nonlinear optical properties were explored in detail. The linear optical properties of the WS_2 films were investigated with UV-Vis spectroscopy and spectroscopic ellipsometry while the nonlinear optical properties measured by Z-scan setup using He-Ne laser of wavelength 632.8 nm as the excitation source. Optical limiting was shown to be one of the possible application of theWS_2 thin films.

5.2 Experimental details

MoS_2 films were deposited by PLD technique onto corning glass (transparent substrate required for NLO characterization of thin films using Z-scan setup) substrate heated to 600 ℃ under Ar gas atmosphere at a pressure of 10^{-1}, 10^{-2}, and 10^{-5} mbar, respectively. WS_2 films were deposited by PLD technique at various Ar gas pressures. The films were deposited onto Corning glass at the substrate temperature of 400 ℃ under Ar gas atmosphere at a pressure of 10^{-1}, 10^{-2}, and 10^{-5} mbar, respectively. All the films were deposited for 5 minutes. Nonlinear optical properties of the films were obtained by performing Z-scan experiment. Z-scan experimental set-up was explained in detail in chapter 2, section 2.6.

5.3 NLO properties of MoS_2 films

The Z scan experiment was performed for a few layered MoS_2 films deposited onto corning glass (deposition time 20 sec). The normalized open aperture (OA) and closed aperture

(CA) transmittance spectra of the film are shown in fig. 5.1 and as can be seen that no significant nonlinear signal from the sample is observed.

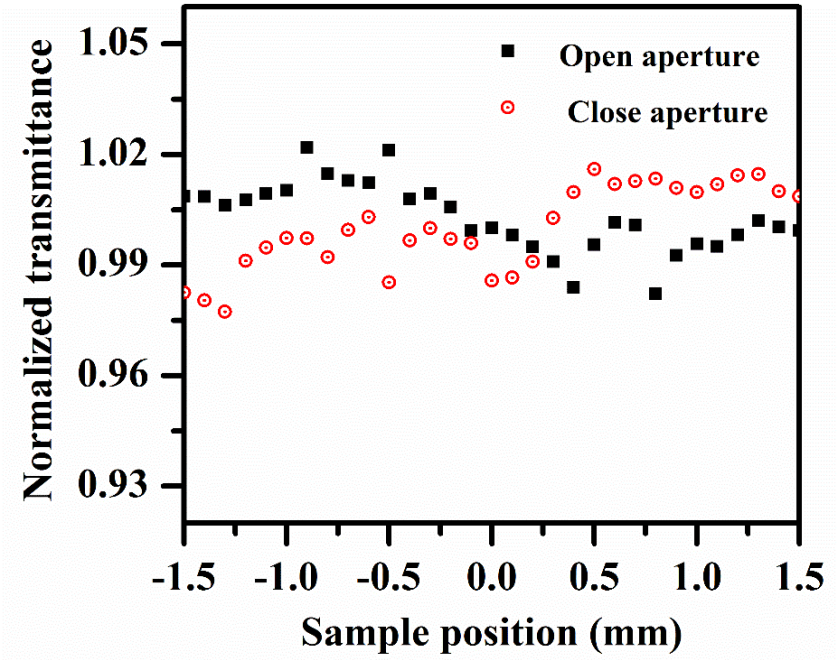

5.1 Normalized open aperture and closed aperture Z-scan transmittance of a few layered MoS_2 film on corning glass substrate.

Z-scan experiment was then carried out for multilayered thick MoS_2 films. MoS_2 films were deposited at Ar gas pressure atmosphere of 10^{-1}, 10^{-2} and 10^{-5} mbar, respectively for the ablation time of 5 min. The linear absorption coefficient 'α' and thicknesses of the films were extracted from spectroscopic ellipsometer analysis of the films. Thicknesses of the films were 50.5, 43.5 and 34.2 nm for the films at deposition pressure of 10^{-1}, 10^{-2} and 10^{-5} mbar, respectively. Figures 5.2 (a), (b) and (c) show the normalized transmittance plot for open aperture Z-scan as a function of the sample position w.r.t. focus of the lens for MoS_2 thin films deposited at Ar gas pressures of 10^{-1}, 10^{-2}, and 10^{-5} mbar, respectively. The experimental data were fitted to the transmission profiles given by equation (2.1). The open Z-scan of all the films exhibited the transmittance minima at $z = 0$ and transmittance increased symmetrically on both sides of $z = 0$. The transmission pattern indicates reverse saturation absorption (RSA)

phenomenon in the sample. The nonlinear absorption coefficient, β' was calculated from the fitting parameter *c*, obtained from the normalized transmittance data of the open aperture Z-scan measurement after fitted to equation (2.1).

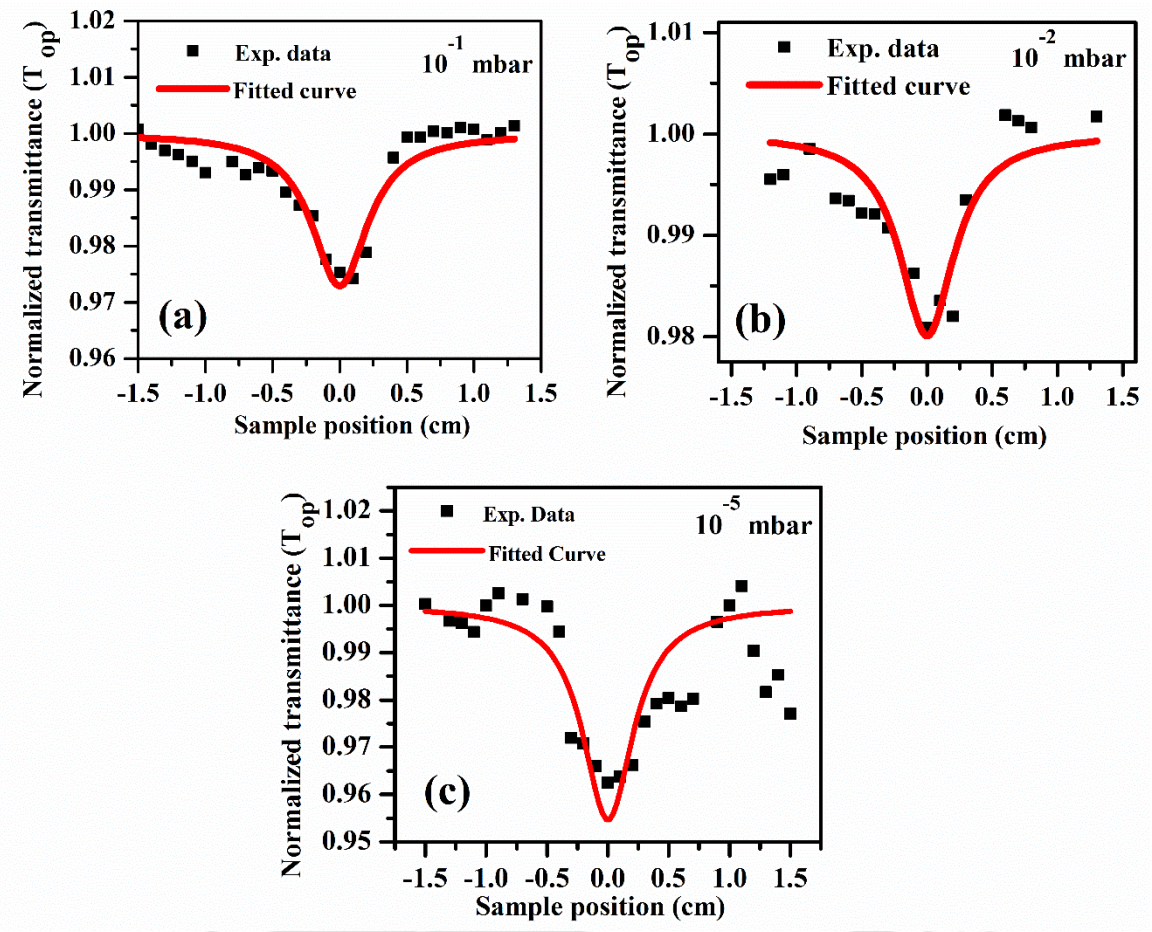

Figure 5.2 Open z-scan normalized transmittance intensity of MoS_2 thin films deposited in Ar gas pressure of (a) 10^{-1}, (b) 10^{-2} and (c) 10^{-5} mbar.

Figures 5.3 (a), (b) and (c) show the normalized transmittance plot for closed aperture Z-scan as a function of the sample position w.r.t focus of the lens for MoS_2 thin films deposited at Ar gas pressures of 10^{-1}, 10^{-2}, and 10^{-5} mbar, respectively. In the closed aperture Z-scan, normalized transmission curves shows a transmittance minimum (valley) prior to focus followed by a transmittance maximum (peak) after focus for all the films. This valley-peak signature indicates the self-focusing property, which corresponds to the positive nonlinear

refractive index n_2. n_2 was calculated from the closed aperture Z-scan measurement after fitted to equation (2.2).

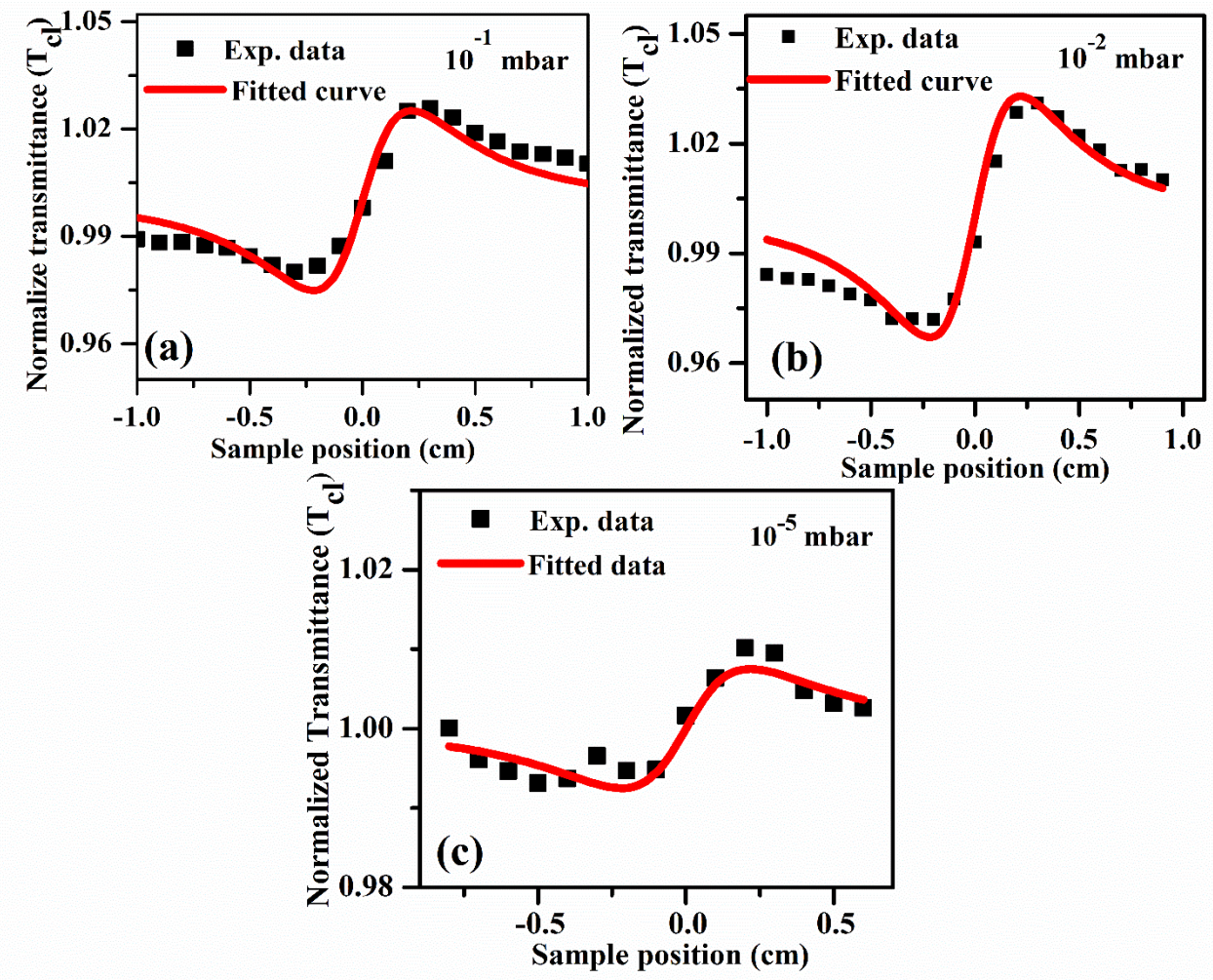

Figure 5.3 Closed z-scan normalized transmission intensity of MoS_2 thin films deposited in Ar gas pressure of (a) 10^{-1}, (b) 10^{-2} and (c) 10^{-5} mbar.

Table 5.1 shows the variation of nonlinear absorption coefficient (*ß'*) and nonlinear refractive index (n_2) of MoS_2 thin films with decreasing Ar pressure. The variation of β' and n_2 of the MoS_2 thin films as a function of deposition pressure is also presented graphically in fig 5.4. The β' for the MoS_2 films decreased from 10.5 to 3.13 cm/W, with an increase in Ar pressure from 10^{-5} to 10^{-1} mbar. The n_2 for the MoS_2 films decreased from 13.68×10^{-4} to 6.89×10^{-4} cm^2/W, with an increase in Ar pressure from 10^{-5} to 10^{-1} mbar which suggest the

MoS_2 film deposited at high vacuum is optically denser than MoS_2 films deposited at high Ar pressure.

Table 5.1 α, β, and n_2 for the MoS_2 films deposited at different Ar pressures.

Ar Pressure (mbar)	**Linear absorption coefficient, α** $(cm^{-1})\times10^3$	**Film thickness** (nm)	**Nonlinear absorption coefficient, β'** (cm/W)	**Nonlinear Refractive index, n_2** $(cm^2/W)\times10^{-4}$
10^{-1}	3.3	50.5	3.13	6.89
10^{-2}	3.9	43.5	3.61	10.50
10^{-5}	5.5	34.2	10.5	13.68

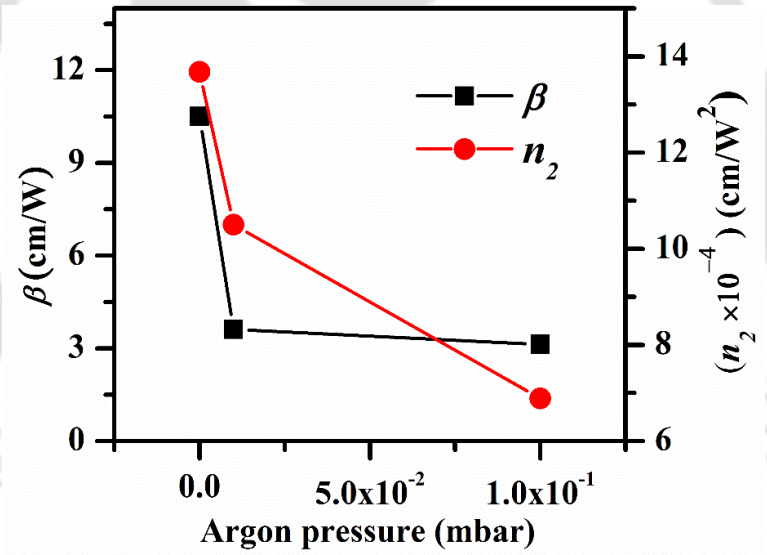

Figure 5.4 β' and n_2 of MoS_2 thin films as a function of deposition Ar pressure.

For the third-order nonlinearity, the relation between the Rayleigh length (z_o) of incident laser beam and spatial separation between peak and valley (Δz_{pv}) along scanning direction is given by equation, [58]

$$\Delta z_{pv} = 1.7 z_0 \tag{5.1}$$

The measured value of z_o for He-Ne laser focused by convex lens of focal length 5 cm is 2.5 mm. The measured valley-to-peak separation of 4.2 mm, which is nearly 1.7 times of Raleigh length (z_0 = 2.5 mm), confirms the presence of positive third order nonlinearity in the MoS_2 films. The measured β' and n_2 are higher by an order of 10^{11} compared to the reported β' and n_2, measured by femtosecond laser of ultrathin MoS_2 films [60]. However, similar order of β' and n_2 were observed in MoS_2 nanoflakes where Z-scan measurement was performed under a diode laser source of wavelength 532 nm [180]. Since our experiment was performed with CW laser, the laser-induced heating effect was the cause in the significant thermal enhancement of β' and n_2.

5.4 NLO properties of WS_2 thin films

The NLA and NLR coefficient of the WS_2 films were obtained by fitting the open and closed aperture transmitted beam of different positions with the respective position dependent transmitted intensity formulae. Figures 5.5 (a), (b) and (c) show the plot of open aperture (OA) normalized transmittance of the WS_2 films deposited at the Ar pressures of 10^{-1}, 10^{-2}, and 10^{-5} mbar, respectively. In the X-axis of the plots, focus point of the lens considered as z = 0 position and the sample was translated on both sides of the focus point up to ±15 mm in an interval of 1 mm. The measured open aperture Z-scan transmitted beam was fitted with equation (2.1). The transmitted beam showed valley (i.e. minimum transmittance) at the focused point followed by a symmetric structure with respect to the center (z = 0) i.e. the films showed RSA. Ningning et al. and Zin et al. also reported RSA in monolayer WS_2 (bandgap ~2.1 eV) by 2PA of femtosecond laser pulse of wavelength 800 nm (~ 1.55 eV) and 1040 nm (~ 1.19 eV) [30,31]. The nonlinear absorption coefficient, β' was calculated from the normalized transmittance data of the open aperture Z-scan measurement after being fitted to equation (2.1).[73,181-183] The thickness of the films (L), measured by ellipsometer, were found to be 12, 33, and 27 nm at Ar

pressure of 10^{-1}, 10^{-2}, and 10^{-5} mbar, respectively. Further, the linear absorption coefficient (α) at the laser wavelength (632.8 nm) was extracted from the ellipsometer spectra analysis

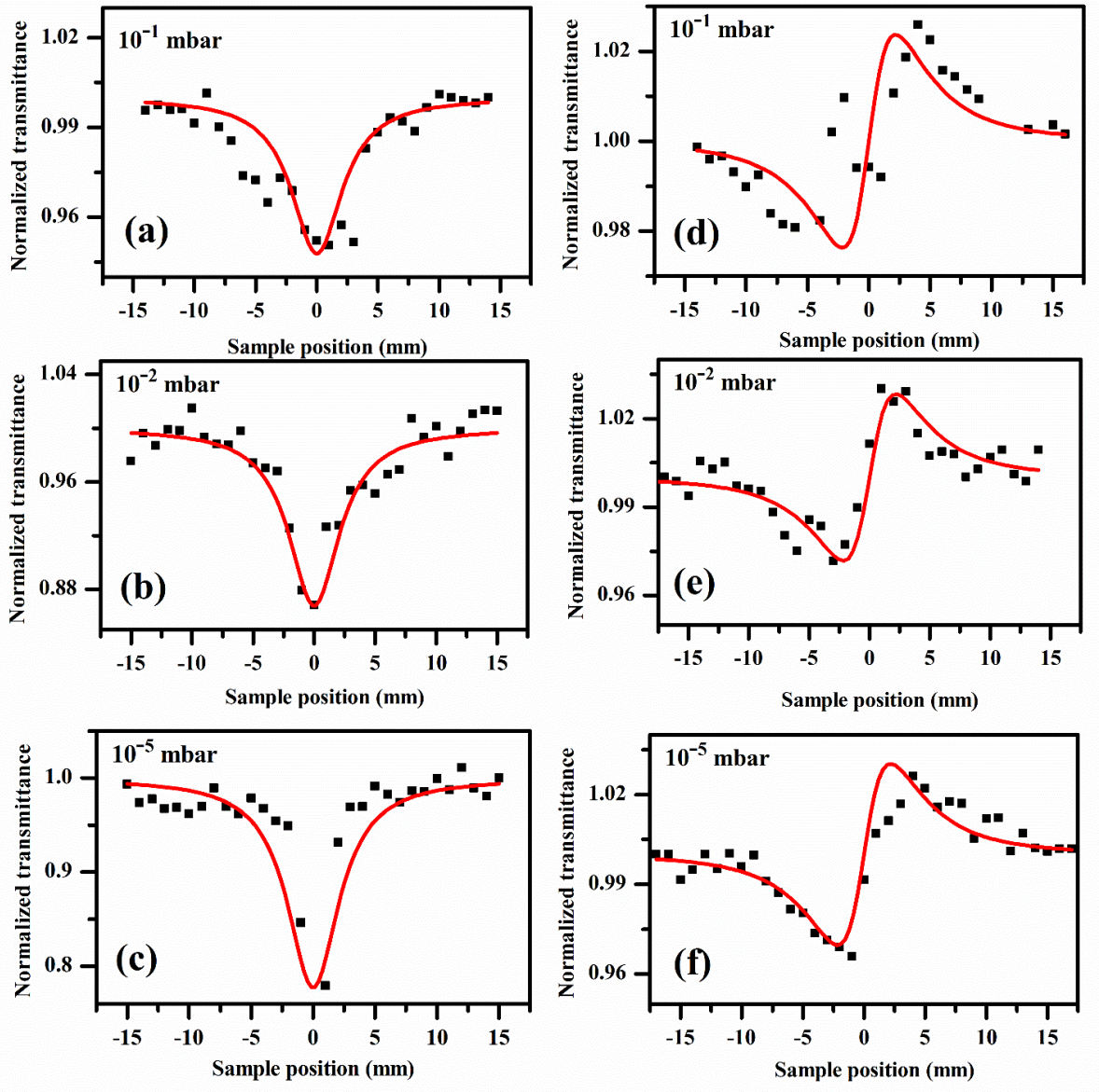

Figure 5.5 The plot of open Z-scan normalized transmission intensity of WS_2 thin films deposited in Ar gas pressure of (a) 10^{-1}, (b) 10^{-2}, and (c) 10^{-5} mbar. The plot of closed Z-scan normalized transmission intensity of WS_2 thin films deposited in Ar gas pressure of (d) 10^{-1}, (e) 10^{-2}, and (f) 10^{-5} mbar.

of the respective films. Figures 5.5 (d), (e) and (f) shows the plot of closed aperture (CA) normalized transmittance of the samples prepared at the Ar pressure of 10^{-1}, 10^{-2} and 10^{-5} mbar, respectively. Further, n_2 of the films was extracted by fitting equation (2.2) with the close

aperture transmission beam as shown in figures 5.5 (d), (e) and (f). It was observed that the closed aperture transmission beams possessed valley (transmission minimum) before the focus position ($z = 0$) and a peak (transmission maximum) after the focus position. This valley-peak position in the closed aperture transmission beam is due to the self-focusing phenomenon of the film which corresponds to the positive nonlinear refractive index (n_2) of WS_2 films. The real (χ_R^3) and imaginary (χ_I^3) third-order nonlinear optical susceptibility of the WS_2 films were calculated using equations (2.4) and (2.5) and corresponding third-order nonlinear optical susceptibility (χ^3) was calculated using equation (2.6) [114]. The calculated values of n_2, β', χ_R^3, χ_I^3 and χ^3 of the WS_2 films are listed in table 5.2.

A significantly large value of β', n_2, χ_R^3 and χ_I^3 was observed in the S deficient nanocrystallites WS_2 films as compared to the reported nonlinear optical parameters of monolayer, multilayer, bulk-like WS_2 films measured by Z-scan technique with a pulsed laser source (nano and femtosecond) [29-31]. B' and n_2 of the WS_2 films were around 10^5 times larger than that of monolayer WS_2 under fs-pulsed laser irradiation as reported by Zin et al. [30] whereas, χ_R^3 and χ_I^3 in the present work is 10^6 and 10^7 times higher than that observed in monolayer WS_2 under fs-pulsed laser as reported by Ningning et al. [31]. χ^3 was also found to be 10^7 times higher than the reported value in monolayer to multilayered WS_2 films under ns-pulsed laser by Carlos et al. [29]. However, similar order of β' and n_2 were observed in MoS_2 nanoflakes, where Z-scan measurement was performed under a diode laser source of wavelength 532 nm [180]. Hence, observed large values of NLO coefficients of the nc-WS_2 films in the present work were promoted by the high energy excitonic states created by quantum confinement effects as well as by continuous wave (CW) laser induced heating effects. In quantum confinement region, the oscillator strength enhances and interaction of the local electric field of the light with nanostructures becomes stronger as observed earlier in nc-SiO_2 thin films [114]. Figure 5.6 shows the variation of β' and n_2 of WS_2 thin films as a function of deposition Ar pressure where with

decrease in deposition pressure a gradual increase in the nonlinear optical coefficients β' and n_2 of the WS_2 films were observed. Earlier, in section 5.3, similar NLO behavior was also noticed in MoS_2 thin films. It was observed that for the similar deposition Ar pressure the nonlinear optical coefficients (β') are larger in case of WS_2 thin films while NRI (n_2) of the MoS_2 films are larger than WS_2 films.

Table 5.2. Nonlinear optical coefficients (β', n_2, χ^3_R, χ^3_I and χ^3) of WS_2 thin films deposited for 6 min at various Ar gas pressure.

Ar Pressure (mbar)	**Nonlinear refractive index, n_2 (cm^2/W)×10^{-4}**	**Nonlinear absorption coefficient, β' (cm/W)**	**Real 3rd order susceptibility, χ^3_R(esu) ×10^{-2}**	**Imaginary 3rd order susceptibility, χ^3_I(esu) ×10^{-2}**	**3rd order susceptibility, χ^3(esu) ×10^{-2}**
10^{-1}	1.10	17.34	0.97	1.31	1.63
10^{-2}	1.67	27.40	3.02	2.05	3.65
10^{-5}	1.67	45.50	6.70	3.16	7.41

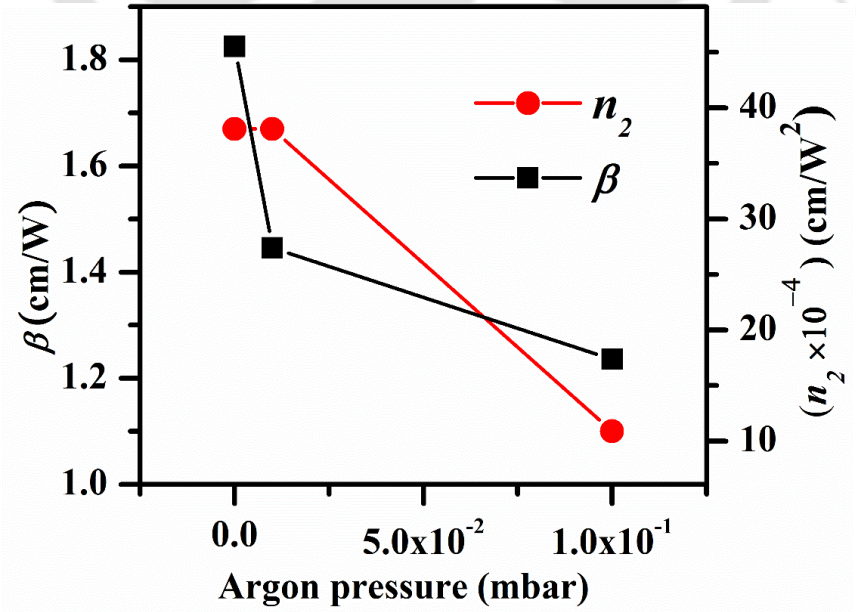

Figure 5.6 β' and n_2 of WS_2 thin films as a function of deposition Ar pressure.

In the present study, Z-scan experiment was performed under CW laser illumination, where the incident laser beam is absorbed by the optical material and induced considerable thermal heating in the samples. The high temperature of the illuminated portion of the material leads to a change in the NLO properties of the material. Hence thermally induced optical nonlinearities cause large NLO coefficients in the WS_2 films [184,185]. In a high absorbing medium, the change in refractive index caused by laser heating process is expressed as [184],

$$\Delta n = \left(\frac{dn}{dT}\right)\left(\frac{w_0}{2}\right)^2\left(\frac{I\alpha}{k}\right) \tag{5.2}$$

where, k is coefficient of thermal conductivity of the optical material and w_0 is the radius of the laser beam. Hence Δn ~10^{-4} cm^2/W which indicates that in the case of CW laser the thermal nonlinearity dominates over optical nonlinearity.

5.5 Optical limiting in MoS_2 and WS_2 thin films

The optical limiter is an important device for protecting human eye and sensors from the exposure to high power laser beam. An ideal optical limiter should show linear optical transmission for lower intense input laser power and above a threshold laser power, the transmission remains constant [186]. Getting an ideal optical limiting response from a single material is very difficult. Varieties of materials like suspension dyes, SiO_2, Si nano-crystal, C_{60}/toluene, etc. are characterized with optical limiting properties [187]. Practically the materials which show nonlinear absorption can be used as an optical limiter. Possessing a large nonlinear absorption coefficient (β') with RSA response the WS_2 films may be effective as an optical limiter material. Figure 5.7 (a) shows the characteristic optical limiting behavior of the WS_2 films measured by the Z-scan setup (as shown in fig. 2.8) where the sample was placed at the location of focused laser beam (z = 0) and the transmitted output power was measured with step by step increase in the input laser power.

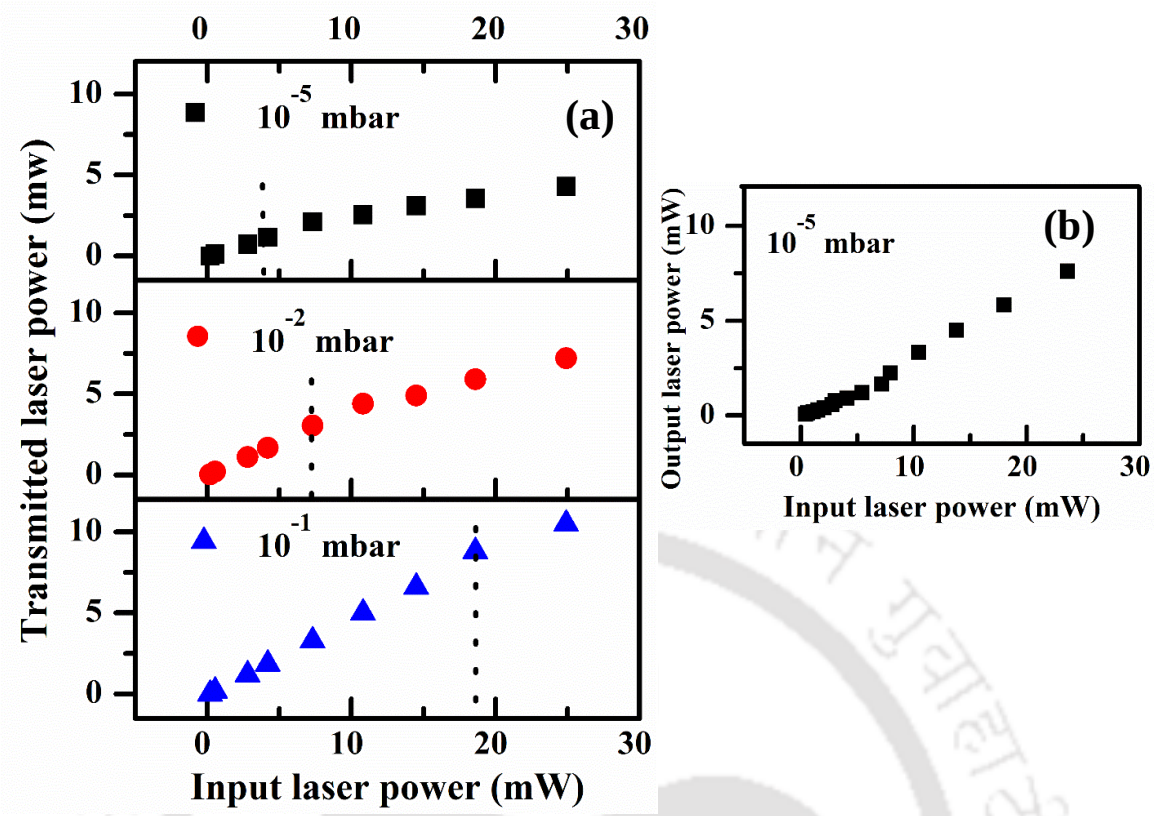

Figure 5.7 Optical limiting response of (a) the WS_2 thin films deposited at various Ar gas pressure and (b) MoS_2 film deposited at 10^{-5} mbar.

From fig. 5.7 (a) it is clearly observed that initially the transmitted output power linearly varied with the input laser power but with further increase in laser power, the output power gradually deviated from its linear behavior and moved towards saturation.The starting point of deviation from linear nature is referred as optical limiting threshold point. It is observed that the threshold point is shifted from lower input laser energy to higher energy (4.2, 7.3 and 18.6 mW, respectively) with an increase in deposition pressure from 10^{-5} to 10^{-1} mbar. Hence the WS_2 film of higher *β'* value appears as more efficient optical limiter material [188]. Figure 5.7 (b) shows the optical limiting characteristics graph of MoS_2 film deposited at 10^{-5} mbar. In case of the MoS_2 film, no significant optical limiting effect was observed. Hence, the optical limiting phenomenon was too weak in MoS_2 film due to the weak nonlinear optical absorbance (*β'*) value of the MoS_2 film.

5.6 Conclusion

MoS_2 and WS_2 multilayered thin films were deposited using PLD technique at various Ar gas pressures. *As*-deposited films showed interesting nonlinear optical properties. The third-order optical nonlinearity of the MoS_2 and WS_2 films was measured by Z-scan setup with a He-Ne laser source. All the films showed nonlinear reverse saturation absorption (β') and positive nonlinear refractive index (n_2). CW laser-induced thermal nonlinearity dominated over optical nonlinearity and caused an anomalously large value in the nonlinear optical parameters like n_2, β' and χ^3. However, nonlinear absorbance of the WS_2 films were stronger than the MoS_2 films. Optical limiting phenomena was observed in WS_2 films attributed to the strong nonlinear absorbance optical limiting and the limiting threshold power increased with increasing Ar gas pressure due to decrease in β'. Surprisingly the optical limiting phenomena was absent in the as-deposited MoS_2 films.

भारतीय प्रौद्योगिकी संस्थान गुवाहाटी
Indian Institute of Technology Guwahati

Chapter 6

MoS_2 and WS_2 quantum dots synthesis by pulsed laser ablation in liquid

6.1 Introduction

Along with the 2D layered structure, QDs of MoS_2 and WS_2 also established their usefulness in various optoelectronic and sensing devices [32-35]. QDs have direct bandgap energy compared to the indirect bandgap of MoS_2 and WS_2 bulk counterpart. By synthesizing the QDs of different sizes one can tune the bandgap of the QDs attributed to the quantum confinement effect. Both the MoS_2 and WS_2 QDs are nontoxic, have bandgap in the visible region, chemically and thermally stable with a noticeable high efficiency seems to be a good alternative of the existing toxic QDs like PbSe, CdAs, etc. There have several reports on the synthesis of 2D materials QDs by various processes like multi exfoliation based on lithium intercalation, hydrothermal route, wet-grinding assisted co-solvent sonication, probe assistant ultra-sonication, solvent assisted sono-chemical exfoliation process, etc. [32,33,75,76]. As a drawback, the multi exfoliation process consumes a lot of time and produces chemical hazardous. Hydrothermal process needs thermal treatment for a longer period. Among various tedious and time-consuming processes, PLAL technique shows a great possibility as an efficient, single step, simple physical process to synthesize MoS_2 and WS_2 QDs. In PLAL technique the ablation parameters like laser fluence, laser wavelength, ablation time, liquid medium, etc. can play a significant role in regulating the shape, size, density of particles and optical properties of the synthesized nanoparticles [189-191]. To the best of our knowledge, so far there has been no systematic study on the efficacy of PLAL parameters on controlling the shape and size and corresponding optical behavior of the generated QDs of 2D materials. In the earlier chapters, monolayer to multilayered MoS_2 and WS_2 films were deposited by PLD technique at various

laser fluences and ablation times. In the present work, instead of deposition inside a vacuum chamber, MoS_2 and WS_2 solid targets immersed in distilled water (DW) were ablated by pulsed laser and instead of thin films, MoS_2 and WS_2 nanostructures like nanosheets, QDs were synthesized. Like the previous chapters, the effect of laser fluence and ablation time on nanostructures shape and size and their optical properties were investigated systematically. The shape and sizes of the QDs were characterized by TEM and AFM images. All the samples were subjected to Raman spectra and XRD analysis to study the crystalline properties of the QDs. Further, the optical properties were investigated by recording the PL spectra, UV-Vis spectra, TRPL of the respective QDs. Chemical stability of the QDs was determined by measuring their Z potential.

6.2 Experimental details

MoS_2 and WS_2 QDs were synthesized from a solid bulk-MoS_2 target by PLAL experiment. The PLAL experimental details were discussed in section 2.5. All the samples were prepared in distilled water as dispersed liquid medium. At a fixed laser energy, the experiment was performed at various ablation times of 5, 10 and 20 min. QDs were also synthesized at various laser energies of 10, 20 and 40 mJ at a fixed ablation time. Post-synthesis characterizations of the MoS_2 and WS_2 QDs were performed using the following instruments. The sizes of the QDs were measured by TEM and AFM images, crystallinity of the samples was estimated by Raman, XRD, HRTEM and SAED analysis. The optical behavior of the samples was characterized by UV-Vis, PL and TRPL analysis.

6.3 MoS_2 QDs synthesis by PLAL

6.3.1 Laser ablation at various ablation time

Three different samples were prepared by ablating solid MoS_2 target at three different ablation times of 5, 10 and 20 min at a fixed laser energy of 40 mJ. The minimum ablation time

was chosen to 5 min to produce a sufficient amount QDs to carry on all the analysis and the ablation process was done at the highest ablation time of 20 min to avoid interruption in the ablation process due to the high density of QDs. Another sample was prepared between the extreme ablation times, at 10 min to find out the effect of ablation times on the size and optical properties of MoS_2 QDs. The pre- and post- centrifuged colloidal MoS_2 QDs solution were drop-casted onto Cu grid to perform TEM analysis. Figure 6.1 shows the TEM image of pre-centrifuged MoS_2 QDs solution prepared by laser ablation for 20 min at the laser energy of 40 mJ. Along with MoS_2 nanoparticles, a large quantity of MoS_2 nano-sheets was also observed in the TEM image. A similar type of mixed MoS_2 nanostructures were also observed in the samples obtained at other ablation times. So, the ablation process produced a mixed solution of MoS_2 nanoparticles and nanosheets.

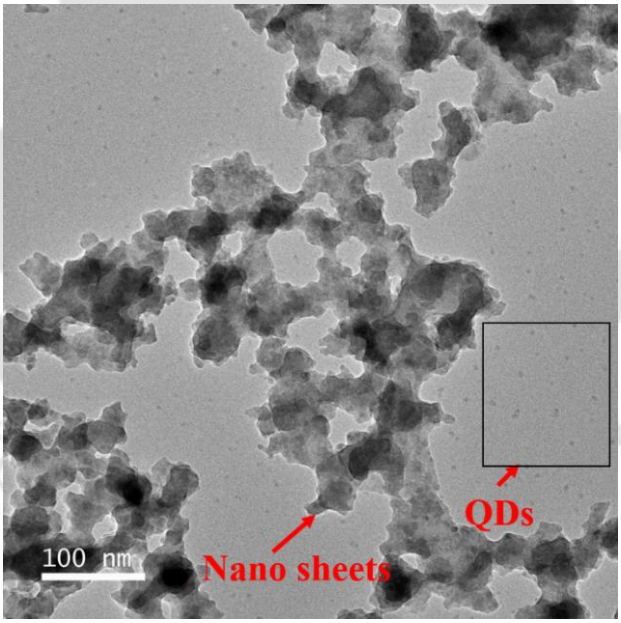

Figure 6.1 TEM image of laser ablated pre-centrifuged MoS_2 sample.

Figure 6.2 (a), (b) and (c) shows the TEM image of the post-centrifuge supernatant solutions which were synthesized at the laser ablation time of 5, 10 and 20 min, respectively. All the images showed distribution of MoS_2 nanoparticles without the presence of MoS_2

nanosheets. Hence, after centrifugation, most of the nanosheets were precipitated at the bottom of the container and the supernatant solution mostly contained MoS_2 nanoparticles. In supernatant solution, most of the MoS_2 nanosheets were removed. Inset of fig. 6.2 (a), (b) and (c) shows the size distribution of the *as*-synthesized nanoparticles, where the sizes of the nanoparticles were distributed in the range of 2-7, 2-5 and 4-8.5 nm with an average particle size of 4, 2.91 and 6.13 nm at the ablation time duration of 5, 10 and 20 min, respectively. We know the excitonic Bohr radius of MoS_2 crystal is ~23 nm [192]. In all the samples the average size of MoS_2 nanoparticles were well within the excitonic Bohr radius of MoS_2 crystal. Therefore, the nanoparticles can be considered as MoS_2 QDs. Among the three samples, average QDs size was found to be minimum (~ 2.91 nm) at 10 min ablation time and then increased to ~ 6.13 nm at the ablation time of 20 min. The result can be understood as follows, Initially, with an increase in the ablation time from 5 to 10 min, the dispersed QDs or nanoparticles in DW further absorbed laser light and fragmented into smaller size. Further in increase in the ablation time, though the fragmentation process was going on, the high density of QDs resulted in the agglomeration of QDs and as a result, the effective size of the QDs increased.

To analyze the crystalline properties of the film, the high-resolution TEM (HRTEM) images and selected area electron diffraction (SAED) patterns were also recorded. Fig. 6.3 (a) and (b) are the corresponding HRTEM image and SAED pattern of the MoS_2 QD nanocrystals. The *d* spacing obtained from HRTEM image was 0.27 nm corresponding to the (100) plane of MoS_2 [192]. SAED pattern exhibited a sharp hexagonal diffraction spot corresponding to the crystalline 2H-MoS_2 structure [193]. SAED pattern also depicted hexagonal MoS_2 (100), (110) crystalline plane which confirmed the crystallite MoS_2 QDs formation.

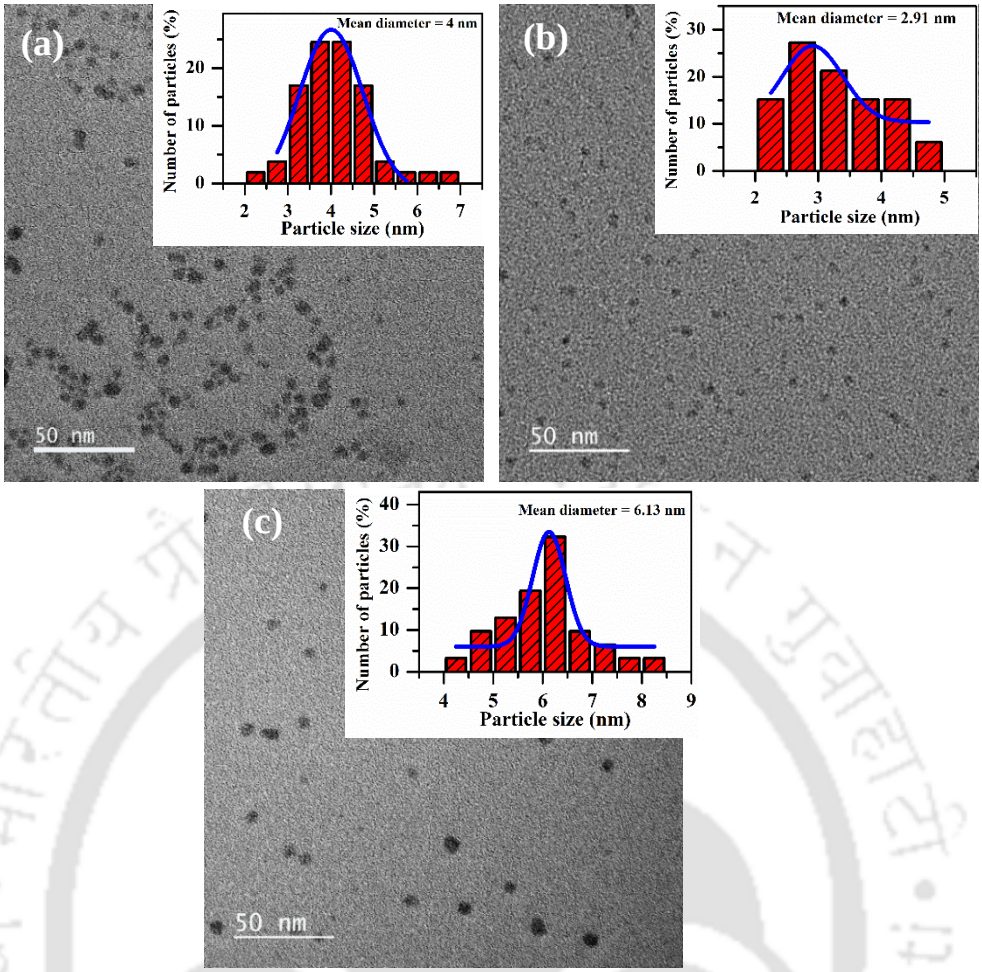

Figure 6.2 TEM images of MoS_2 QDs, synthesized at the ablation time of (a) 5, (b) 10 and (c) 20 min at the laser energy of 40 mJ. Inset of each image show the size distribution of the MoS_2 QDs.

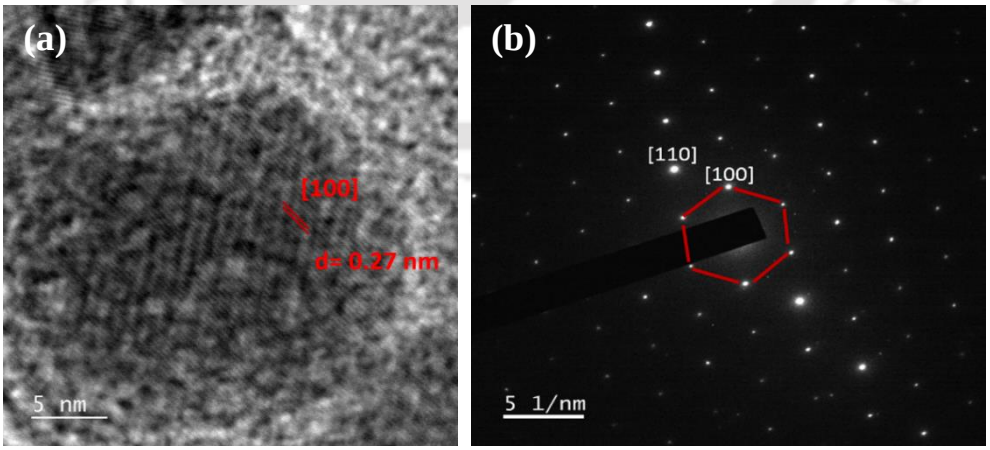

Figure 6.3 (a) HRTEM image and (b) SAED pattern of MoS_2 QDs prepared at the laser energy of 40 mJ for 20 min ablation time.

AFM measurements were performed to confirm the morphology and thickness of the as-prepared MoS_2 QDs. Figure 6.4 (a), (b) and (c) shows the AFM images of the PLAL MoS_2 QDs at ablation time of 5, 10 and 20 min, respectively. The corresponding height profiles are shown in fig. 6.4 (a), (b) and (c) for of each of the AFM images revealed the thickness of the surface containing QDs of the respective samples. The heights of the QDs were ~ 4.5, 3.7 and 6.5 nm for the samples at ablation time of 5, 10 and 20 min which are almost similar to the lateral length of the respective QDs as shown in TEM images.

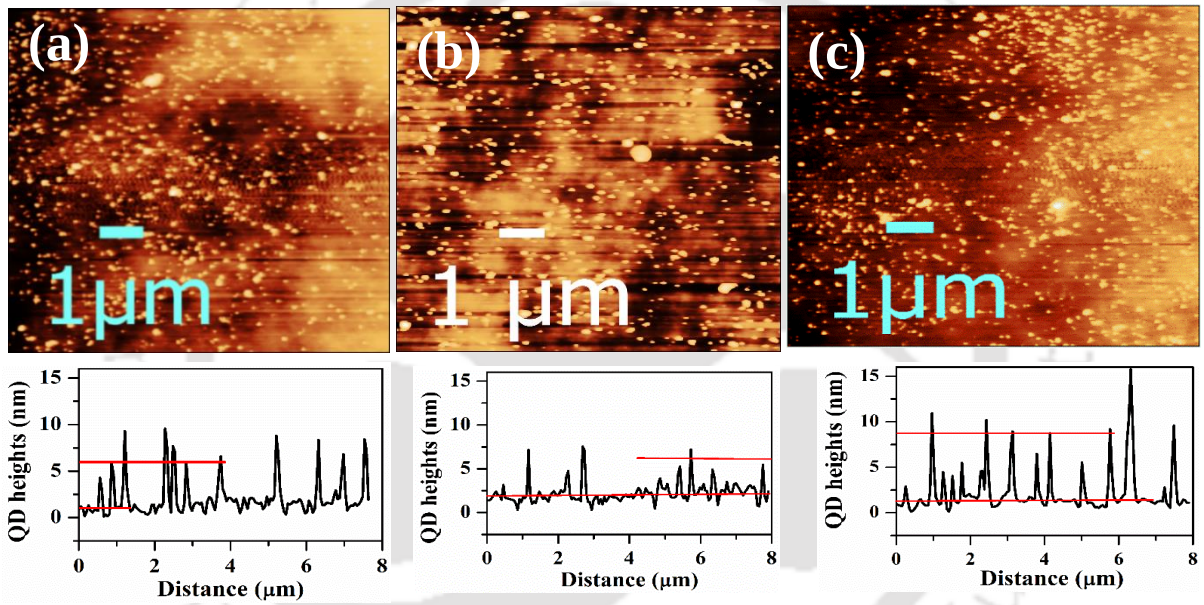

Figure 6.4 AFM images along with particle height profile of the PLAL MoS_2 QDs at the ablation time of (a) 5, (b) 10 and (c) 20 min.

Figure 6.5 shows the XRD patterns of MoS_2 QDs and the MoS_2 solid target. MoS_2 target shows XRD peaks at 14.53, 29.14, 44.29 and 60.25 deg corresponding to the (002), (004), (006) and (110) crystalline planes of hexagonal phase MoS_2, with (002) peak being the most intense one [192]. In the case of MoS_2 QDs, the XRD peak corresponds to (002), (004) and (006) planes with (002) plane being the most prominent.

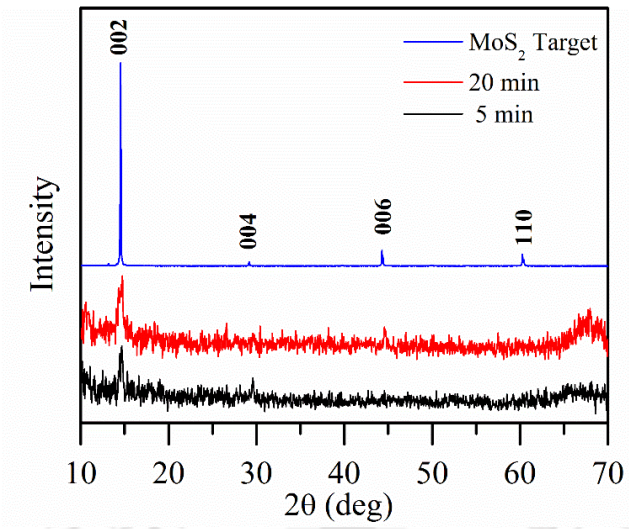

Figure 6.5 XRD pattern of the MoS_2 target and drop casted MoS_2 QDs onto Si substrate.

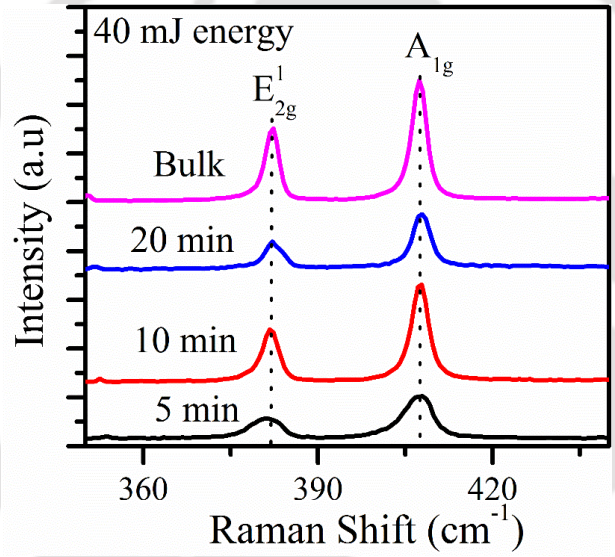

Figure 6.6 Raman spectra of the MoS_2 QDs synthesized at various ablation times.

Figure 6.6 shows the Raman spectra of MoS_2 QDs at ablation time of 20, 10, and 5 min along with the bulk MoS_2 target. Each spectrum exhibit two prominent Raman peaks corresponding to A_{1g} and E^1_{2g} Raman modes of MoS_2 [117]. The E^1_{2g} and A_{1g} Raman modes showed thickness dependent peak positions. The difference in peak position of A_{1g} (blue shifted) and E^1_{2g} (red shifted) mode increased with an increase in MoS_2 layer numbers from monolayer to higher order [117,192]. The peak positions corresponding to A_{1g} mode were observed

at 407.8, 407.5, 406.7 and 407.8 cm^{-1} while that corresponding to E_{2g}^1 at around 382.1, 381.7, 381 and 381.7 cm^{-1} for the MoS_2 QDs at the ablation time duration of 20, 10, and 5 minutes and bulk MoS_2, respectively. The peak difference between the two Raman modes, ΔF, in the respective cases were found to be 25.7, 25.8, 25.6 and 26.1 cm^{-1}. Raman peak difference of the QDs samples are similar to multilayered MoS_2 films. The height of the QDs were like multilayered thick MoS_2 (as discussed in AFM analysis) which caused a multilayered MoS_2–like Raman signature.

Figure 6.7 shows the EDX spectra of the MoS_2 QDs prepared by ablating the MoS_2 target for 20 min at a laser energy of 40 mJ with inset showing the % of each atomic elements of MoS_2. The atomic percentage of S and Mo were found to be 65.5 and 34.5 for the MoS_x structure corresponding to x = 1.9, which confirmed almost stoichiometric MoS_2 QDs formation. Similar EDX spectra and S to Mo atomic ratio were also observed in MoS_2 QDs synthesized at 10 and 5 min ablation time.

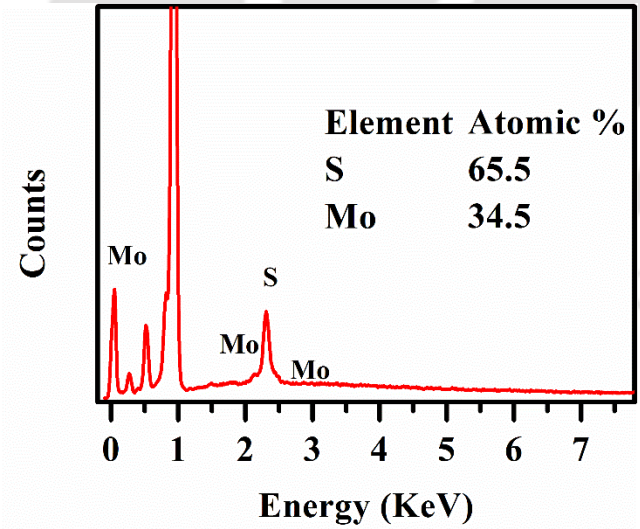

Figure 6.7 EDX spectra of MoS_2 QDs synthesized at a laser energy of 40 mJ at the ablation time of 20 min.

Figure 6.8 (a) shows the UV–Visible absorption spectra of pulsed laser ablated MoS_2 QDs in DW at various ablation times at a fixed laser energy of 40 mJ. The MoS_2 QDs solution

shows an absorption edge at ~ 310 nm. Hence, the strong blue-shift during optical absorption of the as-prepared MoS_2 QDs is attributed to the quantum confinement and edge effects when the lateral size of the MoS_2 QDs is reduced to equal or less than the excitonic Bohr radius of MoS_2 (~23 nm). According to TEM results, the majority of the *as*-prepared MoS_2 QDs are in the range of 2–8.5 nm which is well within the excitonic Bohr radius of MoS_2. Similar UV-Vis spectra of MoS_2 QDs were also reported in the literature [32,76,77]. An enlarged view of the UV-Vis spectra in the range of 450-750 nm is depicted in fig. 6.8 (b) where two characteristic absorption peaks corresponding to A (at 609 nm) and B (at 669 nm) excitonic transition were observed [46]. The A/B excitonic transitions are observed in monolayered to multilayered MoS_2 films [44,46]. Hence the presence of low-intensity A/B transition peaks in UV-Vis spectra of the QDs solutions suggests that even after centrifugation some amount of layered MoS_2 nanosheets remained in the QDs solutions.

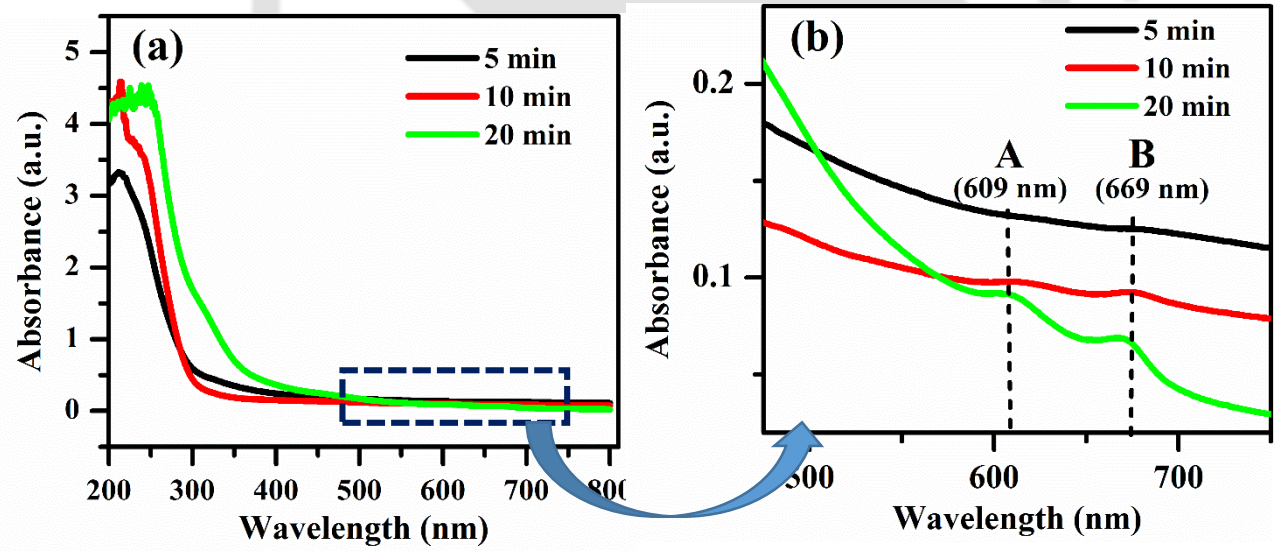

Figure 6.8 The plot of (a) UV-Vis spectra of the MoS_2 QDs synthesized at various ablation times at the laser energy of 40 mJ and (b) an enlarged view of the UV-Vis spectra (450-750 nm range).

To investigate the recombination kinetics of photo-generated charge carriers, TRPL measurements were performed for colloidal MoS_2 QDs using a 308 nm diode laser excitation

source. The emission spectra of the QDs were monitored at 435 nm. Figure 6.9 exhibits the typical PL decay of the dispersed MoS_2 QDs solution prepared at various ablation times. All the recorded TRPL spectra were fitted with a single exponential decay equation, convoluted with a Gaussian instrument response function as given by the equation

$$I(t) = \int_{-\infty}^{t} IRF(t')exp\left(-\frac{t-t'}{\tau}\right)dt' \quad (6.1)$$

where τ is the photon-excited carrier lifetime. From the fitting of PL decay curve, the estimated carrier lifetime was found to be ~3.67, 4.24 and 3.10 ns, for MoS_2 QDs synthesized by laser ablation for the time duration of 5, 10 and 20 min, respectively. Correlating with the average particle size distribution as shown in fig. 5, it was observed that with decreasing particle size, the radiative lifetime becomes progressively longer which was in accordance with the earlier reported result by Subhrajit et al. on MoS_2 QDs colloidal solution [34]. The observed photo-excited carrier lifetime is much longer than previously reported complex multi-exponential carrier lifetime of ~70 ps for layered MoS_2 structure [194]. The longer lifetime of the carrier does provide high stability of charge carrier in the MoS_2 QDs solution. The slow decay of the carrier also results in increase in PL intensity of the respective samples [195].

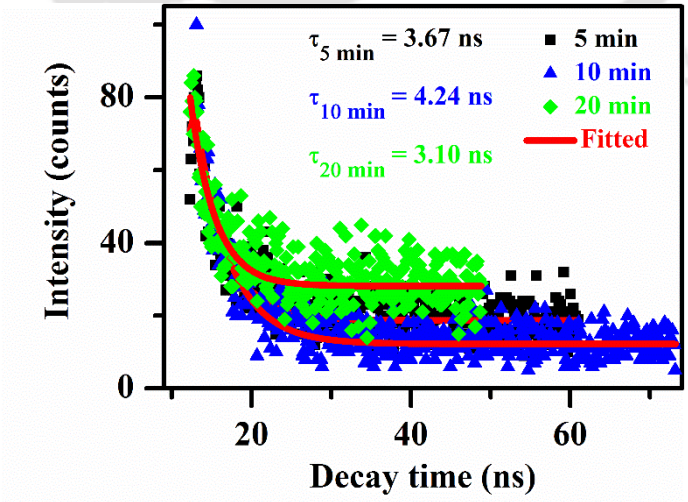

Figure 6.9 TRPL spectra with zero IRF background of the MoS_2 QDs synthesized at different laser ablation times at a fixed laser energy of 40 mJ. The inset shows the details of the lifetime of carriers in different samples.

Zeta potential is a key parameter to measure the stability of colloidal solution. It defines the magnitude as well as positive or negative nature of the effective surface charge of the corresponding double layer around the colloid particle [196]. Generally, a dispersed solution with zeta potentials higher than ± 30 mV is considered as stable dispersion with a high interparticle electrostatic repulsion [197]. Figure 6.10 shows the plots of the zeta potentials of the MoS_2 QDs solutions at various ablation times at a fixed laser energy of 40 mJ. Zeta potentials of the QDs samples at ablation time 5, 10 and 20 min were -35.1, -38.6 and –30.5 mV, respectively. The QDs solution at ablation time 10 min shows high dispersion stability (-38.6mV) while it is reduced to -30.5 and -35.5 mV at 20 and 5 min ablation time. Comparing with the average size of the QDs it was observed that with reduction of the QDs size stability of the solution increased. Recently, significant use of a stable MoS_2 solution as biomarker and organic solar cell has been reported in the literature [198,199].

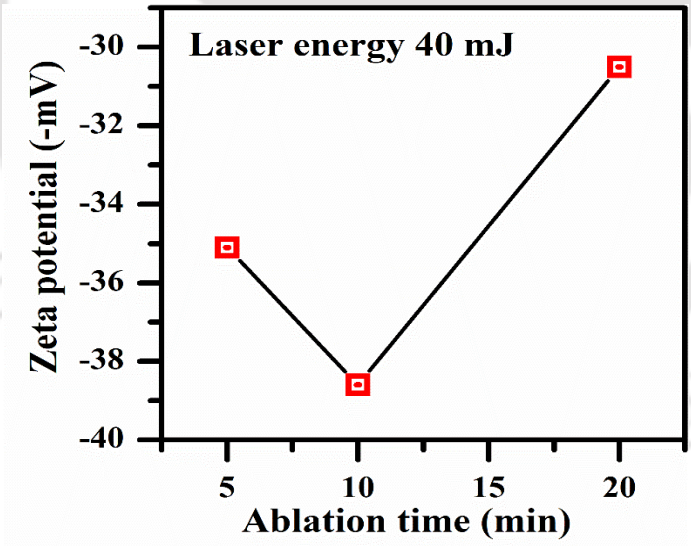

Figure 6.10 Zeta potentials of the MoS_2 QDs solutions at various ablation times.

Due to the quantum confinement effect, the position of the peaks was blue-shifted compared to the monolayer band gap energy (1.9 eV). Hence, no significant difference in PL intensity and FWHM of the PL spectra were observed in all the samples. The high ablation rate and wide size distribution of QDs at the high laser energy (40 mJ) may be the cause of the

result. The recorded PL spectra of the MoS_2 colloidal solution with an excitation wavelength of 290 nm (xenon lamp source) are shown in Fig. 6.11 (a). All the PL spectra showed broadening in the range from 310 to 550 nm due to the distribution in QDs size. The *as*-observed PL spectra of the QDs solution generated at 5, 10, 20 min laser ablation of the MoS_2 solid target were deconvoluted into 4-5 peaks by fitting with a Lorentzian function which is shown in fig. 6.11 (b), (c) and (d), respectively. At 5 min laser ablation, the deconvoluted peaks of PL spectra were observed at 348.5 (3.5 eV), 379.6 (3.2 eV), 406.8 (3.0 eV), 434.0 (2.8 eV) and 461.6 (2.6 eV) nm.

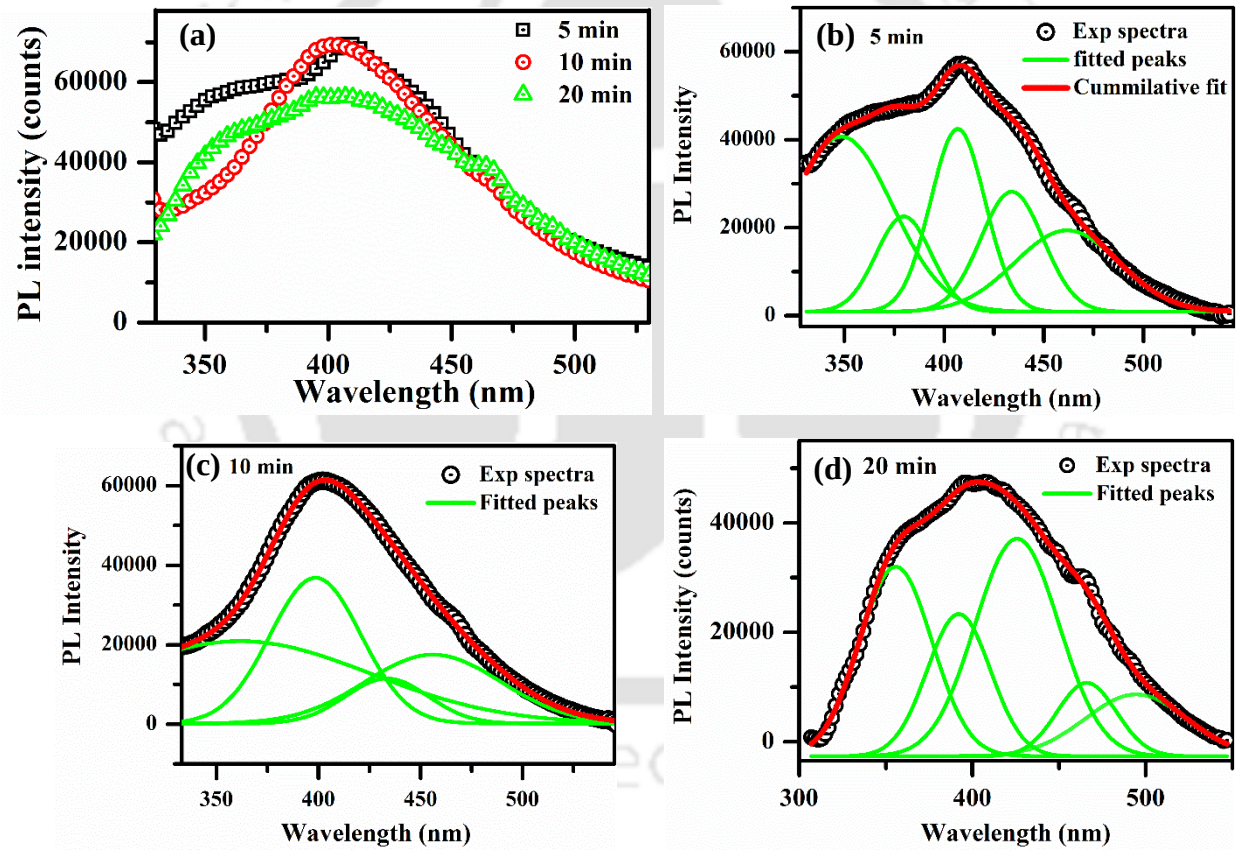

Figure 6.11 The plot of (a) PL spectra of the MoS_2 QDs dispersed in DW synthesized at various ablation time at the fixed laser energy of 40 mJ. Lorentzian fittings of the PL spectra at ablation times of (b) 5, (c) 10 and (d) 20 min.

MoS_2 QDs were also synthesized at the ablation times of 20,10 and 5 min at the fixed laser energy of 10 mJ to verify the effect of ablation time at comparatively lower laser energy.

Figure 6.12 (a) shows the PL spectra of the MoS_2 QDs dispersed in DW synthesized at various ablation times of 5, 10 and 20 min at a fixed laser energy of 10 mJ. The intensity of the PL spectra increased with an increase in the ablation time. Hence the high ablation time produced more QDs and the high density of QDs caused intense PL emission. Further, excitation wavelength-dependent PL emission was studied for MoS_2 QDs synthesized with 10 mJ laser energy for 20 min ablation time as shown in fig. 6.12 (b). The normalize PL spectra showed PL peak position shifted towards higher wavelength from 416 to 448 nm with an increment in excitation wavelength from 290 to 390 nm by an interval of 20 nm i.e. the emission of fluorescence color of the solution could be tuned by changing the excitation wavelength only. The FWHM of PL peak decreased gradually with an increase in excitation wavelength. Hence at lower excitation wavelength almost all the widely distributed QDs had sufficient energy to be excited to higher state while with an increase in excitation wavelength only QDs of larger size were excited to higher state, as a result, the FWHM of the PL peak reduced at higher excitation wavelength. Similar excitation dependent luminescence properties were also observed in MoS_2 QDs [35,75] and graphene oxide (GO) QDs [200-202] synthesized by various techniques.

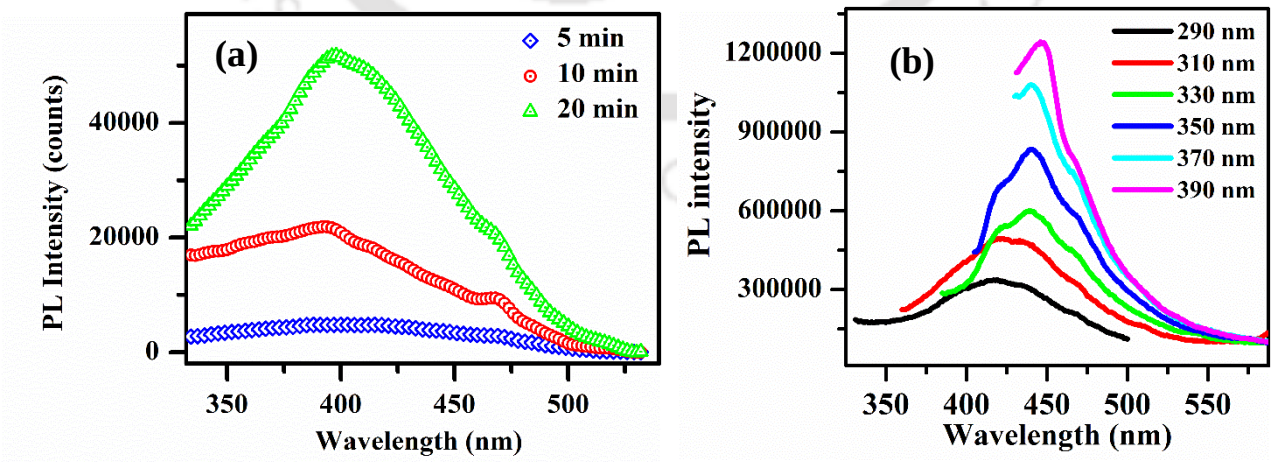

Figure 6.12 The plot of (a) PL spectra of the MoS_2 QDs dispersed in DW synthesized at various ablation time at the fixed laser energy of 10 mJ and (b) Excitation dependent luminescence spectra of MoS_2 QDs of ablation time 20 min at 10 mJ.

6.3.2 Laser ablation at various laser energy

Like ablation time, the ablation laser energy also greatly affects the QDs size and the rate of production. Hence the effects of laser energy were realized by ablating solid MoS_2 target dispersed in DW at various laser energy of 10, 20 and 40 mJ at the fixed ablation time of 5 min as shown in fig. 6.13. Ablation time was fixed for 5 min to avoid various secondary effects like laser interaction with initially generated QDs, QDs agglomerations, etc. which indirectly affects the shape and size of the QDs. The intensity of the PL spectra increased with an increase in the ablation energy from 10 to 40 mJ. This enhancement in PL intensity is associated with the high QDs density of the sample prepared at higher laser energy. In particular, at 40 mJ, the high laser energy caused high rate of ablation and produced large number of QDs compared to the ablation at other low energies.

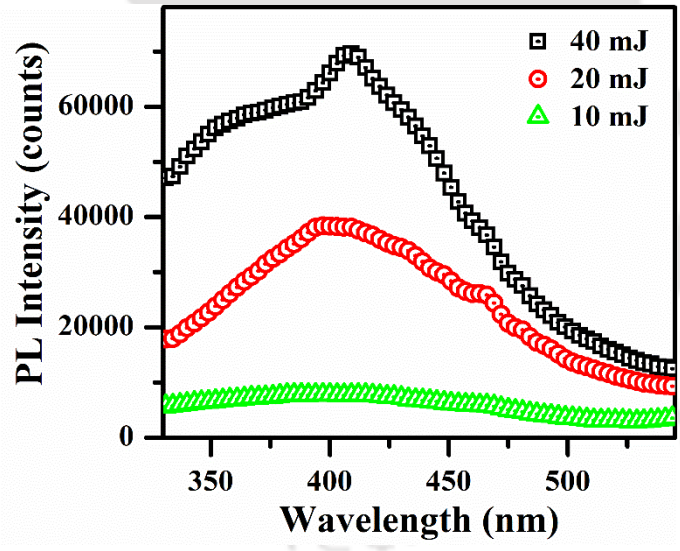

Figure 6.13 PL spectra of the MoS_2 QDs dispersed in DW water synthesized at various laser energy at a fixed ablation time of 5 min.

To verify the effect of laser energy on QDs size, TEM images of MoS_2 QDs, synthesize at various laser energy, were recorded. Figures 6.14 (a), (b) and (c) shows the TEM images of the MoS_2 QDs synthesized at the ablation laser energy of 10, 20 and 40 mJ, respectively. The size distribution of the *as*-synthesized QDs is also shown, where the average QDs sizes were

2.62, 3.57 and 4.0 nm at the laser energy of 10, 20 and 40 mJ, respectively. Therefore, with an increase in laser energy, the average QDs size also increased. Stefan et al. also observed an increase in silver nanoparticles size with an increase in laser fluence [203].

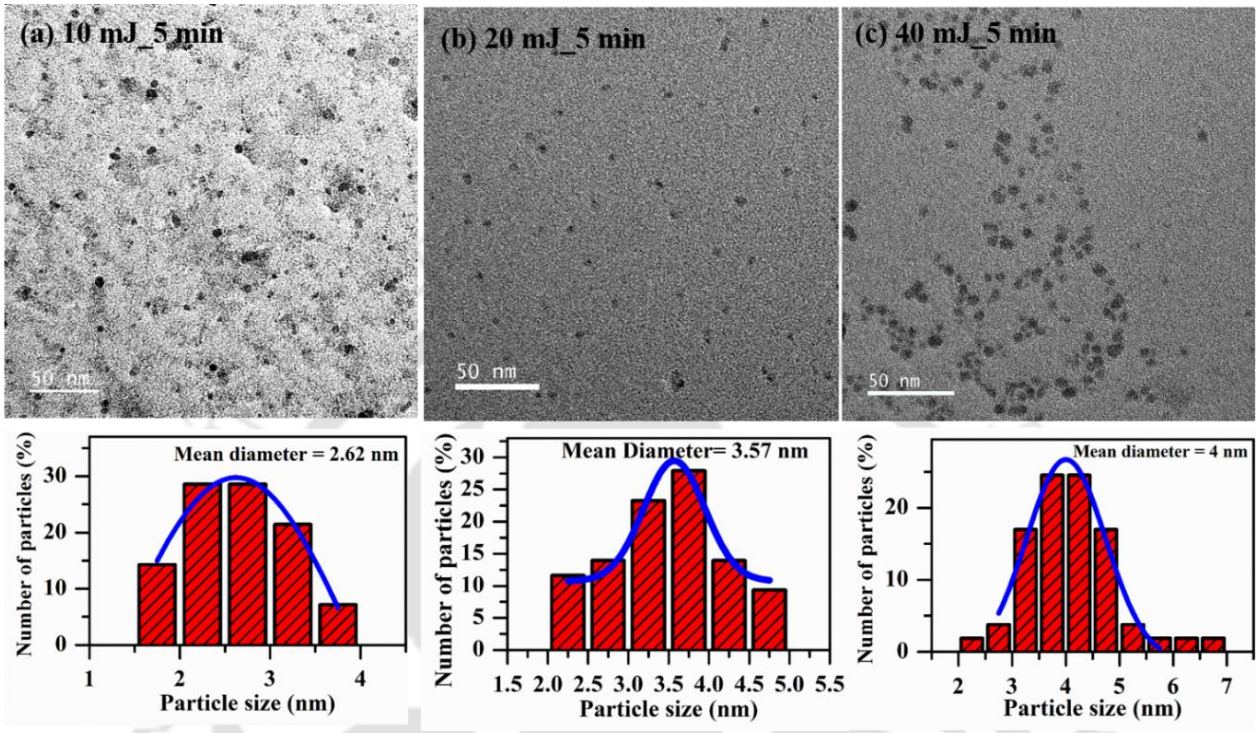

Figure 6.14 TEM images of MoS_2 QDs and their size distribution synthesized at the ablation laser energy of (a) 10, (b) 20 and (c) 40 mJ at a fixed ablation time of 5 min.

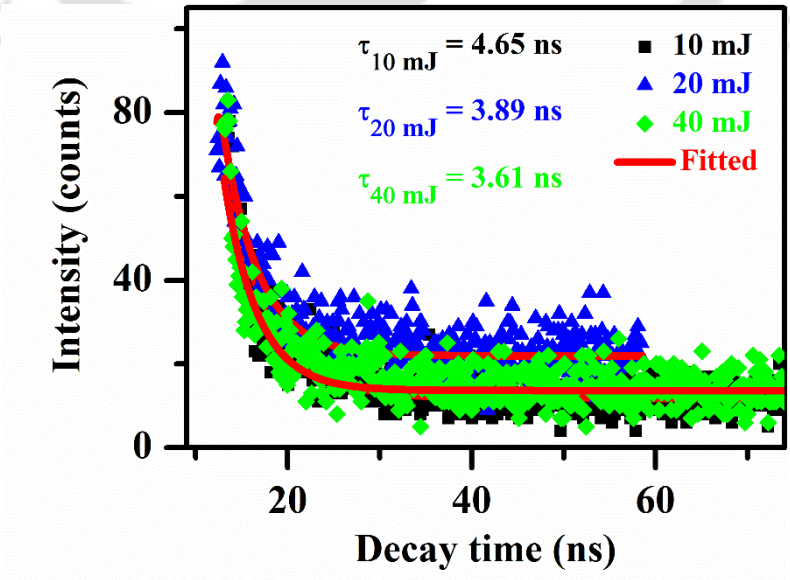

Figure 6.15 TRPL spectra with zero IRF background of the MoS_2 QDs synthesized for different laser ablation energy at fixed ablation time of 5 min.

Further, the carrier lifetime of the QDs solutions was estimated by fitting the TRPL spectra with a single exponential decay equation (equation 6.1). The carrier lifetime of the QDs synthesized at 10, 20 and 40 mJ were 4.7, 4 and 3.6 nanosecond, respectively. Correlating with the average particle size distribution as shown in fig. 6.15, it is observed that with decreasing particle size, the radiative lifetime became progressively longer which is in accordance with the earlier results as observed in MoS_2 QDs.

6.4 WS_2 QDs synthesis by PLAL

PLAL experiment was also performed to synthesis WS_2 QDs at various laser energy of 10, 20 and 40 mJ at the fixed ablation time of 5 min. Figure 6.16 shows the Raman spectra of the WS_2 QDs at ablation laser energy of 10, 20, and 40 mJ. These spectra contain first-order Raman modes at the Brillouin zone center ($E^1_{2g}(\Gamma)$ and A_{1g} (Γ)).[98]. The $A_{1g}(\Gamma)$ mode frequencies were observed at 424.07, 421.72, and 419.21 cm^{-1} while that of $E^1_{2g}(\Gamma)$ modes were observed at 359.33, 357.00, and 353.23 cm^{-1}, for the QDs samples synthesized at an ablation laser energy of 10, 20, and 40 mJ, respectively. The peak position differences of the two Raman modes were ~ 64.74, 64.72 and 65.97 cm^{-1}, indicating multilayered like WS_2 structure formation [96].

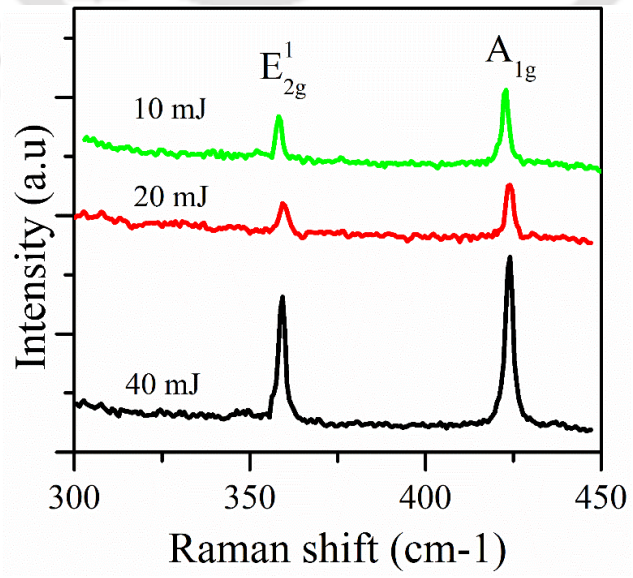

Figure 6.16 Raman spectra of the WS_2 QDs synthesized at various ablation times.

To study the effect of laser energy on QDs size, TEM images of MoS_2 QDs, synthesize at various laser energy, were recorded. Figures 6.17 (a), (b) and (c) show the TEM images of the MoS_2 QDs synthesized at the ablation laser energy of 10, 20 and 40 mJ, respectively. The size distribution of the *as*-synthesized QDs is also shown, where the average QDs sizes were 3.02, 6.19 and 8.28 nm at the laser energy of 10, 20 and 40 mJ, respectively. Therefore, with an increase in laser energy, the average QDs size also increased. Similar result was also observed in the case of MoS_2 QDs synthesized at various laser energies.

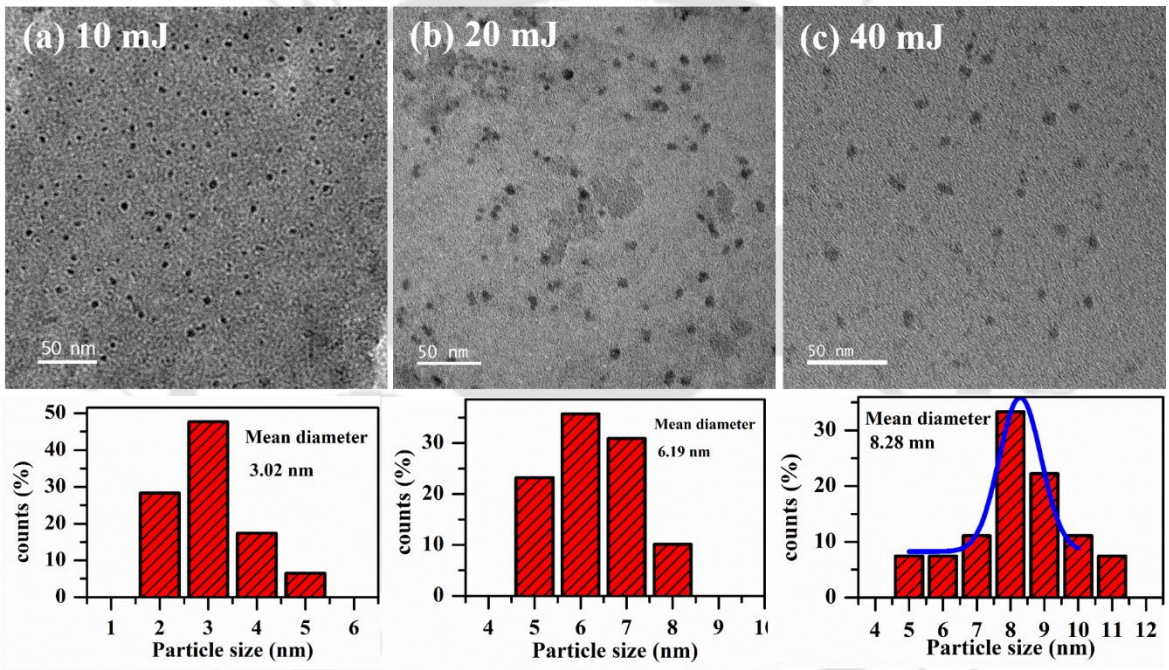

Figure 6.17 TEM images of WS_2 QDs and their size distribution, synthesized by the ablation laser energy of (a) 10, (b) 20 and (c) 40 mJ at a fixed ablation time of 5 min.

Figure 6.18 shows the intensity of the PL spectra of the QDs solutions. The PL peak intensity increased with the increase in ablation energy from 10 to 40 mJ. This enhancement in PL intensity is associated with the high QDs density of the sample prepared at higher laser energy. In particular, at 40 mJ, the high laser energy caused high rate of ablation and produce large number of QDs compared to other low energy laser ablation. A similar result was also observed in MoS_2 QDs.

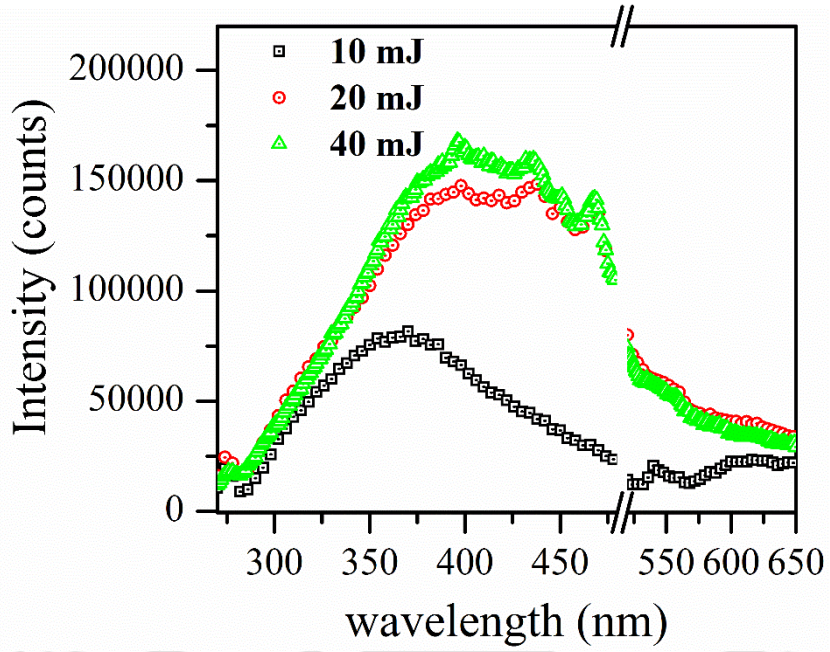

Figure 6.18 PL spectra of the MoS_2 QDs dispersed in DW water synthesized at various laser energy at a fixed ablation time of 5 min.

MoS_2 and WS_2 QDs synthesized by PLAL technique showed high luminescence with an excellent chemical and thermal stability. The ablation parameters like laser energy, ablation times show its effectiveness in controlling the QDs size. In the present work, the nanosecond laser-ablated QDs sizes were 2-8 nm which are little bit larger with wide size distribution compared to the reported femtosecond laser ablated QDs having sizes 1-5 nm [77]. MoS_2 QDs are also successively applied in biological and deep-tissue imaging due to its low toxicity with efficient fluorescence ability [204]. Hence, PLAL technique seems to be a good alternative technique to synthesize MoS_2 QDs and as synthesis MoS_2 quantum dots (QDs) can be effectively used for gas sensing, electrochemical lithium storage, bio-imaging, etc. High surface area with more active edge makes the QDs an active catalyst for hydrogen evolution reaction (HER) [205]. As an application, a detailed study on effectiveness of the MoS_2 and WS_2 QDs as a catalyst for HER has been performed and discussed in chapter 7.

6.5 Conclusion

PLAL technique shows promise as a fast, green, and simple method to prepare high-purity, dense, MoS_2 and WS_2 QDs with wide size distribution. Laser ablation of solid MoS_2 targets produced MoS_2 QDs along with MoS_2 nano-sheets and nano-particle where a QDs only solution was extracted by two post ablation processes called ultrasonication and centrifugation. TEM analysis showed that the majority of the as-prepared MoS_2 QDs were in the range of 2–8.5 nm which is well within the excitonic Bohr radius of MoS_2. All the PL spectra showed a broadening from 310 to 550 nm, due to the distribution in QDs size, were deconvoluted into 4-5 peaks by fitting with a Lorentzian function. Both, with an increase in laser energy and ablation time, PL peak intensity increased. With decreasing QDs size, the radiative lifetime became progressively longer. Highly pure MoS_2 quantum dots (QDs) of average sizes 4, 2.91 and 6.13 nm were obtained by applying a fixed laser energy of 40 mJ for ablation times of 5, 10 and 20 min while at the fixed ablation time of 5 min the average QDs size were 2.91, 3.57 and 4 nm at the laser energy of 10, 20 and 40 mJ, respectively. In the case of WS_2, the average QDs sizes were 3.02, 6.19 and 8.28 nm at the laser energy of 10, 20 and 40 mJ, respectively. The WS_2 QDs, synthesized at the same ablation conditions, were comparatively larger than MoS_2 QDs. The MoS_2 QDs solution showed excitation-dependent luminescence emission which shifted to longer wavelength with an increment in excitation wavelength from 290 to 390 nm. EDX, SAED pattern, and zeta potential analysis showed the formation of stoichiometric, highly crystalline, stable MoS_2 QDs. The two Raman active modes of MoS_2 crystal known as A_{1g} and E^1_{2g} were detected in Raman spectroscopy of the QDs. The following work can be extended to other transitional metal dichalcogenides to effectively synthesis their QDs counterpart.

भारतीय प्रौद्योगिकी संस्थान गुवाहाटी
Indian Institute of Technology Guwahati

Chapter 7

MoS_2 and WS_2 thin films and quantum dots as a catalyst for hydrogen evolution reaction

7.1 Introduction

In the present century, the demand for energy is increasing day by day. Today fossil fuels are mostly fulfilling the required energy. We know that the storage of nonrenewable energy will be exhausted in the near future. The excessive use of fossil fuels also causes serious environmental pollution. All these situations stimulated to exploit some alternative green energy sources. Nowadays, renewable energy sources like solar energy, wind energy, and hydropower are partially fulfilling global power demand although they are insufficient. In another option, hydrogen has the potential to substitute fossil fuels as an alternative green and clean energy source. Unlike other energy sources, hydrogen is not available naturally. For large scale uses of hydrogen, it must be synthesized by various routes. There are various techniques to synthesize hydrogen. In thrombolysis method hydrogen gas is produced from water dissociation by high-temperature treatment. Today ~95% hydrogen is produced by thermal energy treatment [206,207]. Meanwhile, electrochemical, photolysis and biochemical processes are being used to synthesize hydrogen by decomposing water into hydrogen and oxygen [207,208]. Among them, water electrolysis can be an effective technique for large scale hydrogen production. The main disadvantage of this technique is its high-cost production. Particularly, today Pt-group noble metals are the most efficient hydrogen evolution catalyst, but their high cost and low availability limits the large scale production of hydrogen. Hence, alternative cost-effective, highly stable and efficient catalysts for HER have great importance.

Recently, MoS_2 and WS_2 nanostructures and QDs have shown immense possibility as hydrogen evolution catalyst [36-40]. An increase in effective surface area and the presence of a large number of active sites at the edges of the nanostructure increases the HER activity compared to their bulk structure. The high conductivity of metallic 1T phase of MoS_2 and WS_2 is very useful as an efficient HER catalyst. The catalytic activity of the 2D materials nanostructures can be further increased by modifying their chemical structure, inducing defect and creating strain and doping of external transition metals i.e. Co, Ni, etc.

In the earlier chapters, MoS_2 and WS_2 thin films of various thicknesses were deposited and MoS_2 QDs of different sizes were synthesized. In the present work, as an application, the MoS_2 and WS_2 films of various thicknesses are used as a catalyst for HER. Furthermore, we have performed HER by using MoS_2 QDs drop-casted onto glassy carbon electrode (GCE) as a working electrode to verify their effectiveness as an active electrocatalyst for HER.

7.2 Experimental details

The hydrogen evolution reaction (HER) experiment was performed for the effectiveness of the MoS_2 thin films and QDs as an active electrocatalyst. MoS_2 films were deposited onto FTO substrate heated to 500 ℃ under vacuum ($\sim 5 \times 10^{-6}$ mbar) for the time duration of 1, 5, and 15 minutes. WS_2 films were also deposited onto FTO substrate under similar conditions as that of MoS_2. The substrate, heated to 500 ℃, was kept 5 cm apart perpendicular to the target. Along with MoS_2 and WS_2 thin films, a MoS_2/WS_2 heterostructure thin film was also deposited onto the FTO substrate. In MoS_2/WS_2 heterostructure film, MoS_2 film (thickness ~ 34 nm) was first deposited onto the FTO substrate for 7.5 min and immediately WS_2 layer (thickness ~ 27 nm) was deposited onto pre-deposited MoS_2 thin film for another 7.5 min. During the experiment, other deposition parameters were the same as in the case of the MoS_2 and WS_2 films. MoS_2 QDs were synthesized for the ablation time of 5,

10 and 20 min. The QDs solutions were drop-casted onto GCE and allowed to dry onto the electrode at room temperature. During the HER experiment, MoS_2 and WS_2 thin films deposited onto FTO substrate and MoS_2 QDs drop-casted onto GCE were used as working electrodes (WE). More details on HER experiment setup were discussed in chapter 2, section 2.7.

7.3 HER activity of MoS_2 and WS_2 thin films

For HER electrocatalysis, onset potential, overpotential and Tafel slope are the three important parameters to determine the efficiency of the electrode material. Lower the value of the parameters better the performance of the electrodes. Onset potential represents the minimum potential required to start the current flow (generally @ -1 mA/cm^2) through the electrode. The potential required to achieve a current density of @-10 mA/cm^2 is considered as the over potential of the HER experiment. This current density is an important parameter for solar energy to hydrogen generation devices. At this current density the solar energy to water splitting device efficiency is approximately 12.3%. Tafel slope is the linear part of the Tafel plot (Tafel equation $\eta = a \log|j| + c$, where a is the Tafel slope and j is the current density). The lower value of Tafel slope represents high rate of hydrogen production. In the electrocatalysis process, the Potential Vs current density plot is called polarization curve where the term 'polarization' means that electrolysis causes the elements in an electrolyte to be attracted to anode or cathode i.e. the electrolyte components are polarized towards the electrodes. Figure 7.1 (a) shows the polarization curve of MoS_2 and WS_2 and MoS_2/WS_2 thin films. All the films showed low onset potential (@-1 mV/cm^2) compared to their bulk counterparts. The over potential (@-10 mV/cm^2) significantly reduces from bulk material to the thin film samples. Figure 7.1 (b) shows the Tafel plots of the samples, derived from the polarization curves. Tafel slope of the films were in the range of 83- 108 mV/dec in which few-

layered MoS_2 films showed the least value and multilayered WS_2 film showed the highest value.

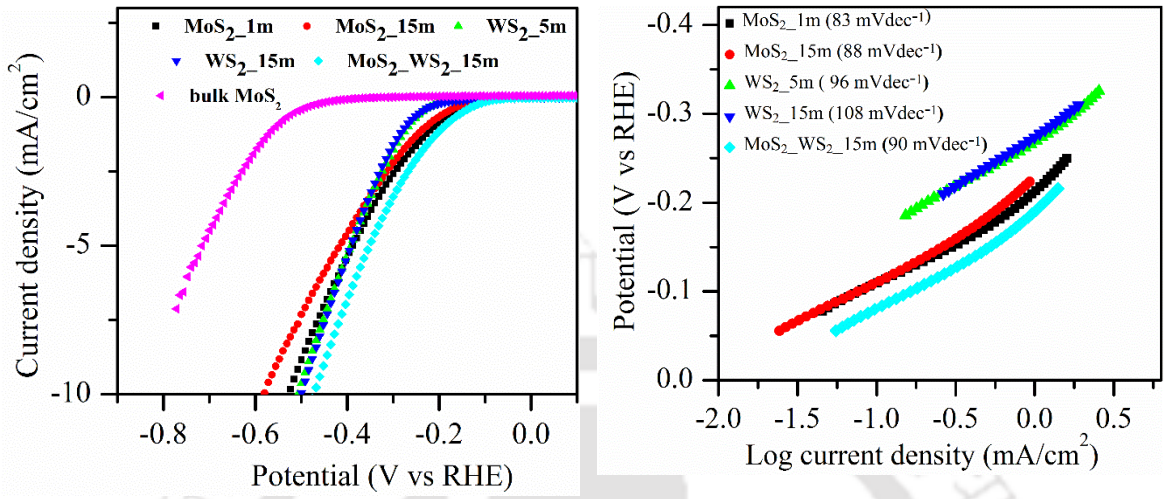

Figure 7.1 (a) Polarization curve of MoS_2 and WS_2 thin films at various deposition times and (b) Corresponding Tafel plots derived from the polarization curves of the thin films.

The superior HER activity of the MoS_2 and WS_2 thin films compared to their bulk counterpart is due to the presence of S deficiency, higher surface to volume ratio, and large number of active edge sites in thin films as compared to the bulk structure. The values of the onset potential, overpotential and Tafel slope of the samples are presented in Table 7.1.

Table 7.1 Onset potential, overpotential and Tafel slope of the MoS_2, WS_2 and their heterostructure films deposited onto FTO at various deposition time.

Thin films	**Onset potential (mV) @ -1 mA/cm^2**	**Overpotential (mV) @-10 mA/cm^2**	**Tafel slope (mV/decade)**
MoS_2_1m	211	527	83
MoS_2_15m	225	580	88
WS_2_5m	267	508	96
WS_2_15m	271	501	108
MoS_2_WS_2_15m	189	472	90

7.4 HER activity of MoS_2 QDs

Like MoS_2 thin films, their QDs structure also possess a high spatial surface area which offers more active edge sites for the HER. The electrocatalytic activity of the MoS_2 QDs for HER was investigated systematically. The QDs solutions were drop-casted onto GCE and dried at room temperature and were used as working electrode. N_2 saturated 0.5 H_2SO_4 solution was prepared as the electrolytic solution. All the measurements were performed using linear sweep voltammetry (LSV) in a typical three-electrode configuration. During the experiment, Ag/AgCl electrode was used as the reference electrode and Pt wire was used as the counter electrode. Figure 7.2 (a) shows the polarization curves of GCE and QDs samples. An increase in the current density was observed in all the QDs samples compared to the standard GCE.

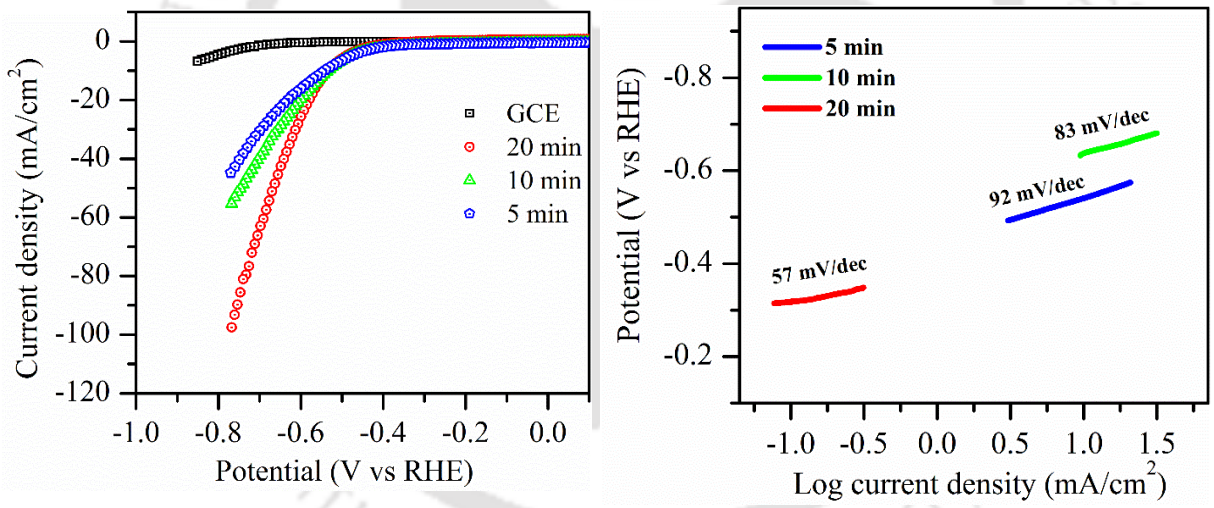

Figure 7.2 (a) Polarization curve of QDs solutions at various ablation times and (b) Corresponding Tafel plots derived from the polarization curves of the QDs solutions.

The value of the onset potential, overpotential and Tafel slope of the QDs samples are presented in Table 7.2. The overpotential @10mA/cm^2 current density was 0.529, 0.536 and 0.534 V for the MoS_2 QDs, synthesized for 20, 10 and 5 min ablation time. Figure 7.2 (b) shows the Tafel slope of the QDs samples. Tafel slope of the QDs at ablation time of 20, 10 and 5 min was 57, 83 and 92 mV/dec.

Table 7.2 Onset potential, over potential and Tafel slope of the MoS_2 QDs synthesized at various ablation times.

MoS_2 QDs Samples	**Onset potential (mV) @ -1 mA/cm^2**	**Over potential (mV) @-10 mA/cm^2**	**Tafel slope (mV/decade)**
20_min	279	529	57
10_min	264	538	83
5_min	295	547	92

These results show better efficiency than several reports on HER effects in pulsed laser deposited 2D materials [100,209]. As observed earlier (in chapter 3) the presence of metallic 1T phase increases the conductivity of the films and S deficiency in the films causes large numbers of active edge sites. Both of these helps in enhance the HER potentials of the PLD films. Hence, amongst all the samples, QDs synthesized for 20 min ablation time were most effective as the electrocatalyst for HER. For 20 min, the longer ablation time generated high density of QDs in the solution. During drop-cast, the high density sample mostly covered the top surface of GCE which provided a more effective surface area for HER in compared to other samples. The large effective area caused high rate of HER. Hence, comparing the efficacy of thin film and QDs samples as a catalyst for HER, the thin films showed low onset profile while the Tafel slope is lower in the case of QDs samples. There are various reports on the synthesis of various kinds of MoS_2 nanostructures for HER catalytic enhancement. The catalytic performances of various MoS_2 nanostructures in terms of various catalytic parameters are summarized in table 7.3. From the table it is observed that the PLD and PLAL synthesis MoS_2 thin films and QDs required higher turned-on potential for HER compared to the other reported MoS_2 nanostructures. But it is interesting that the Tafel slope of the samples of the present work were lower compared to the reported one i.e. after starting the reaction these samples produced hydrogen at higher rates.

Table 7.3 Summary of the electrocatalytic performances of various MoS_2 nanostructures.

MoS_2 nano structure	**Synthesis technique**	**Onset potential (mV) @-1 mA/cm^2**	**Over potential (mV) @ -10mA/cm^2**	**Tafel slope (mV/dec)**	**Ref.**
MoS_2 thin film	PLD	189	472	90	This work
MoS_2 QDs	PLAL	279	529	57	This work
Co-doped MoS_2 nanoparticle	Theoretical simulation	-	400	101	210
Monolayer MoS_2	CVD	100	210	61	211
Strained MoS_2 with S-vacancies	CVD and Ar plasma treatment	-	170	60	212
MoS_2 nanoparticles	Ultrasonication and centrifugation	90	220	69	40
Vertical MoS_2 nanosheets on Graphene	CVD	188	421	84	213
Layered MoS_2 on graphene	CVD	310	590	104	213
O_2 plasma treated MoS_2	O_2 plasma treatment	-	350	105	214

7.5 Conclusion

As an application, the PLD MoS_2 and WS_2 thin films and PLAL synthesized QDs samples were successfully used as HER catalyst. The as-fabricated thin films and QDs samples showed superior HER activity compared to their bulk counterparts. MoS_2 and WS_2 thin film samples showed very low onset potential while QDs samples possessed small Tafel slopes. The high HER activity of MoS_2 thin films and QDs is attributed to the large spatial surface area and large active edge sites. Overall, the PLD and PLAL seem to be an effective technique to synthesize 2D material nanostructures as an efficient HER catalyst.

Chapter 8

Conclusions

In the present thesis, growth of monolayer to multilayer MoS_2 and WS_2 film were studied on various substrates like SiO_2/Si, Corning glass, Si by varying the deposition time, laser fluence, substrate temperature in PLD. 2H-1T mixed-phase mono and few-layered MoS_2 films were obtained by PLD in a very short time span of only 20 sec at various deposition temperatures. The tunability of the ratio of the two phases with deposition temperature as well as deposition time were investigated extensively. The surface morphology evolution of MoS_2 and WS_2 thin films from a few layered to bulk like structure, grown by the PLD technique, was studied based on generic scaling theory using AFM images of the films. A detail study on structural and linear and nonlinear optical characteristics of the MoS_2 and WS_2 films was performed. Along with layered thin films, MoS_2 and WS_2 QDs of various sizes were also synthesized by tuning the nanosecond pulsed laser fluence and ablation time. Further, the MoS_2 and WS_2 thin films and QDs were efficiently used as a catalyst for hydrogen evolution reaction (HER).

For depositing MoS_2 and WS_2 thin films, sintered MoS_2 and WS_2 pellets were prepared from highly pure MoS_2 and WS_2 powder. The sintered pellets were used as the target in be employed PLD system. A high power Nd: YAG laser was focused on the MoS_2 target. Experiments were performed at various optimized conditions like deposition times, Ar gas pressures, substrate temperatures and laser fluences to synthesis films of desired properties. The crystallinity of the deposited films was analyzed by recording X-ray diffraction pattern at 3 degrees/min scanning speed with a step size of 0.03°. Raman and photoluminescence spectra were recorded in the backscattering geometry using an excitation wavelength of 488 nm. The exciting laser was focused onto the sample with the 100X objective lens. Atomic force

microscope was used in the non-contact mode to image the surface morphology. Transmission electron microscopy was performed to analyze the particle size and crystallinity of the deposited films and QDs. The SE measurements were carried out over the spectral range of 1.32–3.50 eV using Variable Angle Spectroscopic Ellipsometer (*Semilab SOPRA: GES-5E*) equipped with goniometer at incident angles of 65°, 70°, and 75°. The nonlinear optical behavior of the films was studied using *Z*-scan setup. He-Ne laser of wavelength 632.8 nm was used as the laser source which was focused onto the film surface using a bi-convex lens of focal length of 5 cm.

Mono- and a few layered MoS_2 films were deposited on SiO_2/Si substrate (300 nm/0.38 mm) using PLD technique. The layered numbers were controlled by applying different number of laser pulses. Raman spectroscopy and AFM height profile were used to determine MoS_2 layered structure. The *as*-grown films show highly crystalline (002) plane oriented epitaxial growth. The deposited MoS_2 films showed an epitaxial compression due to its adhesion to the substrate. XRD and Raman analysis confirmed that crystalline properties of deposited MoS_2 films reduce with an increase in the number of monolayers. The two Raman active modes $A_{1g}$and E_{2g}^1 of the layered MoS_2 films showed strain-induced blue-shifted spectra. TEM measurement demonstrated layered MoS_2 film formation. Similar experiment was also performed to synthesize monolayer to multilayered WS_2 thin films where the laser fluence was varied and other deposition parameters were kept constant.

An efficient way to deposit 1T/2H mixed-phase mono and a few layered MoS_2 thin films for a very short span of time of 20 sec was realized by pulsed laser deposition. The 1T/2H phase ratio in monolayer to a few layered MoS_2 films was modulated by altering the substrate temperature. Irrespective of deposition temperature all the films showed a mixed-phase structure while the 2H to 1T phase ratio increased from 66 to 84% with an increase in deposition temperature from 400 to 720 °C. The presence of 1T-2H mixed-phase MoS_2 layers

was confirmed and their structural and optical properties were analyzed in nano (TEM), micro (Raman, AFM) and macro (ellipsometer) scale. The ellipsometer analysis demonstrated the two excitonic absorption peaks, denoted as *A*/*B* and *C*/*D*, corresponding to 2H phase while the presence of 1T phase caused excess semimetal like charge density of the order of ~10^{20} cm^{-3}. Hence, stable 1T/2H mixed phase MoS_2 films, strongly adhered to the substrate were obtained in a single step bottom-up growth process. The highly crystalline 1T Phase MoS_2 films could be used as an efficient electrocatalyst.

An experimental investigation was carried out to identify the scaling behavior as well as growth mechanism of 2D MoS_2 thin films, grown on glass substrates by PLD at different deposition time durations, using atomic force microscopy images. Growth dynamics of thin films expressed by scaling theory is a useful tool to quantify statistical properties of surface morphology of the thin films. The growth of MoS_2 films evolved from layer-by-layer to layer plus island with the increase in deposition time from 20 sec to 15 min. The film surface exhibited anisotropic growth dynamics in vertical and lateral direction where RMS roughness varied with deposition time as, $w \sim t^{\beta}$ with growth exponent, $\beta = 0.85 \pm 0.11$ while lateral correlation length ξ, as $\xi = t^{1/z}$ with dynamic scaling exponent, $1/z = 0.49 \pm 0.09$. The films showed local roughness exponent $\alpha_{loc} = 0.89 \pm 0.01$, global roughness exponent $\alpha = 1.72 \pm 0.14$ and spectral roughness exponent, $\alpha_s = 0.85 \pm 0.03$, suggesting the growth of MoS_2 thin films followed intrinsic anomalous scaling behavior ($\alpha_s < 1$, $\alpha_{loc} = \alpha_s \neq \alpha$). Shadowing owing to conical incoming particle flux distribution towards substrate during deposition has been attributed to the anomalous growth mode. Optical properties of the films, extracted from ellipsometric analysis, were also correlated with RMS roughness and cluster size variation which unveiled the important role played by surface roughness and film density. Similar work extended to WS_2 films deposited onto corning glass and SiO_2/Si substrate as well.

Multilayered-to-bulk like MoS_2 and WS_2 films were deposited by pulsed laser deposition at various argon gas deposition pressure. A significantly large reverse saturation absorption and positive nonlinear refraction response were observed in all the films, as measured by the open and closed aperture *Z*-scan experiment under He-Ne laser at 632.8 nm. In addition, third-order non-linear optical susceptibility of the thin films was found to be of the order of 10^{-2} esu as measured from *Z*-scan experiment. The anomalously high nonlinear optical response of the film was attributed to the continuous-wave laser-induced thermal nonlinearity dominance over optical nonlinearity. Optical limiting was also observed in the WS_2 thin films where optical limiting thresholds were found to increase with increasing nonlinear absorption coefficient.

MoS_2 QDs were synthesized efficiently by multilevel photo-exfoliation of solid MoS_2 target using pulsed laser ablation in distilled water. It is a single step, chemical-free simple physical process. Highly pure MoS_2 quantum dots (QDs) of average sizes 4, 2.91 and 6.13 nm were obtained by applying a fixed laser energy of 40 mJ at ablation time of 5, 10 and 20 min while for the fixed ablation time of 5 min the average QDs size were 2.91, 3.57 and 4 nm at the laser energy of 10, 20 and 40 mJ, respectively. The wide size distribution of the QDs resulted in a broad luminescence in the visible region. The MoS_2 QDs solution showed excitation-dependent luminescence emission which shifted to longer wavelength by varying the excitation wavelength from 290 to 390 nm. EDX, XRD and SAED pattern, zeta potential analysis demonstrated the formation of stoichiometric, highly crystalline, stable MoS_2 QDs. In Raman spectroscopy, the peaks corresponding to the A_{1g} and E^1_{2g} phonon modes of MoS_2 were clearly observed, indicating crystalline MoS_2 QDs formation. The colloidal MoS_2 QDs solution showed an absorption edge ~ 310 nm. The blue-shift in optical absorption of the as-prepared MoS_2 QDs was attributed to the quantum confinement. The following work can be extended to other transitional metal dichalcogenides to effectively synthesis their QDs counterpart.

As an application, MoS_2 and WS_2 films of various thicknesses deposited onto the FTO substrate and MoS_2 QDs drop casted onto GCE were used as an active electrocatalyst for HER. The overpotential @-10mA/cm^2 current density was 0.472 -0.580 V, and Tafel slope in between 83-108 mV/decade for various MoS_2 and WS_2 films. The overpotential @-10mA/cm^2 current density was 0.529, 0.536 and 0.534 V for the MoS_2 QDs, synthesized at 20, 10 and 5 min ablation time. Tafel slope of the QDs at ablation time of 20, 10 and 5 min were 57, 83 and 92 mV/dec. These results suggest an excellent efficiency of the thin films and QDs as HER catalyst.

Future scope of the work

In the present work monolayer to multilayered MoS_2 and WS_2 films were deposited by PLD technique and their optical properties are investigated extensively. Like optical characterizations, a details characterization on electrical behavior can also be done of the following MoS_2 and WS_2 thin films. Hence 2D materials hetero-junction synthesis by PLD and their structural characterization and device applications can be undertaken in the future. In the present work, 2D materials QDs solution synthesized by PLAL showed intense PL spectra. They can be used for sensing by PL quenching or enhancement. New physical properties and probable applications can be explored by structure engineering at atomic level of the 2D materials. The hybrid structure of direct band semiconductor (ZnO, TiO_2, ZnS, etc.) and 2D materials (MoS_2, WS_2, CdSe, CdS, etc.) can be deposited by PLD technique and they can be employed in sensing, catalytic applications. The HER catalytic efficiency of the MoS_2 and WS_2 films can be further enhanced by doping of external transition metals.

Bibliography

1 Novoselov, K. S. *et al.* Electric field effect in atomically thin carbon films. *Science* **306**, 666-669 (2004).

2 Gan, X. *et al.* Chip-integrated ultrafast graphene photodetector with high responsivity. *Nat. Photonics* **7**, 883-887 (2013).

3 Yavari, F. & Koratkar, N. Graphene-based chemical sensors. *J. Phys. Chem. Lett.* **3**, 1746-1753 (2012).

4 Shelke, N. T. & Karche, B. Ultraviolet photosensor based on few layered reduced graphene oxide nanosheets. *Appl. Surf. Sci.* **418**, 374-379 (2017).

5 Ye, M., *et al. Photonics.* 288-307 (Multidisciplinary Digital Publishing Institute).

6 Song, X., Hu, J. & Zeng, H. Two-dimensional semiconductors: recent progress and future perspectives. *J. Mater. Chem. C* **1**, 2952-2969 (2013).

7 Wang, Q. H., *et al.*Electronics and optoelectronics of two-dimensional transition metal dichalcogenides. *Nat. Nanotechnol.* **7**, 699-712 (2012).

8 Xu, M., Liang, T., Shi, M. & Chen, H. Graphene-like two-dimensional materials. *Chem. Rev.* **113**, 3766-3798 (2013).

9 Mak, K. F., *et al.* Atomically thin MoS_2: a new direct-gap semiconductor. *Phys. Rev. Lett.* **105**, 136805 (2010).

10 Splendiani, A. *et al.* Emerging photoluminescence in monolayer MoS_2. *Nano Lett.* **10**, 1271-1275 (2010).

11 Song, I., Park, C. & Choi, H. C. Synthesis and properties of molybdenum disulphide: from bulk to atomic layers. *RSC Adv.* **5**, 7495-7514 (2015).

12 Yoon, Y., Ganapathi, K. & Salahuddin, S. How good can monolayer MoS_2 transistors be? *Nano Lett.* **11**, 3768-3773 (2011).

13 Liu, L., Kumar, S. B., *et al.* Performance limits of monolayer transition metal dichalcogenide transistors. *IEEE Trans. Electron Devices* **58**, 3042-3047 (2011).

14 Radisavljevic, B., *et al.* A. Single-layer MoS_2 transistors. *Nat. Nanotechnol.* **6**, 147-150 (2011).

15 Zhang, Y., *et al.* Ambipolar MoS_2 thin flake transistors. *Nano Lett.* **12**, 1136-1140 (2012).

16 Qiu, H. *et al.* Electrical characterization of back-gated bi-layer MoS_2 field-effect transistors and the effect of ambient on their performances. *Appl. Phys. Lett.* **100**, 123104 (2012).

17 Yin, Z. *et al.* Single-layer MoS_2 phototransistors. *ACS Nano* **6**, 74-80 (2011).

18 Wang, H. *et al.* Integrated circuits based on bilayer MoS_2 transistors. *Nano Lett.* **12**, 4674-4680 (2012).

19 Deng, J. *et al.* High-performance hydrogen evolution electrocatalysis by layer-controlled MoS_2 nanosheets. *RSC Adv.* **4**, 34733-34738 (2014).

20 He, M. *et al.* Enhanced hydrogen evolution reaction activity of hydrogen-annealed vertical MoS_2 nanosheets. *RSC Adv.* **8**, 14369-14376 (2018).

21 Chen, X. *et al.* Preparation of a MoS_2/carbon nanotube composite as an electrode material for high-performance supercapacitors. *RSC Adv.* **8**, 29488-29494 (2018).

22 Liu, X. *et al.* High performance field-effect transistor based on multilayer tungsten disulfide. *ACS Nano* **8**, 10396-10402 (2014).

23 Elías, A. L. *et al.* Controlled synthesis and transfer of large-area WS_2 sheets: from single layer to few layers. *ACS Nano* **7**, 5235-5242 (2013).

24 Ovchinnikov, D., *et al.* Electrical transport properties of single-layer WS2. *ACS Nano* **8**, 8174-8181 (2014).

25 Iqbal, M. W. *et al.* High-mobility and air-stable single-layer WS_2 field-effect transistors sandwiched between chemical vapor deposition-grown hexagonal BN films. *Sci. Rep.* **5**, 10699 (2015).

26 Guo, H. *et al.* Transparent, flexible, and stretchable WS_2 based humidity sensors for electronic skin. *Nanoscale* **9**, 6246-6253 (2017).

27 Lan, C. *et al.* Wafer-scale synthesis of monolayer WS_2 for high-performance flexible photodetectors by enhanced chemical vapor deposition. *Nano Res.* **11**, 3371-3384 (2018).

28 Zhang, H. *et al.* Molybdenum disulfide (MoS_2) as a broadband saturable absorber for ultra-fast photonics. *Opt. Express* **22**, 7249-7260 (2014).

29 Torres-Torres, C. *et al.* Third order nonlinear optical response exhibited by mono-and few-layers of WS_2. *2D Mater.* **3**, 021005 (2016).

30 Zheng, X., *et al.* Z-scan measurement of the nonlinear refractive index of monolayer WS_2. *Opt. Express* **23**, 15616-15623 (2015).

31 Dong, N. *et al.* Dispersion of nonlinear refractive index in layered WS_2 and WSe_2 semiconductor films induced by two-photon absorption. *Opt. Lett.* **41**, 3936-3939 (2016).

32 Zhu, X. *et al.* Tunable photoluminescence of MoS_2 quantum dots passivated by different functional groups. *J. Colloid Interface Sci.* **511**, 209-214 (2018).

33 Wang, X., *et al.* One-step synthesis of water-soluble and highly fluorescent MoS_2 quantum dots for detection of hydrogen peroxide and glucose. *Sensors Actuat. B Chem.* **252**, 183-190 (2017).

34 Mukherjee, S., *et al.* Novel colloidal MoS_2 quantum dot heterojunctions on silicon platforms for multifunctional optoelectronic devices. *Sci. Rep.* **6**, 29016 (2016).

35 Lin, H. *et al.* Colloidal synthesis of MoS_2 quantum dots: size-dependent tunable photoluminescence and bioimaging. *New J. Chem.* **39**, 8492-8497 (2015).

36 Karunadasa, H. I. *et al.* A molecular MoS_2 edge site mimic for catalytic hydrogen generation. *Science* **335**, 698-702 (2012).

37 Laursen, A. B., *et al.* Molybdenum sulfides—efficient and viable materials for electro- and photoelectrocatalytic hydrogen evolution. *Energy Environ. Sci.* **5**, 5577-5591 (2012).

38 Merki, D. & Hu, X. Recent developments of molybdenum and tungsten sulfides as hydrogen evolution catalysts. *Energ. Environ. Sci.* **4**, 3878-3888 (2011).

39 Hinnemann, B. *et al.* Biomimetic hydrogen evolution: MoS_2 nanoparticles as catalyst for hydrogen evolution. *J. Am. Chem. Soc.* **127**, 5308-5309 (2005).

40 Wang, T. *et al.* Enhanced electrocatalytic activity for hydrogen evolution reaction from self-assembled monodispersed molybdenum sulfide nanoparticles on an Au electrode. *Energ. Environ. Sci.* **6**, 625-633 (2013).

41 Mattheiss, L. Band structures of transition-metal-dichalcogenide layer compounds. *Phys. Rev. B* **8**, 3719 (1973).

42 Schönfeld, B., Huang, J. & Moss, S. Anisotropic mean-square displacements (MSD) in single-crystals of 2H-and 3R- MoS_2. *Acta Crystallogr. B Struct. Sci.* **39**, 404-407 (1983).

43 Kim, B. S., *et al.* Determination of the band parameters of bulk 2H-MX_2 (M= Mo, W; X= S, Se) by angle-resolved photoemission spectroscopy. *Sci. Rep.* **6**, 36389 (2016).

44 Ganatra, R. & Zhang, Q. Few-layer MoS_2: a promising layered semiconductor. *ACS Nano* **8**, 4074-4099 (2014).

45 Kuc, A., Zibouche, N. & Heine, T. Influence of quantum confinement on the electronic structure of the transition metal sulfide TS_2. *Phys. Rev. B* **83**, 245213 (2011).

46 Eda, G. *et al.* Photoluminescence from chemically exfoliated MoS_2. *Nano Lett.* **11**, 5111-5116 (2011).

47 Jo, M. *et al.* Origin of the blueshift of photoluminescence in a type-II heterostructure. *Nanoscale Res. Lett.* **7**, 654 (2012).

48 Venkata Subbaiah, Y., Saji, K. & Tiwari, A. Atomically thin MoS_2: A versatile nongraphene 2D material. *Adv. Funct. Mater.* **26**, 2046-2069 (2016).

49 Zeng, H. *et al.* Optical signature of symmetry variations and spin-valley coupling in atomically thin tungsten dichalcogenides. *Sci. Rep.* **3**, 1608 (2013).

50 Gutiérrez, H. R. *et al.* Extraordinary room-temperature photoluminescence in triangular WS_2 monolayers. *Nano Lett.* **13**, 3447-3454 (2012).

51 Savjani, N., *et al.* MoS_2 nanosheet production by the direct exfoliation of molybdenite minerals from several type-localities. *Rsc Adv.* **4**, 35609-35613 (2014).

52 Visic, B. *et al.* Optical properties of exfoliated MoS_2 coaxial nanotubes-analogues of graphene. *Nanoscale Res. Lett.* **6**, 593 (2011).

53 Hill, H. M. *et al.* Observation of excitonic Rydberg states in monolayer MoS_2 and WS_2 by photoluminescence excitation spectroscopy. *Nano Lett.* **15**, 2992-2997 (2015).

54 Liu, H.-L. *et al.* Optical properties of monolayer transition metal dichalcogenides probed by spectroscopic ellipsometry. *Appl. Phys. Lett.* **105**, 201905 (2014).

55 Yim, C. *et al.* Investigation of the optical properties of MoS_2 thin films using spectroscopic ellipsometry. *Appl. Phys. Lett.* **104**, 103114 (2014).

56 Weber, J., Calado, V. & Van De Sanden, M. Optical constants of graphene measured by spectroscopic ellipsometry. *Appl. Phys. Lett.* **97**, 091904 (2010).

57 Sheik-Bahae, *et al.* High-sensitivity, single-beam n_2 measurements. *Opt. Lett.* **14**, 955-957 (1989).

58 Sheik-Bahae, M., *et al.* Sensitive measurement of optical nonlinearities using a single beam. *IEEE J. Quantum Electron.* **26**, 760-769 (1990).

59 Kuzyk, M. & Dirk, C. Z-Scan measurements of optical nonlinearities. *Characterization Techniques and Tabulations for Organic Nonlinear Materials*, 655-692 (1998).

60 Wei, R. *et al.* Versatile preparation of ultrathin MoS_2 nanosheets with reverse saturable absorption response. *Opt. Mater. Express* **5**, 1807-1814 (2015).

61 Wang, K. *et al.* Ultrafast saturable absorption of two-dimensional MoS_2 nanosheets. *ACS Nano* **7**, 9260-9267 (2013).

62 Li, H., *et al.* Preparation and applications of mechanically exfoliated single-layer and multilayer MoS_2 and WSe_2 nanosheets. *Acc. Chem. Res.* **47**, 1067-1075 (2014).

63 Lin, M.-W. *et al.* Thickness-dependent charge transport in few-layer MoS_2 field-effect transistors. *Nanotechnology* **27**, 165203 (2016).

64 Kim, S. *et al.* High-mobility and low-power thin-film transistors based on multilayer MoS_2 crystals. *Nat. Commun.* **3**, 1011 (2012).

65 Laskar, M. R. *et al.* Large area single crystal (0001) oriented MoS_2. *Appl. Phys. Lett.* **102**, 252108,(2013).

66 Baek, S. H., Choi, Y. & Choi, W. Large-area growth of uniform single-layer MoS_2 thin films by chemical vapor deposition. *Nanoscale Res. Lett.* **10**, 1 (2015).

67 Shidpour, R., *et al.* A general two-step chemical vapor deposition procedure to synthesize highly crystalline transition metal dichalcogenides: A case study of MoS_2. *Mater. Res. Bull.* **76**, 473-478 (2016).

68 Li, X. & Zhu, H. Two-dimensional MoS_2: Properties, preparation, and applications. *J. Materiomics* **1**, 33-44 (2015).

69 Dhyani, V. & Das, S. High-speed scalable silicon- MoS_2 PN heterojunction photodetectors. *Sci. Rep.* **7**, 44243 (2017).

70 Sun, M. *et al.* Lateral multilayer/monolayer MoS_2 heterojunction for high performance photodetector applications. *Sci. Rep.* **7**, 4505 (2017).

71 Rao, C., Gopalakrishnan, K. & Maitra, U. Comparative study of potential applications of graphene, MoS_2, and other two-dimensional materials in energy devices, sensors, and related areas. *ACS Appl. Mater. Interfaces* **7**, 7809-7832 (2015).

72 Park, M. *et al.* MoS_2-based tactile sensor for electronic skin applications. *Adv. Mater.* **28**, 2556-2562 (2016).

73 Zhang, J. *et al.* Observation of strong interlayer coupling in MoS_2/WS_2 heterostructures. *Adv. Mater.* **28**, 1950-1956 (2016).

74 Cheng, R. *et al.* Electroluminescence and photocurrent generation from atomically sharp WSe_2/ MoS_2 heterojunction p–n diodes. *Nano Lett.* **14**, 5590-5597 (2014).

75 Gong, Y. *et al.* Vertical and in-plane heterostructures from WS_2/MoS_2 monolayers. *Nat. Mater.* **13**, 1135 (2014).

76 Chen, H. *et al.* Ultrafast formation of interlayer hot excitons in atomically thin MoS_2/WS_2 heterostructures. *Nat. Commun.* **7**, 12512 (2016).

77 Chen, K. *et al.* Electronic properties of MoS_2–WS_2 heterostructures synthesized with two-step lateral epitaxial strategy. *Acs Nano* **9**, 9868-9876 (2015).

78 Qiao, W. *et al.* Luminescent monolayer MoS_2 quantum dots produced by multi-exfoliation based on lithium intercalation. *Appl. Surf. Sci.* **359**, 130-136 (2015).

79 Ali, J., *et al.* Fabrication of blue luminescent MoS_2 quantum dots by wet grinding assisted co-solvent sonication. *J. Lumin.* **169**, 342-347 (2016).

80 Li, B. *et al.* Preparation of monolayer MoS_2 quantum dots using temporally shaped femtosecond laser ablation of bulk MoS_2 targets in water. *Sci. Rep.* **7**, 11182 (2017).

81 Oztas, T., *et al.* Synthesis of colloidal 2D/3D MoS_2 nanostructures by pulsed laser ablation in an organic liquid environment. *J. Phys. Chem. C* **118**, 30120-30126 (2014).

82 Novoselov, K. S. *et al.* Two-dimensional atomic crystals. *Proc. Natl. Acad. Sci* **102**, 10451-10453 (2005).

83 Joensen, P., *et al.* Single-layer MoS_2. *Mater. Res. Bull.* **21**, 457-461 (1986).

84 Smith, R. J. *et al.* Large-scale exfoliation of inorganic layered compounds in aqueous surfactant solutions. *Adv. Mater.* **23**, 3944-3948 (2011).

85 Coleman, J. N. *et al.* Two-dimensional nanosheets produced by liquid exfoliation of layered materials. *Science* **331**, 568-571 (2011).

86 Zhou, X., *et al.* Hydrothermal synthesis of flower-like MoS_2 nanospheres for electrochemical supercapacitors. *J. Nanosci. Nanotechnol.* **14**, 7250-7254 (2014).

87 Liao, H., *et al.* A solution low-temperature route to MoS_2 fiber. *Chem. Mater.* **13**, 6-8 (2001).

88 Li, X., *et al.* Solution-processed MoSx as an efficient anode buffer layer in organic solar cells. *ACS Appl. Mater. Interfaces* **5**, 8823-8827 (2013).

89 Li, X. *et al.* Large-area synthesis of high-quality and uniform graphene films on copper foils. *Science* **324**, 1312-1314 (2009).

90 Liu, K.-K. *et al.* Growth of large-area and highly crystalline MoS_2 thin layers on insulating substrates. *Nano Lett.* **12**, 1538-1544 (2012).

91 Zhan, Y., Liu, Z., Najmaei, S., Ajayan, P. M. & Lou, J. Large-area vapor-phase growth and characterization of MoS_2 atomic layers on a SiO_2 substrate. *Small* **8**, 966-971 (2012).

92 Lee, Y. H. *et al.* Synthesis of large-area MoS_2 atomic layers with chemical vapor deposition. *Adv. Mater.* **24**, 2320-2325 (2012).

93 Ratha, S. & Rout, C. S. Supercapacitor electrodes based on layered tungsten disulfide-reduced graphene oxide hybrids synthesized by a facile hydrothermal method. *ACS appl. mater. interfaces* **5**, 11427-11433 (2013).

94 Godin, K., *et al.* Increased monolayer domain size and patterned growth of tungsten disulfide through controlling surface energy of substrates. *J. Phys. D* **49**, 325304 (2016).

95 Siegel, G., *et al.* Growth of centimeter-scale atomically thin MoS_2 films by pulsed laser deposition. *APL Mater.* **3**, 056103 (2015).

96 Loh, T. A. & Chua, D. H. Growth mechanism of pulsed laser fabricated few-layer MoS_2 on metal substrates. *ACS Appl. Mater. interfaces* **6**, 15966-15971 (2014).

97 Serrao, C. R. *et al.* Highly crystalline MoS_2 thin films grown by pulsed laser deposition. *Appl. Phys. Lett.* **106**, 052101 (2015).

98 Late, D. J. *et al.* Pulsed laser-deposited MoS_2 thin films on W and Si: field emission and photoresponse studies. *ACS Appl. Mater. Interfaces* **6**, 15881-15888 (2014).

99 Loh, T. A., Chua, D. H. & Wee, A. T. One-step synthesis of few-layer WS_2 by pulsed laser deposition. *Sci. Rep.* **5**, 18116 (2015).

100 Loh, T. A. & Chua, D. H. Origin of hybrid 1T-and 2H-WS_2 ultrathin layers by pulsed laser deposition. *J. Phys. Chem. C* **119**, 27496-27504 (2015).

101 Yao, J., *et al.* highly-responsive and broadband photodetection based on large-area multilayered WS_2 films grown by pulsed-laser deposition. *Nanoscale* **7**, 14974-14981 (2015).

102 Yang, Z. & Hao, J. Progress in pulsed laser deposited two-dimensional layered materials for device applications. *J. Mater. Chem. C* **4**, 8859-8878 (2016).

103 Schenato, M. *et al.* Effect of annealing and nanostructuring on pulsed laser deposited WS_2 for HER catalysis. *Appl. Catal. A Gen.* **510**, 156-160 (2016).

104 Smith, H. M. & Turner, A. Vacuum deposited thin films using a ruby laser. *Appl. Opt.* **4**, 147-148 (1965).

105 Dijkkamp, D. *et al.* Preparation of Y-Ba-Cu oxide superconductor thin films using pulsed laser evaporation from high T c bulk material. *Appl. Phys. Lett.* **51**, 619-621 (1987).

106 Fogarassy, E., Fuchs, C., Slaoui, A. & Stoquert, J. SiO_2 thin-film deposition by excimer laser ablation from SiO target in oxygen atmosphere. *Appl. Phys. Lett.* **57**, 664-666 (1990).

107 Balooch, M. *et al.* Deposition of SiC films by pulsed excimer laser ablation. *Appl. Phys. Lett.* **57**, 1540-1542 (1990).

108 Biunno, N., *et al.* Low-temperature processing of titanium nitride films by laser physical vapor deposition. *Appl. Phys. Lett.* **54**, 1519-1521 (1989).

109 Hansen, S. & Robitaille, T. Formation of polymer films by pulsed laser evaporation. *Appl. Phys. Lett.* **52**, 81-83 (1988).

110 Krebs, H. U. & Bremert, O. Pulsed laser deposition of thin metallic alloys. *Appl. Phys. Lett.* **62**, 2341-2343 (1993).

111 Walck, S., *et al.* Evolution of surface topography in pulsed-laser-deposited thin films of MoS_2. *Surf. Coat Technol.* **62**, 412-416 (1993).

112 Bruncko, J. *et al.* Comparative study of ZnO thin film prepared by pulsed laser deposition–Comparison of influence of different ablative lasers. *Vacuum* **138**, 184-190 (2017).

113 Fominski, V. *et al.* Chemical composition, structure and light reflectance of W–Se and W–Se–C films prepared by pulsed laser deposition in rare and reactive buffer gases. *Vacuum* **119**, 19-29 (2015).

114 Zhu, B. *et al.* The effects of substrate temperature on the structure and properties of ZnO films prepared by pulsed laser deposition. *Vacuum* **82**, 495-500 (2008).

115 Acerce, M., Voiry, D. & Chhowalla, M. Metallic 1T phase MoS_2 nanosheets as supercapacitor electrode materials. *Nat. Nanotechnol.* **10**, 313 (2015).

116 Sarode, K. & Patil, D. Metallic 1T Phase MoS_2 Nanosheets for Supercapacitor Application. *J. Nanosci. Technol.*, **4**, 371-373 (2018).

117 Dey, P. P. & Khare, A. Stoichiometry-dependent linear and nonlinear optical properties of PLD SiOx thin films. *J. Alloys Compd.* **706**, 370-376 (2017).

118 Kumar, I. & Khare, A. Optical nonlinearity in nanostructured carbon thin films fabricated by pulsed laser deposition technique. *Thin Solid Films* **611**, 56-61 (2016).

119 Fujiwara, H. *Spectroscopic ellipsometry: principles and applications*. (John Wiley & Sons, 2007).

120 Lee, C. *et al.* Anomalous lattice vibrations of single-and few-layer MoS_2. *ACS Nano* **4**, 2695-2700 (2010).

121 Yang, M. *et al.* Study of the Raman peak shift and the linewidth of light-emitting porous silicon. *J. Appl.Phys.* **75**, 651-653 (1994).

122 Yang, L. *et al.* Lattice strain effects on the optical properties of MoS_2 nanosheets. *Sci. Rep.* **4**, 5649 (2014).

123 Wu, C.-R., *et al.* The Growth Mechanism of Transition Metal Dichalcogenides by using Sulfurization of Pre-deposited Transition Metals and the 2D Crystal Hetero-structure Establishment. *Sci. Rep.* **7** (2017).

124 Reichelt, K. Nucleation and growth of thin films. *Vacuum* **38**, 1083-1099 (1988).

125 Chopra, K. Growth of sputtered vs evaporated metal films. *J Appl. Phys.* **37**, 3405-3410 (1966).

126 Yu, Y. *et al.* Controlled scalable synthesis of uniform, high-quality monolayer and few-layer MoS_2 films. *Sci. Rep.* **3** (2013).

127 Kim, J. G., *et al.* Effect of interlayer interactions on exciton luminescence in atomic-layered MoS_2 crystals. *Sci. Rep.* **6**, 29813 (2016).

128 Hao, Q. *et al.* Boosting the Photoluminescence of Monolayer MoS2 on High-Density Nanodimer Arrays with Sub-10 nm Gap. *Adv. Optic. Mater.* **6**, 1700984, (2018).

129 Nayak, A. P. *et al.* Pressure-dependent optical and vibrational properties of monolayer molybdenum disulfide. *Nano Lett.* **15**, 346-353 (2014).

130 Wexler, S. Deposition of atomic beams. *Rev. Mod. Phys* **30**, 402 (1958).

131 Venables, J., *et al.* Nucleation and growth of thin films. *Rep. Prog. Phys.* **47**, 399 (1984).

132 Chopra, K. L. Thin film phenomena. (1969).

133 Wypych, F. & Schöllhorn, R. 1T- MoS_2, a new metallic modification of molybdenum disulfide. *J. Chem. Soc., Chem. Commun.* 1386-1388 (1992).

134 Reshmi, S., *et al.* Structural stability of coplanar 1T-2H superlattice MoS_2 under high energy electron beam. *Nanotechnology* **29**, 205604 (2018).

135 Li, D. *et al.* Optical properties of thickness-controlled MoS_2 thin films studied by spectroscopic ellipsometry. *Appl. Surf. Sci.* **421**, 884-890 (2017).

136 Pankove, J. I. *Optical processes in semiconductors*. (Courier Corporation, 1975).

137 Leong, S. X. *et al.* 2H→ 1T Phase Change in Direct Synthesis of WS2 Nanosheets via Solution-Based Electrochemical Exfoliation and Their Catalytic Properties. *ACS Appl. Mater. Interfaces* **9**, 26350-26356 (2017).

138 Lin, Y.-C., *et al.* Atomic mechanism of the semiconducting-to-metallic phase transition in single-layered MoS_2. *Nat. Nanotechnol.* **9**, 391 (2014).

139 Kang, Y. *et al.* Plasmonic hot electron induced structural phase transition in a MoS_2 monolayer. *Adv. Mater.* **26**, 6467-6471 (2014).

140 Sarma, S. & Ray, S. C. Trigonal (1T) and hexagonal (2H) mixed phases MoS_2 thin films. *Appl. Surf. Sci.* **474**, 227-231, (2019).

141 Cheng, P., *et al.* Mechanically-induced reverse phase transformation of MoS 2 from stable 2H to metastable 1T and its memristive behavior. *Rsc Adv.* **6**, 65691-65697 (2016).

142 Zhu, J. *et al.* Argon plasma induced phase transition in monolayer MoS_2. *J. Am. Chem. Soc.* **139**, 10216-10219 (2017).

143 Tongay, S. *et al.* Defects activated photoluminescence in two-dimensional semiconductors: interplay between bound, charged, and free excitons. *Sci. Rep.* **3**, 2657 (2013).

144 Tsai, C. *et al.* Electrochemical generation of sulfur vacancies in the basal plane of MoS_2 for hydrogen evolution. *Nat. Commun.* **8**, 15113 (2017).

145 Loh, T. A., Chua, D. H. & Wee, A. T. One-step synthesis of few-layer WS_2 by pulsed laser deposition. *Sci. Rep.* **5** (2015).

146 Nabiyouni, G. & Farahani, B. J. Anomalous scaling in surface roughness evaluation of electrodeposited nanocrystalline Pt thin films. *Appl. Surf. Sci.* **256**, 674-682 (2009).

147 Al-Kuhaili, M. Characterization of thin films produced by the thermal evaporation of silver oxide. *J. Phys. D* **40**, 2847 (2007).

148 Ramasco, J. J., *et al.* Generic Dynamic Scaling in Kinetic Roughening. *Phys. Rev. Lett.* **84**, 2199-2202 (2000).

149 Pelliccione, M. & Lu, T. M. *Evolution of Thin Film Morphology: Modeling and Simulations*. 1 edn, Vol. **108** (Springer-Verlag New York, 2008).

150 Nasehnejad, M., *et al.* Dynamic scaling study of nanostructured silver films. *J. Phys. D* **50**, 375301, (2017).

151 Gupta, I. & Mohanty, B. C. Dynamics of surface evolution in semiconductor thin films grown from a chemical bath. *Sci. Rep.* **6**, 33136 (2016).

152 Saitou, M. Anomalous scaling of nickel surfaces in pulse-current electrodeposition growth. *Phys. Rev. B* **66**, 073416 (2002).

153 Das Sarma, S., *et al.* Scale invariance and dynamical correlations in growth models of molecular beam epitaxy. *Phys. Rev. E* **53**, 359-388 (1996).

154 López, J. M., *et al.* Superroughening versus intrinsic anomalous scaling of surfaces. *Phys. Rev. E* **56**, 3993-3998 (1997).

155 López, J. M. Scaling Approach to Calculate Critical Exponents in Anomalous Surface Roughening. *Phys. Rev. Lett.* **83**, 4594-4597 (1999).

156 Obaidulla, S. M. & Giri, P. Surface roughening and scaling behavior of vacuum-deposited $SnCl_2Pc$ organic thin films on different substrates. *Appl. Phys. Lett.* **107**, 221910 (2015).

157 Torres, M. F. & Buceta, R. C. Intrinsic anomalous scaling in a ferromagnetic thin film model. *Eur. Phys. J. B* **86**, 20 (2013).

158 Mullins, W. W. Theory of thermal grooving. *J. Appl. Phys.* **28**, 333-339 (1957).

159 Edwards, S. F. & Wilkinson, D. in *Proc. R. Soc. A.* 17-31 (The Royal Society).

160 Kardar, M., *et al.* Dynamic scaling of growing interfaces. *Phys. Rev. Lett.* **56**, 889 (1986).

161 Yao, J. H. *et al.* Shadowing instability in three dimensions. *Phys. Rev. E* **47**, 1007 (1993).

162 Karunasiri, R., *et al.* Thin-film growth and the shadow instability. *Phys. Rev. Lett.* **62**, 788 (1989).

163 Drotar, J. T., *et al.* Surface roughening in shadowing growth and etching in 2+1 dimensions. *Phys. Rev. B* **62**, 2118 (2000).

164 Weaver, I. & Lewis, C. Polar distribution of ablated atomic material during the pulsed laser deposition of Cu in vacuum: Dependence on focused laser spot size and power density. *J. Appl. Phys.* **79**, 7216-7222 (1996).

165 Fujiwara, H., *et al.* Real-time spectroscopic ellipsometry studies of the nucleation and grain growth processes in microcrystalline silicon thin films. *Phys. Rev. B* **63**, 115306 (2001).

166 Fujiwara, H., *et al.* Assessment of effective-medium theories in the analysis of nucleation and microscopic surface roughness evolution for semiconductor thin films. *Phys. Rev. B* **61**, 10832 (2000).

167 Losurdo, M. & Hingerl, K. *Ellipsometry at the Nanoscale*. (Springer, 2013).

168 Palasantzas, G. Static and dynamic aspects of the rms local slope of growing random surfaces. *Phys. Rev. E* **56**, 1254 (1997).

169 Logothetidis, S. Surface-roughness and grain-boundary effects on the optical properties of low-pressure chemical-vapor-deposited silicon thin films by spectroscopic ellipsometry. *J. Appl. Phys.* **65**, 2416-2426 (1989).

170 McMarr, P., *et al.* Thickness-dependent void fraction of rf-sputtered amorphous Ge films by spectroscopic ellipsometry. *Appl. Phys. Lett.* **49**, 328-330 (1986).

171 Sundari, S. T., Dash, S. & Tyagi, A. in *Nanoscience, Engineering and Technology (ICONSET), 2011 International Conference on.* 543-547 (IEEE).

172 Pelliccione, M. & Lu, T.-M. *Evolution of thin film morphology*. Vol. **108** (Springer, 2008).

173 Ruffino, F. & Grimaldi, M. Atomic force microscopy study of the growth mechanisms of nanostructured sputtered Au film on Si (111): evolution with film thickness and annealing time. *J. Appl. Phys.* **107**, 104321 (2010).

174 Raible, M. *et al.* Amorphous thin-film growth: Theory compared with experiment. *EPL (Europhysics Letters)* **50**, 61 (2000).

175 Edwards, S. F. & Wilkinson, D. The surface statistics of a granular aggregate. *in Proc. R. Soc. A.* **381**, 17-31 (1982).

176 Tripathi, N., *et al.* Growth dynamics of pulsed laser deposited indium oxide thin films: a substrate dependent study. *Appl. Surf. Sci.* **256**, 7091-7095 (2010).

177 Dolbec, R. *et al.* Growth dynamics of pulsed laser deposited Pt nanoparticles on highly oriented pyrolitic graphite substrates. *Phys. Rev. B* **70**, 201406 (2004).

178 Auger, M. A. *et al.* Growth dynamics of reactive-sputtering-deposited AlN films. *J. Appl. Phys.* **97**, 123528 (2005).

179 Friberg, S. & Smith, P. Nonlinear optical glasses for ultrafast optical switches. *IEEE J. Quantum Electron.* **23**, 2089-2094 (1987).

180 Weber, M., *et al.* Nonlinear refractive index of glasses and crystals. *Opt. Eng.* **17**, 175463 (1978).

181 Owyoung, A. Ellipse rotation studies in laser host materials. *IEEE J. Quantum Electron* **9**, 1064-1069 (1973).

182 Debelo, N., Dejene, F., Roro, K., Pricilla, M. & Oliphant, C. The effect of argon gas pressure on structural, morphological and photoluminescence properties of pulsed laser deposited KY3F10:Ho3+ thin films. *Appl. Phys. A* **122**, 619 (2016).

183 Bayesteh, S., Mortazavi, S. Z. & Reyhani, A. Investigation on nonlinear optical properties of MoS2 nanoflakes grown on silicon and quartz substrates. *J. Phys. D* **51**, 195302 (2018).

184 Bharti, G. P. & Khare, A. Structural and linear and nonlinear optical properties of Zn 1-x Al x O ($0 \leq x \leq 0.10$) thin films fabricated via pulsed laser deposition technique. *Opt. Mater. Express* **6**, 2063-2080 (2016).

185 Dey, P. P. & Khare, A. Effect of substrate temperature on structural and linear and nonlinear optical properties of nanostructured PLD a-SiC thin films. *Mater. Res. Bull.* **84**, 105-117 (2016).

186 Aithal, S., Aithal, P. & Bhat, G. Characteristics of Ideal Optical Limiter and Realization Scenarios Using Nonlinear Organic Materials–A Review. *International Journal of Advanced Trends in Engineering and Technology* **1**, 73-84 (2016).

187 Hollins, R. C. Materials for optical limiters. *Curr. opin. solid st. m.* 4, 189-196 (1999).

188 Dey, P. P. & Khare, A. Nonlinear optical and optical limiting response of PLD nc-Si thin films. *J. Mater. Chem. C* **5**, 12211-12220 (2017).

189 Desarkar, H., *et al.*Effect of ablation time and laser fluence on the optical properties of copper nano colloids prepared by laser ablation technique. *Appl. Nanosci.* **2**, 285-291 (2012).

190 Bajaj, G. & Soni, R. Effect of liquid medium on size and shape of nanoparticles prepared by pulsed laser ablation of tin. *Appl. Phys. A* **97**, 481-487 (2009).

191 Yang, S., *et al.* Size and structure control of Si nanoparticles by laser ablation in different liquid media and further centrifugation classification. *J. Phys. Chem. C* **113**, 19091-19095 (2009).

192 Pradhan, G. & Sharma, A. K. Anomalous Raman and photoluminescence blue shift in mono-and a few layered pulsed laser deposited MoS_2 thin films. *Mater. Res. Bull.* **102**, 406-411 (2018).

193 Pradhan, G. & Sharma, A. K. Temperature controlled 1T/2H phase ratio modulation in mono-and a few layered MoS_2 films. *Appl. Surf. Sci.* **479**, 1236–1245 (2019).

194 Korn, T., *et al.* Low-temperature photocarrier dynamics in monolayer MoS_2. *Appl. Phys. Lett.* **99**, 102109 (2011).

195 Xu, L. *et al.* Analysis of photoluminescence behavior of high-quality single-layer MoS_2. *Nano Res.* **12**, 1619-1624 (2019).

196 Makhlouf, A. S. H. & Barhoum, A. *Emerging Applications of Nanoparticles and Architectural Nanostructures: Current Prospects and Future Trends*. (William Andrew, 2018).

197 Gupta, A., Arunachalam, V. & Vasudevan, S. Water dispersible, positively and negatively charged MoS_2 nanosheets: surface chemistry and the role of surfactant binding. *J. Phys. Chem. Lett.* **6**, 739-744 (2015).

198 Anbazhagan, R., *et al.* Highly concentrated MoS_2 nanosheets in water achieved by thioglycolic acid as stabilizer and used as biomarkers. *RSC Adv.* **4**, 42936-42941 (2014).

199 Liu, W., *et al.* Ultra-stable two-dimensional MoS_2 solution for highly efficient organic solar cells. *RSC Adv.* **4**, 32744-32748 (2014).

200 Pan, D., *et al.* Hydrothermal route for cutting graphene sheets into blue-luminescent graphene quantum dots. *Adv. Mater.* **22**, 734-738 (2010).

201 Bao, L. *et al.* Electrochemical tuning of luminescent carbon nanodots: from preparation to luminescence mechanism. *Adv. Mater.* **23**, 5801-5806 (2011).

202 Gan, Z. *et al.* Mn2+-bonded reduced graphene oxide with strong radiative recombination in broad visible range caused by resonant energy transfer. *Nano Lett.* **11**, 3951-3956 (2011).

203 Wackerow, S. & Abdolvand, A. Generation of silver nanoparticles with controlled size and spatial distribution by pulsed laser irradiation of silver ion-doped glass. *Opt. Express* **22**, 5076-5085 (2014).

204 Gu, W., *et al.* One-step synthesis of water-soluble MoS2 quantum dots via a hydrothermal method as a fluorescent probe for hyaluronidase detection. *ACS Appl. Mater. Interfaces* **8,** 11272-11279 (2016).

205 Qiao, W. *et al.* Monolayer MoS 2 quantum dots as catalysts for efficient hydrogen evolution. *RSC Adv.* **5**, 97696-97701 (2015).

206 Tee, S. Y. *et al.* Recent progress in energy-driven water splitting. *Adv. Sci.* **4**, 1600337 (2017).

207 Zou, X. & Zhang, Y. Noble metal-free hydrogen evolution catalysts for water splitting. *Chem. Soc. Rev.* **44**, 5148-5180 (2015).

208 Li, X., *et al.* Nanostructured catalysts for electrochemical water splitting: current state and prospects. *J. Mater. Chem. A* **4**, 11973-12000 (2016).

209 Grigoriev, S., *et al.* Pulsed laser deposition of nanocomposite MoSex/Mo thin-film catalysts for hydrogen evolution reaction. *Thin Solid Films* **592**, 175-181 (2015).

210 Bonde, J., Moses, P. G., Jaramillo, T. F., Nørskov, J. K. & Chorkendorff, I. Hydrogen evolution on nano-particulate transition metal sulfides. *Faraday Discussions* **140**, 219-231 (2009).

211 Shi, J. *et al.* Controllable growth and transfer of monolayer MoS_2 on Au foils and its potential application in hydrogen evolution reaction. *ACS Nano* **8**, 10196-10204 (2014).

212 Li, H. *et al.* Activating and optimizing MoS_2 basal planes for hydrogen evolution through the formation of strained sulphur vacancies. *Nat. Mater.* **15**, 48 (2016).

213 Gnanasekar, P., *et al.* Vertically aligned MoS_2 nanosheets on graphene for highly stable electrocatalytic hydrogen evolution reactions. *Nanoscale* **11**, 2439-2446 (2019).

214 Tao, L., Duan, *et al.* Plasma-engineered MoS_2 thin-film as an efficient electrocatalyst for hydrogen evolution reaction. *Chem. Commun.* **51**, 7470-7473 (2015).

Journal publications:

1. **G. Pradhan**, A.K Sharma, *Anomalous Raman and photoluminescence blue shift of a few layered pulsed laser deposited MoS_2 films*, Mat. Res. Bull., 102 (2018) 406–411.
2. **G. Pradhan**, A.K. Sharma, *Linear and non-linear optical response of sulfur deficient nanocrystallite WS_2 thin films*, J. Mat. Sci., 54 (2019), 14809-14824.
3. **G. Pradhan**, P.P. Dey, A.K. Sharma, *Anomalous kinetic roughening in growth of MoS_2 films under pulsed laser deposition*, RSC Adv., 9 (2019) 12895–12905.
4. **G. Pradhan**, A.K. Sharma, *Temperature-controlled 1T/2H phase ratio modulation in mono- and a few layered MoS_2 films*, Appl. Surf. Sci., 479 (2019) 1236–1245.
5. **G. Pradhan**, P.P. Dey, A.K. Sharma, *Surface evolution and scaling properties of pulsed laser deposited WS_2 thin films on different substrates*, Appl. Phys. A 475 (2020) 1-7.

Under preparation:

1. **G. Pradhan,** P.P. Dey, Alika Khare and A.K. Sharma, *Synthesis and size modulation of MoS_2 quantum dots by pulsed laser ablation in liquid for viable hydrogen generation*.

Conference Proceeding:

1. G. Pradhan, R. Kesarwani, A. Khare and A. K. Sharma, *Thickness dependent optical properties of MoS_2 thin films probed by spectroscopic ellipsometry*. Optical Society of America, P1A.14 (2016).

Book Article:

G. Pradhan, P. P. Dey and A. K. Sharma, '*MoS_2 Quantum Dots Synthesis and Their Size Modulation by Pulsed Laser Ablation in Liquid'* in "Advances in Science and Technology", Volume II, 2020, McGraw-Hill (accepted).

Conference attended:

1. Rahul Kesarwani, **Gobinda Pradhan**, Sasmita Behera, Ashwini K Sharma and Alika Khare, "*Surface morphology and optical properties study of thin films grown by PLD*." Research conclave (2016), IIT Guwahati, India. (Poster presentation)

2. **Gobinda Pradhan** and Ashwini K Sharma, "*Optical properties of bilayer MoS_2 film deposited by PLD technique*." ICLLT-2016, Tezpur University, India. (Poster presentation)

3. **Gobinda Pradhan**, Rahul Kesarwani, Alika Khare and Ashwini K Sharma, "*Thickness dependent optical properties of MoS_2 thin films probed by spectroscopic ellipsometry*." Photonics -2016, IIT Kanpur, India. (Poster presentation)

4. **Gobinda Pradhan** and Ashwini K Sharma, "*2D Layered MoS_2 Films Growth Using PLD Technique*", ICNANO-2017, Allahabad, India. (Poster presentation)

5. **Gobinda Pradhan** and Ashwini K Sharma, "*Temperature controlled nucleation and growth of a few layered MoS_2 films*", ICTF-2017, Delhi, India. (Poster presentation)

6. **Gobinda Pradhan,** Parth P Dey and Ashwini K Sharma, "*MoS_2 quantum dots synthesis and their size modulation by pulsed laser ablation in liquid*", NCRAST-2019, Guwahati, India. (Poster presentation)

7. **Gobinda Pradhan** and Ashwini K Sharma, "*Shape and Size Modulation of MoS_2 Quantum Dots Synthesis by Pulsed Laser Ablation in Distilled Wate*r", ICMAT-2019, Singapore. (Oral presentation)

Workshops attended:

1. "National workshop on Advanced Probing Techniques in TEM", APTTEM-2016, IIT Guwahati, Guwahati, India.

2. "One-Day Workshop on Vacuum Technology and its Applications in Optical Science", IIT Guwahati, Guwahati, India on August 19th, 2017.

Awards:

1. First prize in poster presentation titled "*MoS_2 quantum dots synthesis and their size modulation by pulsed laser ablation in liquid*" in NCRAST-2019, 15-17 May 2019, Guwahati, India.

2. DST, SERB international travel support (ITS) for attending the international conference named 'ICMAT-2019',23-28 June 2019, Marina Bay Sands, Singapore.